# Carrier Recombination in Multicrystalline Silicon: A Study using Photoluminescence Imaging

Hang Cheong Sio

November 2015

A thesis submitted for the degree of

Doctor of Philosophy

of The Australian National University


Australian National University

# Declaration

I certify that this thesis does not incorporate without acknowledgement any material previously submitted for a degree or diploma in any university, and that, to the best of my knowledge, it does not contain any material previously published or written by another person except where due reference is made in the text. The work in this thesis is my own, except for the contributions made by others as described in the Acknowledgements.

Hang Cheong Sio

November 2015

# Acknowledgements

This work would not have been possible without the help of a number of people.

First and foremost, I would like to express my deepest gratitude to my primary supervisor, Associate Professor Daniel Macdonald, for his continuous support and encouragement throughout my entire Ph.D. study. He has always made himself available for discussion, provided me a lot of sound advice and insights, and allowed me great freedom in my research. Thank you especially for being extremely patient with me when I first started, which reduced my stress and anxiety as a student who barely knew anything about multicrystalline silicon beforehand. I would also like to thank Professor Andres Cuevas, for sharing his passion and knowledge in modelling of silicon device, which inspires much of the work in this thesis. I am grateful to Associate Professor Thorsten Trupke of UNSW for his invaluable suggestion and feedback, particularly in the area of photoluminescence imaging. Thank Professor Hoe Tan for being on my supervisory panel. I would also like to acknowledge scholarship support from BT Imaging and the Australian Renewable Energy Agency (ARENA).

I am indebted to Dr. Sieu Pheng Phang, who helped me a lot in my Ph.D. study, from experiment planning, sample processing, to thesis writing. Pheng shared his carrier de-smearing tool which is used throughout this thesis. Thank you also for devoting your time and effort to listen and response to my ideas, even though most of them are neither sensible nor practical. I am extremely thankful to Di Yan, who helped me to perform the Sentaurus simulation presented in Chapter 5 on short notice and provided numerous assistances in sample processing. I am appreciative of Hieu Nguyen for performing the micron scale photoluminescence spectroscopy measurement used in Chapter 5. Thank Teck Kong Chong for his innovative idea to create silicon strips for studying orientation dependent passivation effect presented in Chapter 7 and Sachin Surve for implementing the laser cutting.

I am also grateful to other colleagues at ANU. Dr. Fiacre Rougieux helped implementing the carrier mobility models to the models used in Chapters 3 and 4. Dr. Daniel Walter provided the PSF for correcting the optical smearing in the silicon CCD

camera. Dr. Frank Brink and Dr. Hua Chen assisted me with the EBSD measurements. Thank Dr. Wensheng Liang for teaching me how to operate the ALD system, Erin Crisp for the dicing saw training, Dr. Yimao Wan for sharing his knowledge on surface passivation, Simeon Baker-Finch for sharing his expertise on optical modelling, Anyao Liu and Ryan Sun for the fruitful discussion on hydrogenation and metal defects. I would also like to send my thanks to Chris Samundsett, James Bullock, Teng Kho and Dr. Eric Wang for assistance with sample preparation. I also acknowledge the effort from Bruce Condon, Nina de Caritat, Maureen Brauers, James Cotsell, Mark Saunders, Wie Joe and Dr. Beatriz Velasco in keeping the lab running smoothly and safely.

It has been my pleasure to work in such a friendly and enjoyable environment. Thanks given to those people who came to our office for a nice chat or maybe for biscuits, and more thanks to those few who actually supplied the biscuits. I must mention my wonderful lunch buddies: Pheng, Teng, Teck, Eric, Siew, Tom R., Chog, Peiting, An, Di, James B., Tom A., and Kean. You guys have made my lunch fascinating. I am also grateful to have the chance to meet so many wonderful people: Azul, Brendan, Da, Heping, Ingrid, Jin Jin, Josephine, Judy, Lachlan, Louis, Maxime, Mohsen, Nick, Peter, Soe Zin, Xiao, Xinyu, Yiliang.

I would like to express my deepest appreciation to my parents and my sisters for their unconditional love. Thank my parents for providing me the opportunity to study abroad. Thank you for giving me great freedom to explore the world, and welcoming me home when I am tired. Last, but certainly not least, I would like to thank my girlfriend Katrina for her encouragement and support, and for bearing my bad temper over the last few months.

# Abstract

Multicrystalline silicon is the most commonly used material for solar cell applications [1]. While being lower in cost, multicrystalline silicon wafers inherently contain crystal defects such as grain boundaries and dislocations, and also have relatively high metal impurity concentrations, which can act as strong recombination centres for excess carriers, resulting in less efficient cells compared to monocrystalline silicon solar cells. Understanding the recombination properties of multicrystalline silicon is therefore important for improving the efficiency of multicrystalline silicon solar cells. This thesis applies photoluminescence imaging technique [2] to study various carrier recombination mechanisms in multicrystalline silicon materials.

Photoluminescence calibrated carrier lifetime imaging has been used throughout this thesis to assess the lifetimes of inhomogeneous multicrystalline silicon wafers. A new method for converting steady state photoluminescence images into carrier lifetime images for silicon wafers with inhomogeneous lifetime distribution is presented. The method is based on a calibration factor extracted from a separate, homogeneous, monocrystalline silicon wafer and simple optical modelling of the photoluminescence signal from both the calibration wafer and the test wafer. When applied on multicrystalline silicon wafers, it is found that the lifetimes calibrated by the proposed method are more consistent, in contrast to the lifetimes calibrated by the conventional quasi-steady-state photoconductance based calibration method, in which the magnitude and injection dependence of the lifetimes is observed to be sensitive to the choice of reference area and affected by measurement artefacts, such as minority carrier trapping effects [3, 4], in the quasi-steady-state photoconductance measurements.

Carrier recombination at grain boundaries is a major efficiency loss mechanism in multicrystalline silicon solar cells. Accurate measurement of the recombination properties of grain boundaries is essential for developing methods to reduce their impact on the final cell performance. An approach for quantifying the recombination activities of a grain boundary in terms of its surface recombination velocity, based on the photoluminescence intensity profile across the grain boundary, is developed. This quantity provides a more meaningful and absolute measure of the recombination

properties of a grain boundary compared to commonly used signal contrast methods [5], which can strongly depend on other sample parameters, such as the intra-grain bulk lifetime. The method also allows the injection dependence of the surface recombination velocity of a given grain boundary to be explicitly determined. The proposed approach is demonstrated on both double-side passivated wafers, both before and after phosphorus gettering, and single-side passivated wafers with a strongly non-uniform carrier density profile depth-wise. It is found that the latter allows more recombination active grain boundaries to be analysed, extending the sensitivity of the method.

The approach is then applied to evaluate the recombination properties of a large number of grain boundaries from different parts of a p-type boron doped directionally solidified multicrystalline silicon ingot. The results show that varying impurity levels along the ingot significantly impact the electrical properties of as-grown grain boundaries, and also their response to phosphorus gettering and hydrogenation. Grain boundaries from the middle of the studied ingot become more recombination active after either gettering or hydrogenation alone, whereas grain boundaries from the top and bottom of the ingot have a more varied response. Hydrogenation, in general, is much more effective on gettered grain boundaries compared to as-grown grain boundaries. A close inspection of their injection dependence reveals that while some grain boundaries exhibit little injection dependence before gettering, others show a relatively large injection dependence, with their surface recombination velocities increasing as the injection level decreases. Grain boundaries of the former type tend not to be recombination active after both gettering and hydrogenation, and are less likely to impact the final cell performance in comparison with grain boundaries of the latter type. Moreover, distinct sub-bandgap photoluminescence spectra were detected from grain boundaries that are already active before gettering, and those activated by gettering, suggesting different origins for their recombination activities. Lastly, the detrimental influence of grain boundaries on solar cell devices is discussed with the aid of numerical simulations.

Recent development of the crystal growth technology has led to the production of various types of multicrystalline silicon materials with great potential for high efficiency low cost solar cells. Two notable examples of such are the n-type phosphorus doped multicrystalline silicon and the seed-assisted growth high performance

multicrystalline silicon. Using techniques developed earlier in this work, a thorough comparison of the electrical properties of conventionally solidified p-type, n-type and high performance p-type multicrystalline silicon materials is performed. All studied samples reveal reasonably high diffusion lengths ($> 800\ \mu m$) among the intra-grain regions after gettering and hydrogenation, suggesting that the main performance limiting factors are likely to be recombination at crystal defects. In addition to the reduced amount of dislocations, grain boundaries in the high performance p-type samples show lower recombination behaviour than those in the conventional p-type samples. The electrical properties of multicrystalline silicon materials change substantially after gettering and hydrogenation. While gettering significantly improves the lifetimes of the intra-grain regions, it also increases the recombination rate of the majority of the crystal defects. The effectiveness of hydrogen passivation varies considerably among different materials, being more effective on the n-type samples than the p-type samples.

The last section of this thesis demonstrates the use of the photoluminescence imaging technique to study surface recombination in silicon wafers. The technique offers an opportunity to monitor crystal orientations in multicrystalline silicon wafers through photoluminescence imaging, utilising the observed correlation between surface recombination and crystal orientation in thin, chemically polished and unpassivated wafers. The technique is also applied on passivated samples, for characterising the influence of crystal orientation on dielectric passivation. Application on thermally grown silicon oxide passivated samples reveals that the studied silicon oxide films provide a better passivation on surfaces with higher surface energy, such as (100) or (106) surfaces, compared to those with lower surface energy, such as (235) or (111) surfaces. The methodology proposed can potentially be applied to other dielectric films to evaluate the orientation dependence of their passivation properties. The results of such studies may allow a better understanding of the impact of various crystal planes to recombination at textured surface.

# Table of Contents

# Chapter 1

# Introduction

## 1.1 Motivation

Multicrystalline silicon (Mc-Si) is the most commonly used material in solar cell production, currently accounting for more than 50% of the global market [1]. Mc-Si has proven to be an economical solution for solar cells, giving an effective compromise between high cell efficiency and low material cost. Mc-Si ingots are typically grown by directional solidification in which molten silicon is solidified or cast in a crucible. This process is considerably cheaper than the commonly used Czochralski process for producing single-crystal silicon ingots where the silicon ingot is pulled from molten silicon using a seed crystal. As a result of the ingot growth process, mc-Si material inherently contains crystal defects such as grain boundaries (GBs) and dislocations, and also relatively high metal impurity concentrations, originating from the less pure crucibles and coatings, resulting in less efficient cells in comparison to solar cells produced from single-crystal silicon materials.

The balance between efficiency and material cost appears to have shifted slightly in favour of mc-Si over the past decade, as reflected from the market dominance of mc-Si material in the total crystalline silicon production [1, 6]. This is particularly the case for conventional solar cell architectures such as the screen-printed metallised full-area rear alloyed cells. However, owing to the dramatic price reduction in the silicon feedstock over the last few years, further significant reductions in module price are more likely to be achieved by increasing the cell efficiency, through employing different device structures such as the passivated emitter and rear locally diffused (PERL) [7] or Interdigitated-Back-Contact (IBC) structures [8]. Such high efficiency solar cell architectures have a higher requirement for material quality, and hence may not be as successfully applied to typical mc-Si wafers. Understanding and improving the electrical properties of mc-Si material is, therefore, very important for the material to continue to play a major part in the photovoltaic industry into the future.

Since the final cell performance strongly depends on the material quality, there are continuing efforts to develop new ingot growth methods for higher quality mc-Si materials. Fujiwara *et al.* [9, 10] proposed the dendrite growth method to obtain mc-Si ingots with large grains and fewer GBs by inducing lateral dendrite growth along the crucible wall through controlling the cooling speed at the initial stage of solidification. The process, however, is difficult to control and requires further developments for industrial applications. Instead of growing mc-Si ingot with large grains, it has been shown that the solar cell efficiency can also benefit from the opposite approach, with small grain size and significantly more GBs [11, 12]. It has been suggested that the propagation of dislocation networks can be suppressed by the increased presence of GBs of certain types, which act as alternative sites for stress release [11, 13]. Material developed based on this concept contains smaller grains, larger amounts of GBs, and lower numbers of dislocation clusters. It is commonly referred as 'high performance' multicrystalline silicon, and is now being deployed in mc-Si solar cell production, with its market share expected to increase dramatically in the future. The international technology roadmap for photovoltaic (ITRPV) [1] predicted that 'high performance' mc-Si will completely replace conventional mc-Si by 2020.

On the other hand, while most solar cells today are based on boron doped p-type silicon, phosphorus doped n-type silicon has attracted increasing attention in the solar industry recently. N-type monocrystalline silicon solar cells with efficiencies at or above 25% have been reported by Sunpower [14, 15] and Panasonic [16]. A major advantage of n-type silicon is that it does not suffer from light-induced boron-oxygen-related-degradation [17, 18], as opposed to widely used boron doped Czochralski-grown (Cz) silicon. N-type silicon also has higher tolerance to metal impurity contamination than p-type silicon [19], potentially making it very suitable for mc-Si material which tends to inherently contain higher metal contents. N-type mc-Si material therefore has the potential for low cost high efficiency solar cells, although it has not been implemented in industry.

Crystal defects such as GBs and dislocations significantly affect the efficiency of mc-Si solar cells. They can act as strong recombination centres for excess carriers, and hence can locally reduce the minority carrier lifetime. The recombination behaviour of crystal

defects depends on the structure and geometry of the defects, the contamination levels in the material, and their interactions [5, 20-27]. Although crystal defects have been studied extensively in the literature, their underlying recombination mechanisms are still not fully understood. Furthermore, it is also important to consider the influence of phosphorus gettering and hydrogenation when evaluating the detrimental influence of crystal defects on solar cell performance, given that gettering and hydrogenation are incorporated in common solar cell fabrication steps during the formation of pn junctions and firing of metal contacts. It has been shown that the recombination behaviour of crystal defects changes after gettering [20, 23, 24, 28, 29] and hydrogenation [29-32]. Understanding the recombination behaviour of crystal defects and their response to those two processes is important, as it allows the possibilities of identifying performance limiting crystal defects and mitigating their detrimental effects during cell production.

Moreover, apart from recombination through crystal defects within the bulk, recombination at surfaces acts as another significant loss mechanism in solar cells. Reducing the rate of surface recombination is essential for solar cells. The majority of the current studies on surface passivation focus on monocrystalline silicon wafers. The effectiveness of surface passivation in mc-Si material is less clear due to the random crystal orientation in mc-Si. It has been reported that the passivation effectiveness for certain dielectric films, such as silicon dioxide [33] or amorphous silicon [34, 35], can indeed be influenced by the surface orientation.

This thesis aims to broaden the existing knowledge concerning various recombination mechanisms in mc-Si. Owing to the inhomogeneity in mc-Si material, spatially resolved characterisation tools are required to study mc-Si. This was traditionally performed by mapping techniques such as microwave-detected photoconductance decay lifetime mapping (μ-PCD), electron beam induced current (EBIC) and light beam induced current (LBIC). However, such mapping techniques are normally either time-consuming or require a solar cell structure with metal contacts. In this work, we apply the photoluminescence (PL) imaging technique to study recombination behaviours in mc-Si. Major advantages of the PL imaging technique are that the measurement is rapid, applicable to large area, and does not require a cell structure or a pn junction. These

advantages allow our analysis to be performed based on a large sample size, which is otherwise difficult to obtain with mapping techniques.

## 1.1 Thesis outline

Chapter 2 outlines fundamental concepts and experimental techniques that are used throughout this thesis. The concept of carrier lifetime is first introduced, followed by a review of various recombination mechanisms occurring in semiconductors relating to the operation of a solar cell. The main characterisation techniques used in this thesis are then described, namely, the quasi-steady-state photoconductance (QSSPC) lifetime measurement technique, PL imaging, and Electron back-scatter diffraction (EBSD). Special attention is paid to discuss the operating principles of the PL imaging technique, along with its associated measurement artefacts and methods for reducing their impact.

Chapter 3 demonstrates a new approach for converting PL images into calibrated carrier lifetime images for silicon wafers with inhomogeneous lifetime distributions such as mc-Si wafers. The method is based on an optically-corrected calibration factor extracted from PL and QSSPC measurements on a separate calibration wafer with homogeneous lifetime. The principle of the method is first explained, and then is verified experimentally using a set of monocrystalline silicon wafers with different doping, thickness and reflectivity. A mc-Si wafer is used to demonstrate the difference between the conventional calibration approach, where the PL signal is calibrated against a QSSPC measurement on the test sample itself, and our proposed method. Factors affecting the accuracy of the calibration processes are also discussed. The proposed calibration method developed in this chapter is used throughout the remainder of the thesis.

Chapter 4 focuses on GBs in mc-Si. The chapter presents a method based on PL imaging and modelling of the PL intensity across a GB using two-dimensional finite element analysis, to quantify the recombination strength of a GB in terms of the effective surface recombination velocity ($S_{GB}$). The surface recombination velocity ($S_{GB}$) represents the intrinsic recombination properties of a GB in absolute terms, and does not depend on other parameters such as the lifetime of the intra-grain regions, in contrast to the commonly used signal contrast methods [5] for investigating GBs. The

details of the modelling are first described. The method is then demonstrated on double-side passivated mc-Si wafers, both before and after phosphorus gettering, and single-side passivated wafers with a strongly non-uniform carrier density profile depth-wise. The sensitivity limits and other practical constraints of the method are also discussed.

Chapter 5 applies the model developed in chapter 4 to compare the recombination properties of a large number of GBs in p-type boron doped multicrystalline silicon wafers with different contamination levels, and investigate their response to phosphorus gettering and hydrogenation, aiming to obtain a better understanding of the origin of the recombination activities of GBs. Wafers from three different sections of a commercially grown p-type mc-Si ingot are studied. The different positions in the ingot lead to large differences in the amount of metallic impurities in the wafers. The injection dependent recombination behaviour of GBs is investigated as different decorating impurities may give rise to different injection dependent recombination properties [19]. In addition to band-to-band PL imaging, sub-bandgap PL emitted from several selected GBs is also studied through applying micron scale photoluminescence spectroscopy technique at low temperature ($79\ K$). Lastly, the detrimental influence of GBs on solar cell devices is discussed with the aid of numerical simulations.

Chapter 6 is an extension of the previous chapters, combining the techniques and knowledge developed earlier to assess the electrical properties of various types of mc-Si materials and identify the main performance limiting factors in mc-Si solar cells. The chapter compares the recombination properties of conventionally solidified p-type and n-type mc-Si wafers, and also the recently developed high performance p-type mc-Si wafers. Three distinct regions of the wafers are examined in detail. These are the intra-grain regions, the GBs, and the dislocation networks, along with their response to phosphorus gettering and hydrogenation. The electrical properties of intra-grain regions are assessed based on both the minority carrier lifetime and diffusion length. The recombination activities of GBs are compared quantitatively in terms of their effective surface recombination velocities, using methods presented in Chapter 4. The recombination behaviour of dislocations is evaluated qualitatively based on PL images.

Chapter 7 applies the PL imaging technique to explore surface recombination in silicon wafers with different surface dielectric films. The chapter begins with applying PL

imaging to thin, chemically polished and unpassivated mc-Si wafers. It is found that the PL intensity from such wafers is dominated by surface recombination, which in turn is crystal orientation dependent. An approach for monitoring crystal orientations in mc-Si wafers based on this correlation is proposed. The work is then extended to passivated wafers. Two approaches for evaluating the influence of crystal orientation on surface passivation are presented. The orientation dependent passivation effect of thermally grown silicon oxide films is investigated through the proposed methods.

Chapter 8 summaries the results from previous chapters and suggests possible further works.

# Chapter 2

# Carrier recombination in crystalline silicon and characterisation techniques

## 2.1 Carrier recombination in crystalline silicon

Solar cells operate by directly converting light energy into electrical energy. When silicon is illuminated by light, photons with energy larger than the silicon bandgap are absorbed. This provides energy for electrons to be excited from the valence band to the conduction band, creating excess electron-hole pairs. The excess electrons and holes are then collected at the metal contacts and fed to an external circuit. The excess carriers are only able to exist for a limited time owing to electron-hole recombination, a process in which excited electrons are relaxed back from the conduction band to the valence band by releasing energy, resulting in the destruction of electron-hole pairs. Carriers that recombine before reaching the metal contacts cannot contribute to the solar cell output. The term 'minority carrier lifetime' of a semiconductor, denoted by τ, is the average time a minority carrier can stay in an excited state after electron-hole generation before recombining. For p-type silicon, it is given by:

$$\tau_n = \frac{\Delta n}{U} \qquad (2.1)$$

Where $\tau_n$ denotes the minority carrier (electron) lifetime. $\Delta n$ is the excess minority carrier concentration and $U$ is the recombination rate.

The minority carrier lifetime is one of the most important parameters for solar cells. It is an intrinsic property of a material, reflecting its electrical quality. The minority carrier lifetime is sometime referred as 'recombination lifetime' and is usually the combined

result of various independent recombination processes. There are three main fundamental recombination mechanisms in silicon, namely radiative recombination, Auger recombination and recombination through defects.

## 2.1.1 Radiative recombination

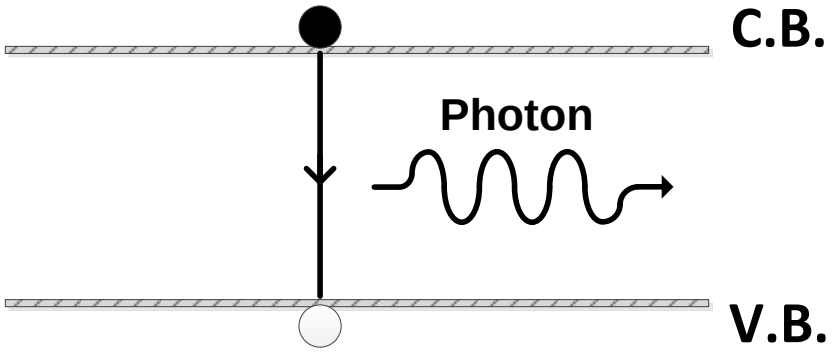


**Figure 2.1 – The electron-hole interaction for radiative recombination.**

Radiative recombination is the reverse of the optical absorption process described above [36]. An electron in the conduction band recombines with a hole in the valence band. During the process, a photon with energy equal to the bandgap of the material is emitted. The net radiative recombination rate $U_{rad}$ is proportional to the product of both the electron and hole concentrations. Assuming charge neutrality ($\Delta n = \Delta p$), it is given as:

$$U_{rad} = B_{rad} \times (pn - {n_i}^2) \approx B_{rad} \times \left(N_{A/D} + \Delta n\right) \times \Delta n \qquad (2.2)$$

Where $n$ and $p$ are the electron and hole concentrations, and $B_{rad}$ the radiative recombination coefficient. $N_{A/D}$ is the density of acceptors and donors respectively. $B_{rad}$ can be calculated from the absorption coefficient for band-to-band transitions and is found to be $4.73 \times 10^{-15}\ cm^3 s^{-1}$ at $300\ K$ in crystalline silicon [37]. Substituting equation 2.2 into equation 2.1, the radiative recombination lifetime is given by:

$$\tau_{rad} = \frac{1}{B_{rad} \times \left(N_{A/D} + \Delta n\right)} \qquad (2.3)$$

In direct semiconductors, such as GaAs, radiative recombination is a significant recombination mechanism. Radiative recombination can be, in some cases, preferable

and is utilised for light-emitting diode (LED) or laser applications. In indirect semiconductors, such as silicon, the rate of radiative recombination is extremely low when compared to Auger recombination and recombination through defects. Thus it is unlikely to impact the overall recombination lifetime. Nevertheless, radiative recombination is utilised in various characterisation techniques in silicon and other semiconductor materials. One of the examples is the photoluminescence (PL) imaging technique, which is the primary characterisation tool used in this thesis.

## 2.1.2 Auger recombination

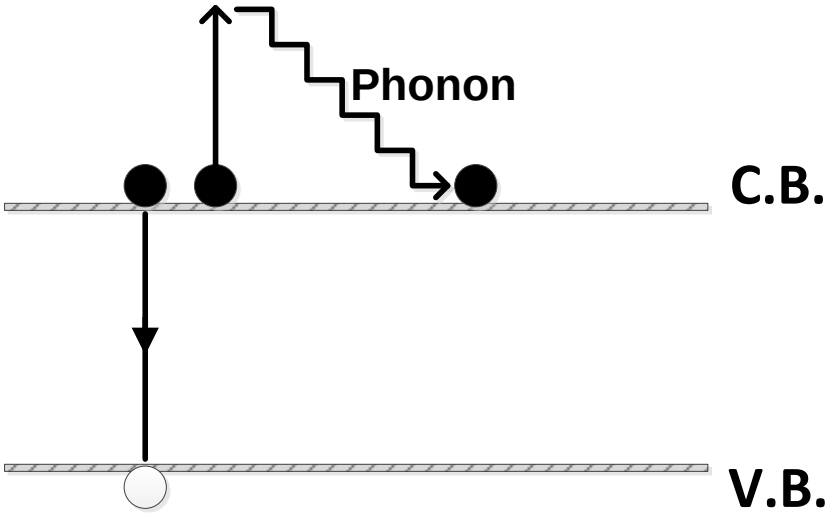


**Figure 2.2 – Auger recombination with the associated excess energy given to an electron in the conduction band.**

Auger recombination occurs when an electron recombines with a hole by releasing the excess energy to a third charge carrier (either an electron in the conduction band or a hole in the valence band) [36]. The kinetic energy given to the third charge carrier is lost as phonons (heat) as the excited carrier relaxes to its original energy state via 'thermalisation'. For Auger recombination, three charge carriers, either two electrons and a hole or two holes and an electron, are involved. Hence, the recombination rate is proportional to the product of the concentrations of all three carriers. The net Auger recombination rate $U_{Aug}$ is given as:

$$U_{Auger} = C_n \times (n^2 p - {n_i}^2) + C_p \times (np^2 - {n_i}^2) \qquad (2.4)$$

Where $C_n$ and $C_p$ are the Auger recombination coefficients. $C_n \times (n^2p - {n_i}^2)$ represents recombination processes involving two electrons and one hole. $C_p \times (np^2 - {n_i}^2)$ represents recombination processes involving two holes and one electron. Early values for the Auger recombination coefficients are those reported by Dziewior and Schmid [38] with $C_n = 2.8 \times 10^{-31}\, cm^6 s^{-1}$ and $C_p = 9.9 \times 10^{-32}\, cm^6 s^{-1}$. The Auger recombination lifetime can be expressed as:

For n-type material:

$$\tau_{Auger} = \frac{1}{C_n(N_D + \Delta n)^2 + C_p(N_D + \Delta n)\Delta n} \quad (2.5)$$

For p-type material:

$$\tau_{Auger} = \frac{1}{C_p(N_A + \Delta n)^2 + C_n(N_A + \Delta n)\Delta n} \quad (2.6)$$

Note that equations 2.4 - 2.6 only provide simplified expressions for Auger recombination. In reality, Auger recombination is more complex. Factors such as Coulomb interactions between charge carriers [39, 40] and phonon participation [41, 42] can all impact on the Auger recombination rate, making it difficult to theoretically determine the Auger recombination parameters. Thus, an empirical parameterisation based on experimental measured lifetimes is often used instead to describe the Auger recombination rate, such as those determined by Kerr and Cuevas [43] and Richter *et al*. [44].

It should be noted that both radiative recombination and Auger recombination are due to intrinsic physical processes in the material, hence their presence is unavoidable [45]. However, unlike radiative recombination, Auger recombination often contributes significantly to the overall effective lifetime in silicon, particularly at high injection levels, or in the heavily doped regions of solar cells, in which the recombination is sometime referred as emitter recombination. At lower injection levels, especially for mc-Si with relatively high impurity or defect content, the carrier lifetime is usually limited by recombination through defects, as described in the following section.

### 2.1.3 Recombination through bulk defects

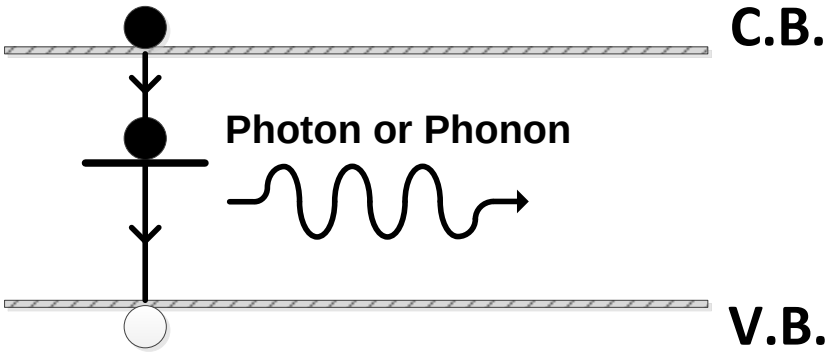


**Figure 2.3 – Two step recombination process through a defect level within the forbidden gap of a semiconductor.**

Crystal defects and impurities introduce energy states or so-called defect levels within the silicon bandgap. These defect levels enable a very effective two-step recombination process in which a free electron in the conduction band first makes a transition into the defect level and then relaxes into the valence band through recombining with a hole [36]. During the transitions, the excess energy is dissipated as phonons (or in some cases as photons). The recombination rate depends on the electron and hole concentrations, as well as the properties of the defects, and their densities. The net recombination rate can be modelled by Shockley-Read-Hall (SRH) statistics [46, 47] and, for a single defect level, is given as:

$$U_{SRH} = \frac{\nu_{th} N_T (np - {n_i}^2)}{\frac{n + n_1}{\sigma_p} + \frac{p + p_1}{\sigma_n}} = \frac{np - {n_i}^2}{\tau_{p0}(n + n_1) + \tau_{n0}(p + p_1)} \qquad (2.7)$$

$\tau_{p0}$ and $\tau_{n0}$ are the capture time constants of electrons and holes and are given as:

$$\tau_{p0} = \frac{1}{N_T \sigma_p \nu_{th}}, \qquad \tau_{n0} = \frac{1}{N_T \sigma_n \nu_{th}} \qquad (2.8)$$

Where $\sigma_n$ and $\sigma_p$ are the capture cross sections of electrons and holes, $\nu_{th}$ is the thermal velocity of the charge carriers, and $N_T$ denotes the density of the defect.

$n_1$ and $p_1$ are the electron and hole densities when the Fermi level coincides with the energy level of the defect ($E_T$), and are given by:

$$n_1 = N_C \exp(\frac{E_T - E_C}{kT}), \qquad p_1 = N_V \exp(\frac{E_C - E_G - E_T}{kT}) \tag{2.9}$$

Where $N_C$ and $N_V$ are the effective densities of state at the conduction and valence band edges. $E_C$ and $E_G$ are the conduction band and band-gap energies. The SRH lifetime is given as:

$$\tau_{SRH} = \frac{\Delta n}{U_{SRH}} \tag{2.10}$$

The SRH statistics can be used to model the recombination behaviour of a given impurity. Table 2.1 summarises the energy level and the electron and hole capture cross sections of several commonly found point-like metal impurities in silicon.

**Table 2.1 – Recombination parameters of various commonly found point-like metal impurities in crystalline silicon at room temperature. Int. and Sub. denote interstitial and substitutional impurities respectively. D. Donor and D. Acceptor denote double donor and double acceptor respectively.**

| Impurity | Lattice site | Type | Energy ($eV$) | $\sigma_n$ ($cm^2$) | $\sigma_p$ ($cm^2$) | Ref. |
|---|---|---|---|---|---|---|
| **Cr** | Int. | Donor | $E_C - 0.24$ | $2.4 \times 10^{-14}$ | $0.8 \times 10^{-14}$ | [48] |
| **Fe** | Int. | Donor | $E_V + 0.38$ | $1.3 \times 10^{-14}$ | $7.0 \times 10^{-17}$ | [49, 50] |
| **Ti** | Int. | D. Donor | $E_V + 0.26$ | $1.5 \times 10^{-15}$ | $3.7 \times 10^{-17}$ | [51] |
| **Au** | Sub. | Acceptor | $E_C - 0.55$ | $1.4 \times 10^{-16}$ | $7.6 \times 10^{-15}$ | [52] |
| **Zn** | Sub. | Acceptor | $E_V + 0.33$ | $1.5 \times 10^{-15}$ | $4.4 \times 10^{-15}$ | [53] |
| | Sub. | D. Acceptor | $E_C - 0.47$ | $1.3 \times 10^{-19}$ | $6.6 \times 10^{-15}$ | [53] |

Note that SRH recombination behaviour is often strongly injection dependent and can be significantly different in p-type and n-type silicon, depending on the electron and

hole capture cross sections of the defects. Interstitial iron is one of the most commonly found metal impurities in mc-Si, it exhibits a deep level within the silicon bandgap and has a much higher electron capture cross-section than hole capture cross-section. Figure 2.4 shows the simulated SRH recombination lifetime for p-type and n-type silicon (with a background doping of $1 \times 10^{12}\ cm^{-3}$) containing $1 \times 10^{12}\ cm^{-3}$ of interstitial iron. The SRH statistics suggest that interstitial iron has a more detrimental influence in p-type silicon than n-type silicon at low injection levels, which is in agreement with experimental observations [19].

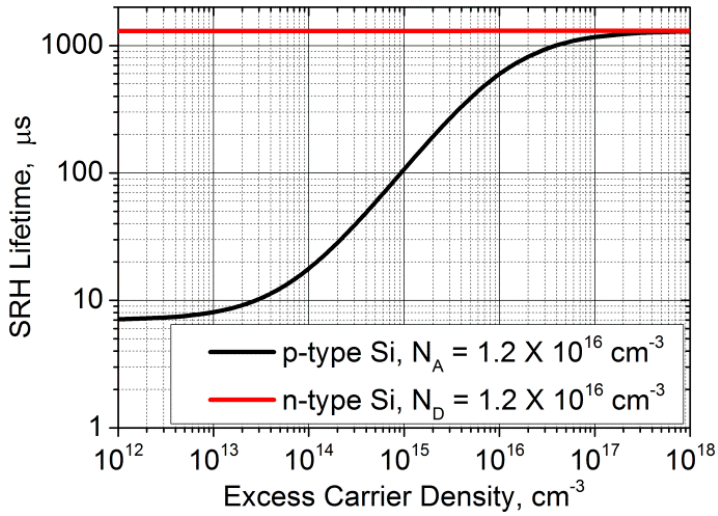


**Figure 2.4 – Simulated SRH recombination lifetime for p-type and n-type silicon containing $1 \times 10^{12}\ cm^{-3}$ of interstitial iron.**

## 2.1.4 Surface recombination

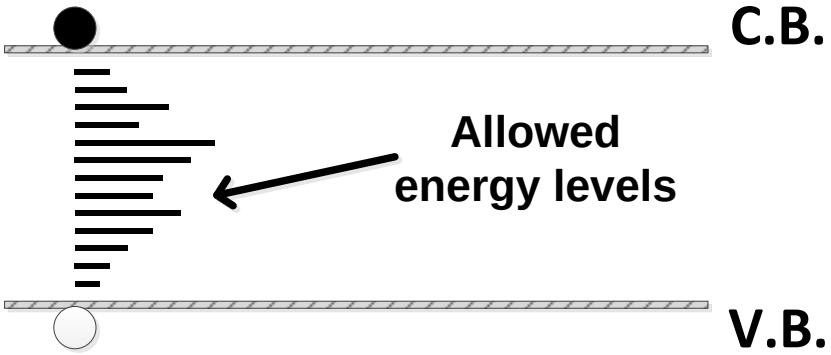


**Figure 2.5 – Surface or defect states lying within the forbidden gap of a semiconductor at the surfaces or grain boundaries of a semiconductor.**

The surfaces of silicon represent a severe discontinuity in the crystal lattice, resulting in a large number of unsaturated ('dangling') bonds [54]. Some of these dangling bonds can give rise to a large density of defect levels within the silicon bandgap, facilitating recombination. Unlike bulk SRH centres described above, these defect levels do not usually occupy a single energy state, but rather exist as many allowed states distributed throughout the bandgap, as shown in Figure 2.5. In principle, the rate of surface recombination can also be modelled using SRH statistics [46, 47], through replacing $N_T$ with $D_{it}(E)$ (the density of interface traps at a given energy) and integrating over the entire bandgap [55]:

$$U_S = \int_{E_V}^{E_C} \frac{v_{th}(n_s p_s - {n_i}^2)}{\frac{n_s + n_1}{\sigma_p(E)} + \frac{p_s + p_1}{\sigma_n(E)}} D_{it}(E) dE \qquad (2.11)$$

Where $n_s$ and $p_s$ are the surface concentrations of electrons and holes. $\sigma_n(E)$ and $\sigma_p(E)$ are the electron and hole capture cross sections for each defect level. While equation 2.11 is comprehensive, determining the energy dependent $D_{it}(E)$, $\sigma_n(E)$ and $\sigma_p(E)$ is not trivial. It is more typical to describe the overall surface recombination rate in terms of the effective surface recombination velocity $S_{eff}$ according to:

$$U_S = S_{eff} \Delta n_s \qquad (2.12)$$

Where $\Delta n_s$ is the excess carrier concentration at the surface. The effective surface recombination velocity $S_{eff}$ combines all surface defect parameters described in equation 2.11 into one single parameter, which is very useful for quantifying and comparing surface recombination. Note that owing to the nature of SRH statistics [46, 47], as shown in the previous section, $S_{eff}$ can be injection dependent.

Analysing the impact of surface recombination on the overall effective lifetime (Section 2.1.6) can be complicated, as it depends not only on the surface conditions, but also other factors such as the bulk lifetime. A detailed analysis can be found in Aberle [55]. For a special case where the excess carrier concentration is uniform depth-wise throughout the sample, a condition that usually applies when the bulk lifetime is high

and $S_{eff}$ is small, the overall effective lifetime can be related to the effective surface recombination velocity according to:

$$\frac{1}{\tau_{eff}} = \frac{1}{\tau_b} + \frac{2S_{eff}}{W} \quad (2.13)$$

Where $\tau_b$ is the bulk lifetime and $W$ the sample thickness. Based on equation 2.13, one can extract the $S_{eff}$ value of certain passivating layers from an effective lifetime measurement. The method is described in detail in Chapter 7, in which the influence of crystal orientation on surface recombination is investigated.

## 2.1.5 Grain boundary recombination

Grain boundaries (GBs) are interfaces separating two dissimilarly oriented crystals (grains) of the same phase in polycrystalline materials. In addition to dangling bonds at the interface, metal impurity decoration at GBs also leads to localised defect states within the silicon bandgap, which act as recombination centres for carriers. The recombination behaviour of GBs is similar to those at surfaces. Equation 2.12 can be applied to describe GB recombination. However, owing to the fact that GBs are located locally within the bulk rather than at the surfaces, extracting the recombination rate of GBs is more complex and cannot be done using a simple expression like equation 2.13. A method for determining the effective surface recombination velocity of a GB ($S_{GB}$) based on PL imaging technique is presented in Chapter 4. This section outlines fundamental concepts and terms relating to descriptions of the GB geometry. It has been shown that the recombination properties of a GB are strongly influenced by its geometry [5, 20, 31].

### 2.1.5.1 Grain boundary geometry

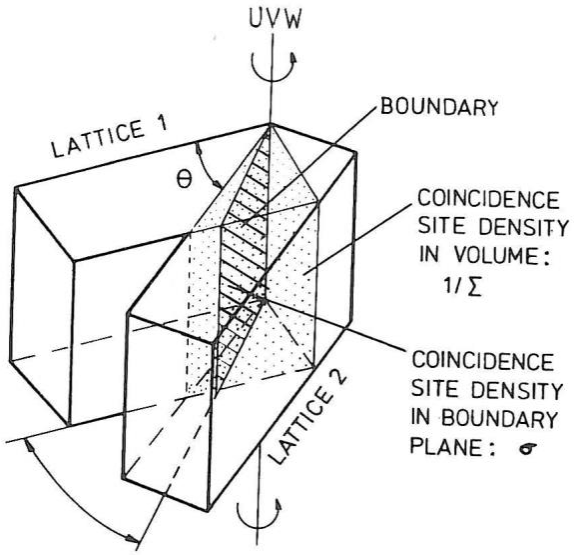


**Figure 2.6 – A schematic illustration of two crystal lattices forming a GB, assuming the lattices are able to interpenetrate each other (figure adapted from Randle [56]).**

Figure 2.6 shows a schematic illustration of two crystal lattices forming a GB. To visualise a GB, the two grains are assumed to be able to interpenetrate each other. A GB has five macroscopic degrees of freedom and therefore requires five parameters to fully define its geometry. The first three degrees of freedom describe the orientation relationship of the two neighbouring grains forming the GB. Lattice 2 can be imagined as a rigid body rotation of lattice 1, that is, the relative position of lattice 2 can be achieved by rotating lattice 1 through a certain angle along with a specific axis. These axis [UVW] and angle (θ) are referred as the axis and angle of misorientation of a GB. Note that the axis/angle description alone does not fully define the geometry of a GB, but only the orientation relationship with the neighbouring grains. A GB can located anywhere within the interpenetrating region (dotted volume in Figure 2.6). The actual position of the GB plane, defined by the coordinates of its normal with respect to one of the grains ($N_1$ *or* $N_2$), takes up the remaining two degrees of freedom, combined with the axis/angle description, to fully describe the geometry of a GB.

Although five degrees of freedom are required to fully define a GB, it is common to describe a GB only in terms of the relative orientation of the neighbouring grains, ignoring the position of the GB plane. This is because the misorientation angle/axis

description is directly related to frequently used data analysis methods such as the Coincidence Site Lattice (CSL) classification, as explained below. Moreover, the determination of the GB plane is generally more difficult and requires extra sample preparation, as shown in the succeeding section (Section 2.2.3).

### 2.1.5.2 Coincidence Site Lattice

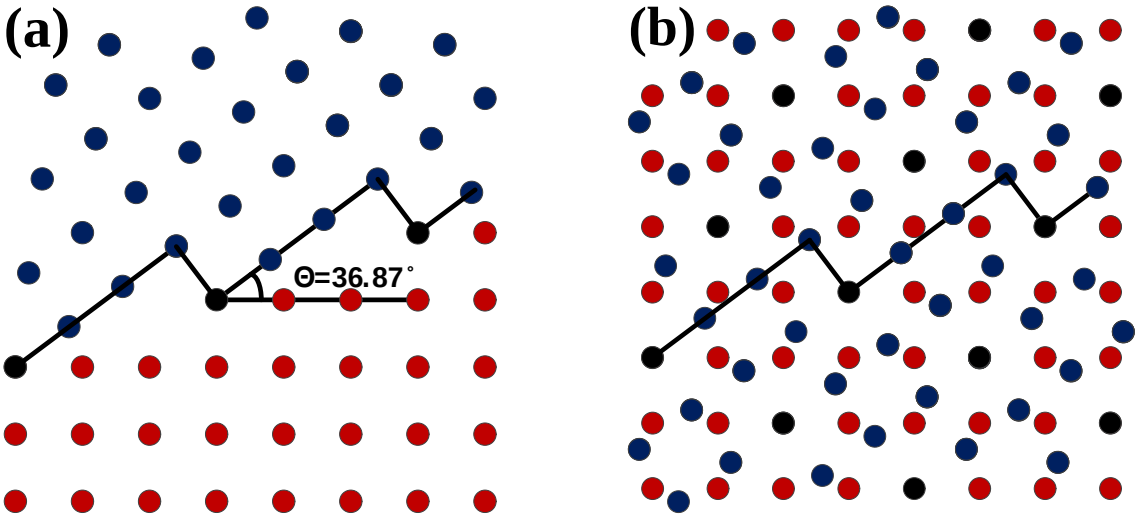


**Figure 2.7 – (a) A GB formed by two lattices misoriented by 36.87° along the axis [100]. (b) Superposition of the two lattices in (a), assuming atoms from both lattices can interpenetrate into each other. The atoms from lattice 1 and 2 are represented by red and blues circles respectively. Black circles denote coincident sites where the atoms from both lattices overlap.**

The coincidence site lattice (CSL) scheme is one of the most commonly used models for the categorisation of GBs. A GB, in principle, can be constructed with any random combinations of misorientation angle/axis. CSL GBs belong to a subset of GBs which have a special geometry, with certain specific combinations of misorientation axis/angle. These specific combinations of misorientation axis/angle introduce periodically coincident sites in the interfacing lattice. CSL GBs are classified by its associated sigma (Σ) notation, where Σ is the reciprocal density of the coincident sites. The concept of CSL can be illustrated using two interpenetrating lattices. Figure 2.7(a) shows a GB formed by two lattices misoriented by 36.87° along the axis [100], view down from the top. [100] is perpendicular to the plane of the paper. The atoms from lattice 1 and 2 are represented by red and blue circles respectively. Upon superposition of these two crystals (imagining atoms from both lattices can interpenetrate into each other), there

will be some coincident sites where the atoms from both lattices overlap, denoted as black circles in Figure 2.7(b). It can be seen that, for this chosen pair of misorientation axis/angle ([100]/36.87°), every fifth position in the lattice is a coincident site. GBs formed by this misorientation configuration are denoted as CSL Σ5 GBs. Table 2.2 outlines the angle and axis of misorientation for the most frequently found CSL GBs in mc-Si [56, 57].

**Table 2.2 – Angle and axis of misorientation for frequently found CSL GBs in mc-Si [56, 57].**

| Σ | $\boldsymbol{\theta}$° | $\boldsymbol{UVW}$ |
|---|---|---|
| **3** | 60° | [111] |
| **9** | 38.94° | [110] |
| **27*a*** | 31.58° | [110] |
| **27*b*** | 35.42° | [210] |

Note that the CSL model only describes the misorientation between the neighbouring grains forming the GB, but not the actual positon of the grain boundary plane. The position of the boundary plane governs the density of coincident sites that actually occur in the GB plane itself (denoted as σ in Figure 2.6), which is more physically related to their electrical properties compared to the overall lattice coincidence (represented by the Σ value) [56, 58, 59]. A high density of coincident sites in the boundary plane is necessary for the formation of a low energy interface structure [60, 61]. The significance of the CSL model is that the periodic coincidence in the GB plane can only be reproduced if the two interfacing lattices contain coincident sites, or in another word, if the GB is a CSL GB. However, a Σ3 GB does not necessarily guarantee a high density of coincident sites in the boundary plane as it also depends on the position of the boundary plane. It has been reported that Σ3 {110} or Σ3 {112} GBs are much more recombination active than Σ3 {111} GBs [62, 63]. Randle [60] suggested that the CSL and Σ notation is only meaningful if there is a high density of coincident sites in the grain boundary plane. Moreover, CSL GBs only represent a portion of the total GBs. In an actual mc-Si sample, there is a large number of GBs that cannot be classified according to the CSL index, as they do not contain any coincident sites. Such GBs, often denoted as random angle (RA) GBs, also have a strong influence on the electrical properties of mc-Si materials and hence should not be neglected.

## 2.1.6 The effective lifetime

Within the silicon bulk, radiative, Auger and SRH recombination mechanisms occur simultaneously in parallel. The total bulk recombination rate is the sum of each individual recombination rate.

$$U_{bulk} = U_{rad} + U_{Auger} + U_{SRH} \tag{2.14}$$

The bulk lifetime can be expressed as:

$$\frac{1}{\tau_b} = \frac{1}{\tau_{rad}} + \frac{1}{\tau_{Auger}} + \frac{1}{\tau_{SRH}} \tag{2.15}$$

The overall effective lifetime depends on both the bulk lifetime and the surface properties and is given as:

$$\frac{1}{\tau_{eff}} = \frac{1}{\tau_b} + \frac{1}{\tau_s} \tag{2.16}$$

Where $\tau_s$ is the equivalent 'surface lifetime'. In actual solar cells or diffused samples, there is a heavily doped region or regions at the surfaces of the silicon. Auger recombination in the heavily doped region, so-called emitter recombination, could also impact the effective lifetime. For such samples, equation 2.16 is modified as:

$$\frac{1}{\tau_{eff}} = \frac{1}{\tau_b} + \frac{1}{\tau_{emitter}} \tag{2.17}$$

Where $\tau_{emitter}$ is the equivalent recombination lifetime in the heavily doped region, including the influence of surface recombination.

The effective lifetime combines different recombination mechanisms and represents the overall recombination properties of a material, hence is directly related to the solar cell performance. The effective lifetime can be directly measured with various lifetime measurement techniques, as described in detail below. However, care must be taken when interpreting the effective lifetime. For example, when evaluating bulk defects, it is

necessary to ensure that the measured effective lifetime is not limited by surface recombination.

Different recombination mechanisms exhibit distinctive injection dependence, hence their impacts on the effective lifetime vary significantly at different injection levels. At low injection, the effective lifetime is usually dominated by SRH recombination, especially in mc-Si which contains a relatively high defect content. The impact of SRH recombination on the effective lifetime decreases at high injection levels, in which the effective lifetime is often limited by Auger recombination. At moderate injection levels, both SRH, emitter and surface recombination contribute to the effective lifetime, with their relative significance depending on their actual recombination parameters, such as the impurity content, the surface recombination velocity or the diffusion profile. As mentioned above, radiative recombination is generally negligible when compared to these other recombination mechanisms.

Note also that the effect of GB recombination is not easily incorporated in the above representation. This is due to the fact that unlike other bulk recombination mechanisms, which occur uniformly within the bulk, GB recombination occurs locally at certain regions within the bulk. Their contribution to the overall lifetime performance depends on various other parameters such as the spatial distribution of the GBs, and the diffusion length of carriers in the bulk, and hence requires equation 2.14 to be implemented in 2 or 3 dimensions. The overall influence of GB recombination on solar cell performance is discussed in more detail in Chapters 5 and 6.

## 2.2 Characterisation techniques

This section introduces characterisation techniques that are used throughout this thesis for evaluating carrier recombination in mc-Si.

### 2.2.1 Quasi-steady-state photoconductance lifetime measurements

Quasi-steady-state photoconductance (QSSPC) lifetime measurements, developed by Sinton and Cuevas [64], is a specific type of photoconductance based technique which

allows the injection dependence of the minority carrier lifetime to be explicitly determined. It is rapid, non-destructive and does not require a cell structure with metal contacts, making it very suitable for characterising silicon wafers. It determines the minority carrier lifetime by measuring the increase in the conductance of an illuminated sample caused by photo-generated excess carriers. The excess conductance $\Delta\sigma$ is related to the excess carrier density by:

$$\Delta\sigma = q\left(\mu_p \Delta p + \mu_n \Delta n\right) W \tag{2.18}$$

Where $q$ is the electron charge. $\Delta n$ and $\Delta p$ are the average carrier densities of the photo-generated electrons and holes, and $\mu_p$ and $\mu_n$ are the hole and electron motilities, which can be determined from a suitable carrier density dependent mobility model [65, 66]. In the absence of minority carrier trapping, as described in detail below (Section 2.2.1.1), it is possible to assume equal excess carrier concentrations for electrons and holes ($\Delta n = \Delta p$). In such a case, the average excess carrier concentration can be expressed as:

$$\Delta n = \frac{\Delta\sigma}{q\left(\mu_p + \mu_n\right) W} \tag{2.19}$$

Based on the continuity equation, the net rate of change of excess carrier concentration equals the difference between the light induced generation rate and the recombination rate:

$$\frac{d\Delta n}{dt} = G - U \tag{2.20}$$

Rearranging for $U$ and substituting it into equation 2.1 yields:

$$\tau_{eff} = \frac{\Delta n}{G - \frac{d\Delta n}{dt}} \tag{2.21}$$

In QSSPC lifetime measurements, a slowly decaying light source is used to illuminate the sample. If the decay is slow enough to ensure that the rate of change of excess

carrier concentration is negligible compared to the generation rate, then steady state effectively prevail. Under such conditions, equation 2.21 becomes:

$$\tau_{eff} = \frac{\Delta n(t)}{G(t)} \tag{2.22}$$

Upon the slowly decaying illumination, $\Delta n$ at each time step can be determined from each measured value of $\Delta\sigma$, which then can be used to calculate the effective lifetime based on equation 2.22, given that the generation rate is known. The generation rate can be calculated based on the optical properties of the sample and the incident flux, according to:

$$G = \frac{(1 - R_f) \times \phi}{W} \tag{2.23}$$

Where $\phi$ and $R_f$ are the incident photon flux as measured by a calibrated reference cell, and the reflectivity of the front surface. In this work, a Sinton Instruments WCT-120 lifetime tester is used for performing QSSPC lifetime measurements.

#### 2.2.1.1 Minority carrier trapping

QSSPC measurements are simple and straightforward, however, they sometimes suffer from measurement artefacts at low injection, leading to a significant overestimation of the measured lifetime. This section describes one of the most commonly found measurement artefacts in QSSPC measurements when measuring lifetimes in mc-Si wafers: minority carrier trapping effects [3, 4].

Minority carrier trapping is caused by the presence of shallow defect levels, also known as trap levels, within the silicon bandgap. These shallow defect levels have a relatively small capture cross section for majority carriers and hence do not effectively contribute to recombination, as opposed to defect levels described above in Section 2.1.3 . Instead, they capture minority carriers for a certain period of time and then release them back to the band from which they were captured. As a result, a proportion of the light generated minority carriers are trapped within these defect levels. Using p-type silicon as an example to illustrate the influence of such traps, the total number of light generated

electrons equals the sum of electrons in the conduction band and those trapped in the shallow defect states.

$$\Delta n_{generated} = n_t + \Delta n \quad (2.24)$$

Where $\Delta n_{generated}$ is the total light-generated minority carrier concentration. $\Delta n$ represents the electron concentration in conduction band. $n_t$ denotes the concentration of carriers that are trapped within the shallow defect states. Owing to charge neutrality, the total excess carrier concentrations for electrons and holes are equal, and it follows that:

$$\Delta p = \Delta n_{generated} = n_t + \Delta n \quad (2.25)$$

Substituting $\Delta p$ in equation 2.18 and rearranging yields:

$$\Delta\sigma = q\Delta n(\mu_p + \mu_n)W + qn_t\mu_p W \quad (2.26)$$

Comparing equation 2.18 and 2.26, it can be seen that although the traps do not contribute to recombination, they affect the photoconductance of a sample. Owing to the presence of traps, calculating the effective lifetime based on equation 2.18 can lead to a significant overestimation of the lifetime. This is particularly the case at low injection when $n_t$ is comparable to $\Delta n$. Note that the influence of minority carrier trapping depends on the densities and properties of the trap levels, and hence depends strongly on material quality. The effect of minority carrier trapping is more substantial in mc-Si than monocrystalline silicon as mc-Si tends to contain a higher impurity and defect content, which can act as trap levels. The effect of trapping on QSSPC lifetime measurements can be reduced or partially corrected with the use of a "bias-light" term to subtract out the underlying photoconductance due to the traps, as suggested by Sinton [67, 68].

## 2.2.2 Photoluminescence Imaging

Photoluminescence (PL) imaging is a spatially resolved characterisation technique which allows the excess carrier density within a silicon wafer or solar cell to be imaged,

by capturing the spontaneous emission of photons in an optically excited silicon wafer or solar cell with an infrared camera. Given its rapid, non-destructive and contactless nature, it is suitable for a variety of different applications, such as for imaging carrier lifetime [2, 69, 70], series resistance [71, 72], shunt resistance [73, 74], doping density [75], and interstitial iron concentration [49]. A major advantage of PL measurements, in general, is that they are unaffected by measurement artefacts at low injection such as minority carrier trapping [3] and depletion region modulation (DRM) [76] effects, in contrast to photoconductance based methods such as the QSSPC technique. This allows PL-based lifetime measurements to be performed at true low injection levels. In this thesis, PL imaging is applied to evaluate carrier lifetime, GB recombination behaviour and surface recombination in mc-Si. The details of the methods are presented in Chapters 3, 4 and 7 respectively. As a reference, this section describes the basic operating principles of the PL imaging technique and discusses various measurement artefacts which can impact the accuracy of PL measurements.

The PL intensity $I_{PL}$, which is a measure of the spontaneous emission of photons from the semiconductor, is related to the rate of radiative recombination $U_{rad}$. Under steady state conditions, and assuming a uniform carrier profile depth-wise, it is given as:

$$I_{PL} = A \times B_{rad} \times (pn) = A \times B_{rad} \times \left(N_{A/D} + \Delta n\right) \times \Delta n \qquad (2.27)$$

Where $A$ is a scaling factor which can be determined experimentally. Equation 2.27 shows that the measured PL intensity is directly related to the excess carrier density $\Delta n$ in the material. Given that PL intensity is usually measured only in relative units, for quantitative studies, it is often necessary to convert the raw PL signal into an absolute excess carrier concentration. This calibration process requires the determination of the product of $A$ and $B_{rad}$ via an independent method, and it is commonly performed using QSSPC lifetime measurement. The calibration process is described in detail in Chapter 3.

As mentioned above, PL imaging is immune to minority carrier trapping at low injection [77]. This is due to the fact that PL intensity is proportional to the product of $p$ and $n$. As long as the background doping of the sample significantly exceeds the density

of trapped carriers, a condition that is usually satisfied in mc-Si, the influence of trapping is negligible and the emitted PL intensity for samples with or without trapping is identical.

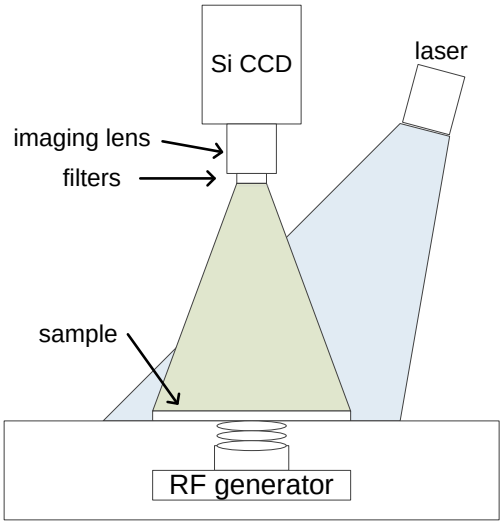


**Figure 2.8 – Schematic of the PL imaging system used in this work.**

PL images in this work were obtained with a BT Imaging LIS-R1 tool. A schematic of the system is shown in Figure 2.8 . A monochromatic laser at 808 nm is used for carrier excitation. The incident photon flux is controlled by varying the applied voltage to the laser and the illumination area (either $165\,mm \times 165\,mm$ or $35\,mm \times 35\,mm$), achieving 0.1 – 10 suns equivalent conditions. PL images were captured with a one megapixel silicon charged-coupled device (CCD) camera, with an acquisition time varying from $0.1\,s$ to $30\,s$. A long pass filter with a cut-off wavelength at $980\,nm$ is equipped in the imaging lens to filter the reflected laser light. Illumination and detection are performed on the same side of the sample. Two sets of imaging lenses were used in this work, a standard lens for general purpose and a high magnification lens for investigating crystal defects. The pixel dimensions of the PL images were around $160\ \mu m$ when using the standard lens and around $22\ \mu m$ when the high magnification lens was used. A Sinton Instruments WCT-120 lifetime tester is equipped within the PL imager to perform QSSPC measurements required for calibrating the PL signal.

In this work, the PL imaging technique is applied to study highly localised features in mc-Si. The PL signal from such samples is influenced by several lateral smearing phenomena in the PL imaging system. These are discussed below.

#### 2.2.2.1 Light scattering within the silicon sensor

The first type of smearing phenomenon is photon scattering within the silicon sensor. The luminescence signal emitted from silicon lies between $900\,nm - 1300\,nm$. The absorption depth of photons in this wavelength range is rather long in silicon. The PL images, therefore, are affected by light-trapping in the silicon CCD sensor, that is, photons entering a certain pixel within the silicon detector are not immediately absorbed. Instead, they travel a significant distance within the sensor and eventually are absorbed in other pixels in the silicon sensor, resulting in a reduction of the image contrast [78]. Since this effect is due to the weak absorptivity of long wavelength light in silicon sensor, the effect can be reduced by filtering out the longer wavelength light [78]. In this work, a short pass filter with a cut off wavelength at $1025\,nm$ (for the standard imaging lens) and $1050\,nm$ (for the magnification lens) are equipped within the imaging lens to reduce the impact of lateral light scattering within the camera's CCD sensor on the captured PL images, therefore producing less blurred images. The use of short pass wavelength, however, unavoidably reduces the overall signal intensity, which can be compensated with a longer exposure time.

On the other hand, Walter *et al.* [79] demonstrated that the photon smearing in the silicon CCD sensor can be quantitatively characterised by imaging the spread of the PL signal from a sub-pixel size point source. The true image can then be approximated by applying image deconvolution using the acquired point-spread function (PSF). In this study, image deconvolution was performed to all the acquired PL images using the Richardson-Lucy (RL) algorithm [80] implemented with ImageJ plugin Deconvolution Lab [81], based on the PSF acquired by Walter *et al.* [79]. It has been shown that while the use of the short-pass filter reduces this photon smearing effect, it can still have some impact on regions with small, high-contrast and localised features [82], such as grain boundaries. Therefore, the use of the PSF is important in this thesis.

This is demonstrated in Figure 2.9, which compares the PL intensity profile across a recombination active grain boundary extracted from PL images taken with and without the use of a short pass filter, before and after applying the PSF. It can be seen that the PL profile is much sharper when captured with a short pass filter due to the reduction of the photon smearing effect in the silicon CCD sensor. Applying image deconvolution

further reduces such effect, improving the contrast of the PL profile. This contrast enhancement process is important for evaluating GB recombination in Chapter 4, in which the surface recombination velocity of a GB is extracted based on the PL intensity profile across the GB.

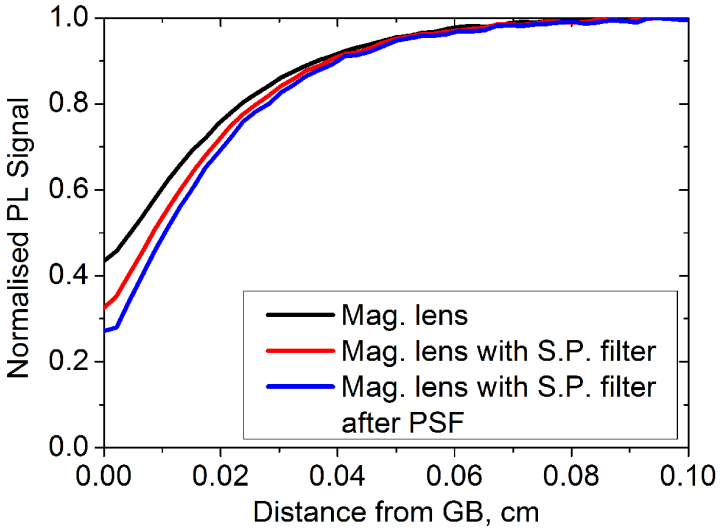


**Figure 2.9 – PL profiles across a recombination active GB extracted from PL images taken with a high magnification lens with and without the use of a short pass filter, and before and after applying the PSF. The PL intensity is normalised against the PL intensity in regions far away from the GB.**

### 2.2.2.2 Light scattering within the sample

Apart from photon scattering within the silicon detector discussed above, the emitted PL can also scatter within the sample before escaping. This results in photons escaping the sample surface at a lateral position different from where they are generated, contributing to blurriness in the images [78]. This effect is particularly significant for textured samples [83]. As a result, only planar samples were studied in this thesis. Similar to photon scattering within the silicon sensor, light scattering within the silicon sample mainly occurs for long wavelength light, hence such effect can also be reduced with the use of a short-pass filter.

### 2.2.2.3 Carrier smearing within the sample

PL images are often converted into effective carrier lifetime images, although they actually represent the distribution of electron and hole concentrations, as can be seen in

equation 2.27. This is due to the fact that the carrier lifetime is a more direct measure of the electrical properties of a material, while the excess carrier concentration depends on the excitation conditions as well as the material properties. The effective lifetime can be calculated from the excess carrier concentration as follows:

$$\tau_{eff} = \frac{\Delta n}{G} \tag{2.28}$$

Where the volumetric generation rate $G$ can be calculated according to equation 2.23.

Equation 2.28 is simple and widely used in the literature. However, it assumes that the lateral diffusion of the minority carriers within the sample is negligible. Such an assumption is not necessarily valid for samples with non-uniform lifetime such as mc-Si wafers, and when the minority carrier diffusion length is larger than the pixel size of the images, which is often the case for well passivated samples. This lateral carrier diffusion can result in a smearing effect in the PL images, and if not accounted for during the conversion of PL images into lifetime images, leads to a higher apparent lifetime in low lifetime regions, and vice versa in high lifetime regions. Note that the lateral carrier diffusion is a real physical effect which occurs during normal solar cell operation. Hence, the smeared PL or excess carrier density images, in some cases, provide a better indication for the performance of a solar cell. However, such smearing effects reduce the accuracy and resolution in studies on the recombination lifetimes, which is the objective of this work.

Phang *et al.* [84] recently proposed a carrier de-smearing technique to correct for the influence of the lateral carrier smearing effect on lifetime images based on the continuity equation. The actual lifetime at each image pixel can be calculated as:

$$\tau_{i,j}(\Delta n_{i,j}) = \frac{\Delta n_{i,j}}{D_{eff}(\Delta n_{i,j}) \times \nabla^2(\Delta n_{i,j}) + G} \tag{2.29}$$

Where $D_{eff}$ is the effective carrier diffusivity [85]. The $D_{eff}(\Delta n_{i,j}) \times \nabla^2(\Delta n_{i,j})$ term represents the carrier injection via diffusion from or to neighbouring pixels. In the case

of negligible lateral diffusion ($\nabla^2(\Delta n_{i,j}) \approx 0$), equation 2.29 converges to equation 2.28.

$\nabla^2(\Delta n_{i,j})$ can be determined from the second derivative of excess carrier density images calibrated from PL images using equation 2.27. Since the method depends on the estimation of the second derivative, it is sensitive to measurement noise and hence noise filtering is required on the PL images before calculating the second derivative. The details of the filtering method are explained in detail in Ref. [84].

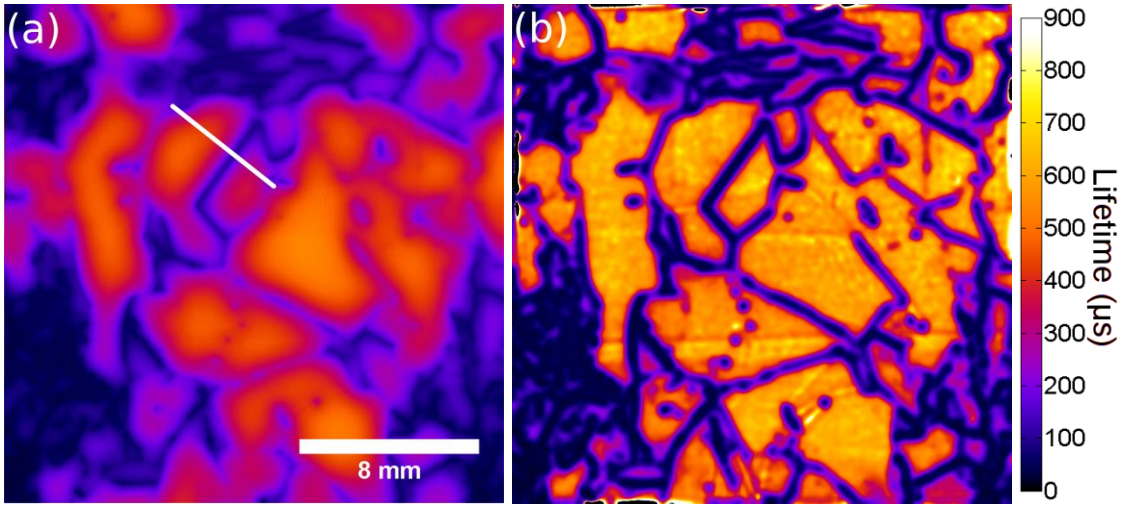


**Figure 2.10 – Application of the carrier de-smearing technique. (a) As measured smeared lifetime calibrated according to equation 2.28, assuming negligible lateral carrier diffusion. (b) De-smeared lifetime calibrated according to equation 2.29, including the influence of lateral carrier diffusion. The same scale is applied on both images.**

The carrier de-smearing technique proposed by Phang *et al.* [84] is used in several sections in this thesis. For demonstration, Figure 2.10 shows lifetime images calibrated with and without the application of the carrier de-smearing technique. It can be seen that the lifetime in the intra-grain regions is more uniform after de-smearing. The carrier smearing effect leads to a significant underestimation of the extracted lifetime values, especially for smaller grains and regions near GBs and other defects. Figure 2.11 shows a line scan of lifetimes across two selected grains in Figure 2.10 (highlighted in white). It reveals that this carrier smearing effect, if not accounted for, limits the apparent lifetime values in these two intra-grain regions to 400 $\mu s$ or below, while in fact the actual lifetimes in the intra-grain regions can reach 600 $\mu s$ or above.

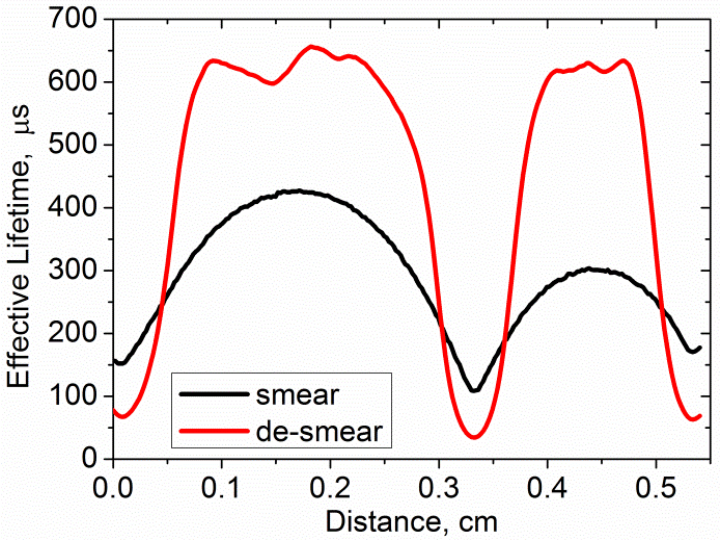


**Figure 2.11 – (a) Smeared and (b) de-smeared lifetime profiles across two selected grains in Figure 2.10 (highlighted in white).**

## 2.2.3 Electron back-scatter diffraction

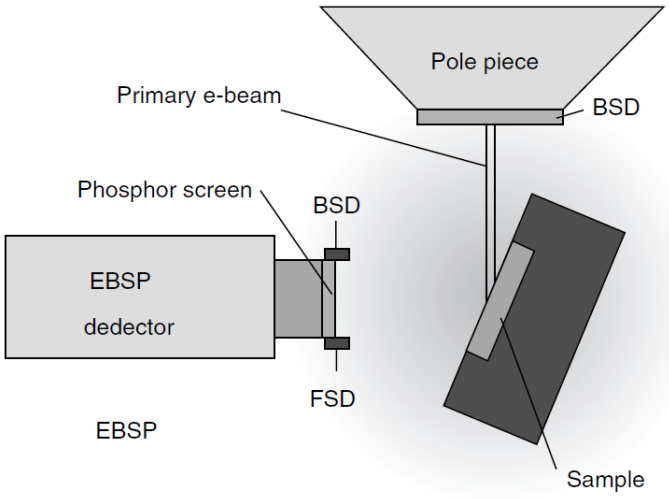


**Figure 2.12 – Schematic diagram for an EBSD system (adapted from Ref. [86]).**

In this work, crystal orientation and GB geometry are mapped by electron back-scatter diffraction (EBSD). EBSD is a scanning electron microscope (SEM) based characterisation technique for determining crystallographic information of samples. A schematic diagram of an EBSD system is shown in Figure 2.12. EBSD operates by capturing the electron diffraction pattern from a highly titled (~70° from horizontal) crystalline sample. When accelerated electrons in the primary beam of the SEM interact

with the titled sample, electrons are scattered and diffracted, and form a pattern that can be detected with a phosphor screen and a low light camera [56, 86]. The diffraction pattern, also known as a Kikuchi pattern, is characteristic of the structure and orientation of the crystal from where they originate, and hence can be utilised to identify its corresponding crystal orientation [87]. The angle and axis of misorientation of a certain GB can be calculated from the crystal orientations of the neighbouring grains forming the GB. EBSD measurements in this work were taken with a Zeiss UltraPlus analytical FESEM, equipped with an electron back-scatter pattern (EBSP) detector.

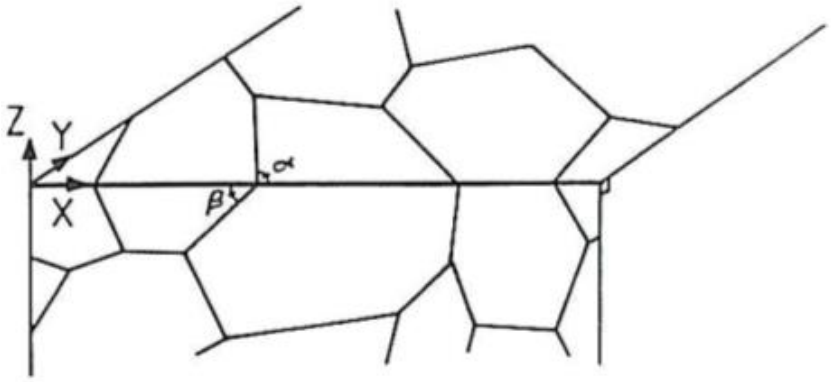


**Figure 2.13 – Schematic diagram showing two perpendicular surfaces of a sample for the determination of the position of the boundary plane. α and β denote angles that the GB makes with the x axis. (the figure is adapted from Ref. [56])**

Note that the typical EBSD setup only measures the axis and angle of misorientation of a GB. In order to obtain the actual position of the GB boundary plane, it is necessary to measure the inclination angle of the GB, in addition to the orientation of both grains. This can be done using the 'two-surface trace analysis', in which a GB trace is observed on two perpendicular and adjoining surfaces of the sample as illustrated in Figure 2.13. The position of the boundary plane, defined by its normal ($N_1$ *or* $N_2$), can be calculated from the measurement values of α and β. The details of the calculation are beyond the scope of this work and are shown in Randle [56]. This method requires both the top and the side views in the SEM, and so is not easily applied to a large number of GBs. It was not used in this thesis.

# Chapter 3
# Calibrating photoluminescence-based lifetime images on multicrystalline silicon wafers

## 3.1 Introduction

Carrier lifetime imaging is a major application for photoluminescence (PL) imaging. Not only has it allowed the carrier lifetime, which is one of the most critical parameters for characterising a solar cell, to be spatially determined, it can also be extended to other applications, such as imaging the interstitial iron concentration in p-type silicon through taking carrier lifetime images before and after dissociation of iron-boron pairs [49], or imaging the emitter saturation current density by applying the method of Kane and Swanson [88, 89] at each pixel in a lifetime image. Given that the PL intensity is usually measured only in relative units, a calibration procedure is required to convert the raw PL signal into carrier lifetime value.

Under steady state conditions and for a sample with a uniform carrier profile depth-wise, the measured relative PL intensity is given by:

$$\begin{aligned} I_{PL,rel,measured} &= A \times B_{rad} \times (p \times n) \\ &= C_{calibration} \times (N_{A/D} + \Delta n)\Delta n \end{aligned} \qquad (3.1)$$

With $A$ being a scaling factor, $B_{rad}$ being the radiative recombination coefficient, $n$ and $p$ being the electron and hole concentrations respectively, and $N_{A/D}$ and $\Delta n$ being the background doping and the excess carrier concentrations. $A$ and $B_{rad}$ can be combined into a single term named $C_{calibration}$, which represents the calibration factor.

Assuming negligible lateral carrier diffusion, as described in detail previously in Section 2.2.2.3, the effective lifetime can be related to the excess carrier concentration according to:

$$\tau_{eff} = \frac{\Delta n}{G} \qquad (3.2)$$

Equation 3.1 and 3.2 relate the arbitrary PL signal to the effective lifetime value. The relative PL signal has to be first converted into an absolute excess carrier concentration based on equation 3.1, from which the lifetime can then be calculated according to equation 3.2. This calibration procedure requires the determination of the calibration factor $C_{calibration}$ , and it is most commonly done by performing a separate carrier lifetime measurement on an area of the test sample using the Quasi-Steady-State Photoconductance (QSSPC) technique [64, 69] under the same illumination, and comparing the measured PL signal to the corresponding QSSPC data. This calibration procedure is typically performed at relatively high excitation levels in which the impact of trapping-like artefacts on the QSSPC data is usually negligible. This is based on the assumption that $C_{calibration}$ is injection level independent, an assumption which was shown to be valid only for injection levels up to $1 \times 10^{15}\ cm^{-3}$ at room temperature [90, 91]. Other effects may also impact on this assumption, in terms of the radiative recombination coefficient ($B_{rad}$).

In general, this standard calibration process is robust when the test sample is relatively homogeneous. It has the advantage that, since the calibration is performed on the test sample itself, there are usually negligible variations in doping, thickness, and optical properties of the calibration region compared to the rest of the test sample. However, as shown below, this approach is subject to significant uncertainty if the reference area chosen for the QSSPC measurement is highly inhomogeneous, as is often unavoidable for mc-Si samples in which large amounts of localised defects such as grain boundaries and dislocations exist. Moreover, the implicit extrapolation of the calibration factor to lower injection levels may also lead to quite large variations, as shown below.

Several studies have been performed on alternative techniques for self-consistent calibration of the PL signal, removing the reliance on the QSSPC data. Mitchell *et al.*

[92] demonstrated a method to extract the bulk lifetime of silicon bricks through the ratio of two luminescence images taken with different spectral filters. However, this method is limited to samples with strongly non-uniform carrier density profiles depth-wise, such as bricks, and is not applicable to high lifetime wafers. Giesecke *et al.* [70] converted PL images into lifetime images based on a lifetime measurement on a part of the test wafer through time modulated quasi-steady-state photoluminescence (QSSPL). Herlufsen *et al.* [93] and Kiliani *et al.* [94] extracted carrier lifetime images based on a time dependent photoluminescence signal, captured either using an InGaAs camera or a silicon CCD camera with its signal modulated by a rotating shutter wheel. The advantage of these dynamic PL calibration techniques is that they do not require any prior knowledge of the wafer parameters.

This chapter presents a more robust QSSPC based method for calibrating steady state PL images into carrier lifetime images. The chapter first describes conventional QSSPC calibration methods along with their strengths and limitations. Then, a new approach for calibrating PL images, based on an optically corrected calibration constant extracted from monocrystalline calibration wafers, is introduced. The principle and experimental verification of the method are first presented, followed by a comparison of the proposed approach against the conventional calibration method, demonstrated using a mc-Si wafer.

## 3.2 Experimental methods

A multicrystalline silicon wafer was used as a test wafer for demonstration. The mc-Si wafer used in this study was a p-type boron doped wafer, with a resistivity of $1.6\ \Omega \cdot cm$, from a commercially grown directionally solidified mc-Si ingot. The mc-Si wafer was passivated by silicon nitride and had a thickness of around 151 µm.

In addition, 22 monocrystalline silicon wafers, consisting of both Float-Zone and Czochralski silicon wafers, were used as calibration wafers for the proposed calibration method. A large number of wafers with different properties were chosen in order to test the reliability and robustness of the proposed calibration method, as shown below. 13 wafers were p-type boron doped with resistivity ranging from $0.47\ \Omega \cdot cm$ to $5.6\ \Omega \cdot cm$, while the remaining 9 wafers were n-type phosphorus doped with resistivity ranging

from $0.43\ \Omega \cdot cm$ to $2.5\ \Omega \cdot cm$. The thickness of the wafers varied from $167\ \mu m$ to $875\ \mu m$. The wafers were passivated either by aluminium oxide, silicon oxide or silicon nitride, and their effective lifetimes ranged from around $26\ \mu s$ to $2.6\ ms$, high enough to ensure uniform carrier profiles depth-wise in all cases. The reflectance of the wafers at 810 nm varied from around 0.17% to 31.2%, measured with a UV-Vis spectrophotometer (Perkin-Elmer Lambda 1050) with integrating sphere. Prior to passivation, all wafers were chemically polished either using $HNO_3$ acid and HF acid or TMAH solution, in order to yield specular surfaces.

PL images were captured with a BT Imaging LIS-R1 tool, with details described in Section 2.2.2. QSSPC lifetime measurements were performed using a Sinton Instruments WCT-120 lifetime tester integrated into the PL imaging system.

# 3.3 Conventional QSSPC based calibration method

## 3.3.1 Theory

In the conventional QSSPC calibration approach, the PL signal is calibrated against a QSSPC measurement on the test sample itself under the same illumination conditions. Here, we discuss two commonly used approaches for averaging the PL data in the region over the QSSPC sensor, as required in the conventional calibration approach for determining $C_{calibration}$.

The first approach determines $C_{calibration}$ through comparing a simple arithmetic average of the PL signal in a defined region above the QSSPC sensor, $I_{PL,Avg}$, with the corresponding excess carrier density data measured by the QSSPC technique, $\Delta n_{QSSPC}$.

$$C_{calibration} = \frac{I_{PL,Avg}}{(N_{A/D} + \Delta n_{QSSPC})\Delta n_{QSSPC}} \qquad (3.3)$$

Equation 3.3 is simple, easily implemented, and is accurate for homogeneous samples. However, it becomes less accurate when the sample has significant lateral non-uniformities. Firstly, the nonlinear relationship between the local values of $I_{PL,rel,measured}$ and $\Delta n$ at high injection, as indicated in equation 3.1, leads to errors in

the simple arithmetic averaging process. More importantly, in practice there are significant variations in the radial sensitivity of the radio frequency coil used in the QSSPC measurement [70, 94], leading to further inaccuracies in the averaging process. Figure 3.1 shows the radial sensitivity of a QSSPC sensor, measured by Giesecke [95] through dark conductivity analysis. It can be seen that the radial sensitivity of the sensor varies significantly, being most sensitive near the radio frequency coil.

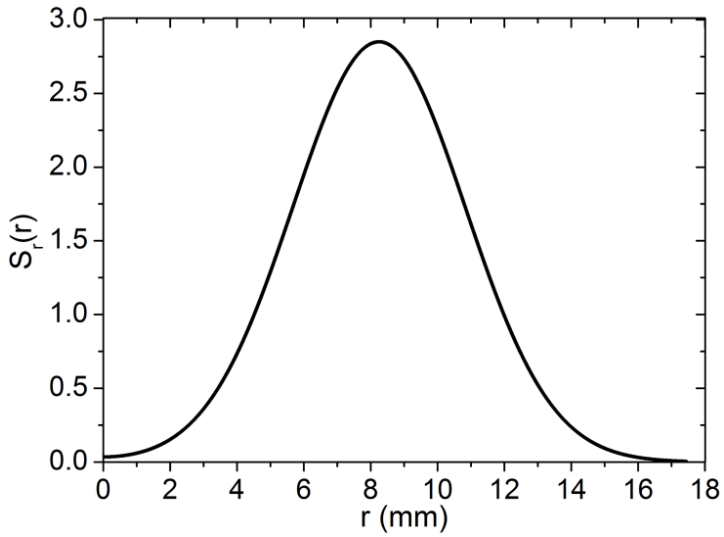


**Figure 3.1 - Radial sensitivity function of the QSSPC sensor, extracted from Giesecke [95]. $r$ represents the distance from the centre of the sensor. Following Giesecke [95], the sensitivity values are normalised according to $2\pi \int_0^R r dr \cdot S_R(r) = \pi R^2$, with $R$ chosen to represent the radius of the active sensing region of the sensor.**

Accounting for both of these problems, a more accurate calibration can be performed by correlating the local PL intensity measured at each pixel to the QSSPC measured excess carrier density data [70] according to the following equations:

$$\Delta n_i = \frac{-N_{A/D} + \sqrt{{N_{A/D}}^2 + 4\frac{I_{PL,i}}{C_{calibration}}}}{2} \quad (3.4)$$

$$\Delta n_{QSSPC} = \sum_i^N \frac{\Delta n_i \times S_r(r_i)}{N} \quad (3.5)$$

with $I_{PL,i}$ and $\Delta n_i$ being the local PL intensity and excess carrier density at each pixel respectively, $S_r$ being the radial sensitivity of the QSSPC sensor and $N$ being the total number of pixels in the sensed area of the QSSPC measurement. Equation 3.4 is derived

through solving equation 3.1 for $\Delta n$. Here, we did not measure the radial sensitivity of the QSSPC sensor used in this work, but applied a sensitivity function measured by Giesecke [95], as shown in Figure 3.1. This could lead to some errors as the sensitivity function of each QSSPC sensor may vary slightly. Despite this, the function is sufficient to demonstrate the errors induced by not accounting for the radial sensitivity of the sensor coil, which is the main objective of the work. $C_{calibration}$ can be determined through solving equation 3.4 and 3.5 by iteration. In this chapter, we will compare both averaging algorithms mentioned and discuss the possible causes of errors in the calibration process.

## 3.3.2 Application on a multicrystalline silicon wafer

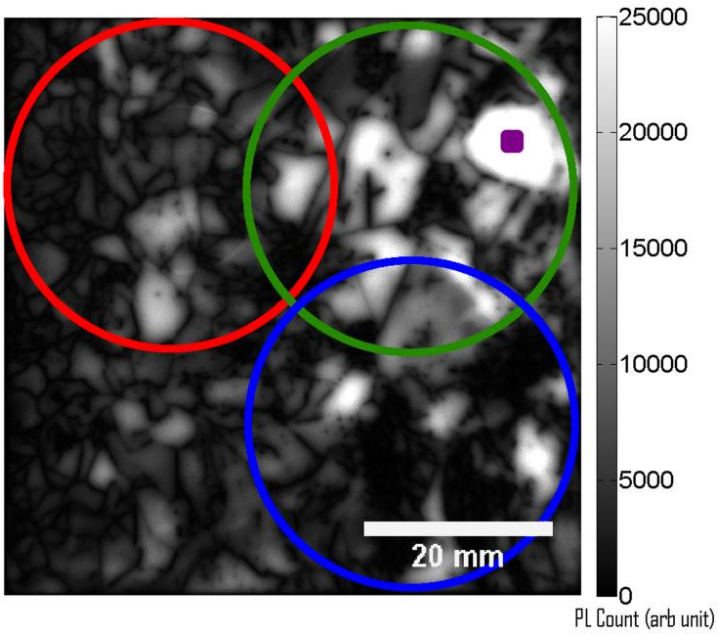


**Figure 3.2 - PL image of a mc-Si wafer. Red, green and blue circles represent three regions (R1, R2, and R3) that were used as the reference areas in the conventional QSSPC calibration methods. Purple square near the top right corner represents an intra-grain region used for lifetime analysis in Figure 3.5 and Figure 3.9.**

Figure 3.2 shows a PL image of the mc-Si wafer that was used as the test wafer. Individual PL and QSSPC measurements, at 15 different injection levels, were taken on the mc-Si test wafer by varying the illumination intensity. The QSSPC lifetimes of three different regions, as highlighted in Figure 3.2, combined with their corresponding PL intensity, were used to determine the calibration factor. Figure 3.3 shows the QSSPC

lifetime data for one of the highlighted regions (R2) in Figure 3.2. We observed high apparent lifetime values at low injection, due to minority carrier trapping. A trapping correction function [68] was applied to correct for the effect of trapping in the raw data and the result is shown in Figure 3.3.

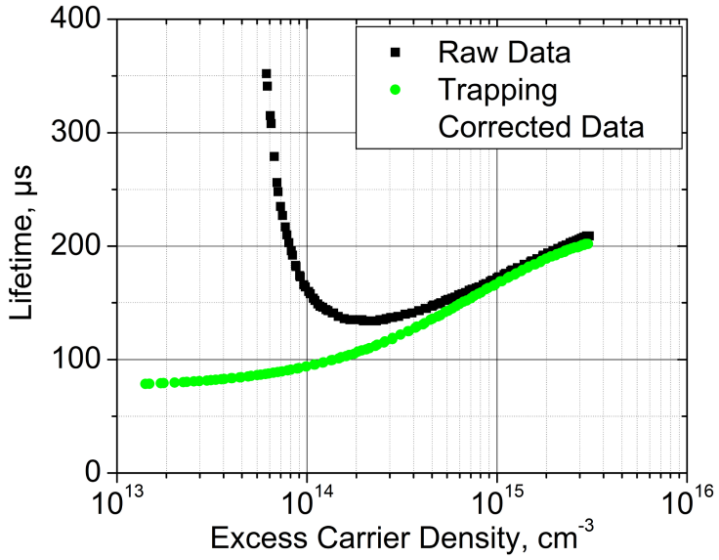


**Figure 3.3 – QSSPC lifetime data of R2, highlighted in Figure 3.2, before and after trapping correction. The trapping corrected data is used for the determination of the $C_{calibration\_CW}$ in Figure 3.4.**

Figure 3.4 compares the values of $C_{calibration}$ determined using the two different averaging algorithms mentioned above in Section 3.3.1, based on the trapping corrected QSSPC data. Note that the x-axis of Figure 3.4 shows the average excess carrier density of the whole wafer for each measurement, while the x-axis of Figure 3.3 shows the excess carrier density of one of the highlighted region (R2) in Figure 3.2. The first algorithm uses a simple arithmetic mean of the measured PL signal for calibration. It can be seen that $C_{calibration\_mc}$ determined by this simple averaging algorithm depends strongly on the choice of reference region used for calibration. The second algorithm correlates the QSSPC data with the measured PL signal at each pixel according to equation 3.4 and 3.5, including the influence of the variation in the radial sensitivity of the QSSPC sensor in the calculation. The $C_{calibration\_mc}$ values determined by this algorithm show only a small dependence on the choice of reference region which is likely to be due to uncertainty in the experimentally determined radial sensitivity data of the QSSPC sensor.

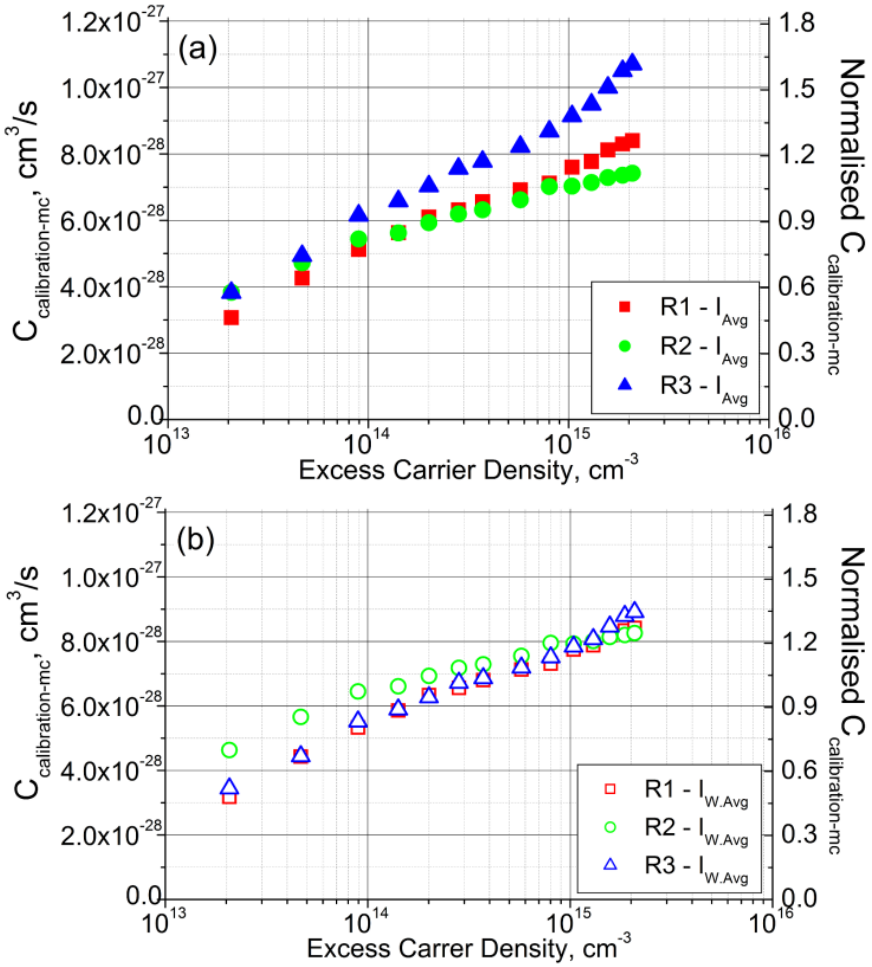


**Figure 3.4 – Variation of the calibration factor calculated based on the two different averaging algorithms, (a) using a simple arithmetic average ($I_{Avg}$) or (b) a position-dependent sensitivity-weighted average ($I_{W.Avg}$) of the measured PL signal, in the conventional calibration methods. The x-axis shows the average excess carrier density of the whole wafer for each measurement, calculated using the proposed calibration method shown below, for allowing a more consistent estimate for the excess carrier density. The secondary axis shows the values normalised against the mean value in the Figure.**

However, although the second algorithm produces more consistent results compared with the first one, the values of $C_{calibration\_mc}$ determined by both algorithms vary considerably with injection level. $C_{calibration}$, in principle, should be injection independent, at least up to $1 \times 10^{15}\ cm^{-3}$, and should be consistent regardless of the choice of reference area used for calibration, otherwise it could lead to a significant error in the calibrated lifetime values. This injection dependent variation in $C_{calibration}$ mainly originates from the QSSPC measurement, as discussed below. Since the

calibration relies on the QSSPC measurement, an overestimation of $\Delta n$ in the QSSPC data leads to an underestimation of the calibration factor and thus an overestimation of the calibrated lifetime values, and vice versa.

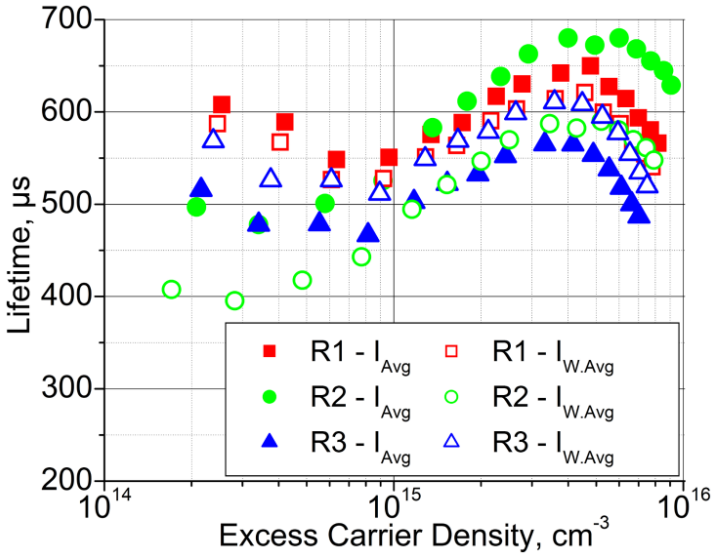


**Figure 3.5 - Injection dependent carrier lifetime of an intra-grain area, as highlighted in Figure 3.2, calibrated by two different averaging algorithms. R1, R2 and R3 represent three different reference areas used in the conventional calibration methods. Note that the x-axis shows the local excess carrier density of the highlighted intra-grain area.**

Figure 3.5 compares the injection dependent carrier lifetime of an intra-grain region, as highlighted as a purple square in Figure 3.2, calibrated with both averaging algorithms. The lifetime of an intra-grain region, far from grain boundaries and dislocations, was selected for comparison as the impact of lateral carrier smearing is minimal and the carrier profile is quite uniform depth-wise in such a region. The lifetimes calibrated by the second algorithm show only a slight variation in terms of their magnitude and injection dependence at high injection level compared to lifetimes calibrated using a simple arithmetic mean, in which substantial differences can be observed. This demonstrates the importance of accounting for the spatially non-uniform sensitivity of the QSSPC coil in measurements on samples with strong spatial variations in minority carrier lifetime.

However, at low injection level, the variation in the lifetime values becomes more significant in both methods and high apparent lifetime values can be observed. The high apparent lifetime values at low injection levels are likely due to minority carrier

trapping in the QSSPC lifetime measurement, although a trapping correction function [68] has already been applied to the QSSPC data. The trapping correction function implicitly assumes that the trapping centres are evenly distributed across the sample and are of a single type in terms of trapping characteristics such as the trap escape/release time ratio [3]. However, in an actual mc-Si sample, the trap density and type are very likely to vary significantly across a wafer. Therefore, the trapping correction may only allow a partial correction, and is not able to completely eliminate the impact of the traps, especially as the injection level is decreased below the apparent trap density.

Furthermore, the influence of trapping might not only be limited to measurements taken at low injection levels as it is possible that very low lifetime regions will have locally reduced excess carrier concentrations, at which trapping can still be prevalent, even when the average excess carrier density across the wafer is high. We observe a variation up to 2 orders of magnitude in the excess carrier density across the mc-Si wafer used in this work under a fixed generation rate.

## 3.4 Proposed calibration method

### 3.4.1 Theory

The conventional QSSPC based calibration method depends strongly on the accuracy of the QSSPC measurement. The method is robust on homogeneous samples, but is subject to significant uncertainty on highly inhomogeneous samples, due to the radial sensitivity of the QSSPC sensor, or on mc-Si wafers, due to measurement artefacts such as minority carrier trapping, as shown above. Therefore, we propose extracting an accurate calibration factor using a monocrystalline silicon wafer with homogeneous lifetime, and then converting it for application to the mc-Si test sample. Since the calibration sample and the test sample may have different doping, thickness and optical properties, and since $C_{calibration}$ depends on these properties of the sample, a correction has to be applied to $C_{calibration}$ to account for these variations. This correction can be performed based on modelling of the PL signal. In general, this can be achieved with simulation packages such as Quokka [96], which allows the PL emission from silicon

wafers to be accurately simulated. For the case of planar samples with uniform carrier profiles depth-wise, a simpler analytical approach can also be used, as outlined below.

Assuming a uniform carrier profile across the wafer thickness, the rate of spontaneous emission of electrons and holes via band-band transitions can be expressed by [97, 98],

$$\begin{aligned} r_{sp}(\hbar\omega) &= B_{rad}(\hbar\omega) \times (pn) \\ &= \alpha(\hbar\omega)\frac{{n_{Si}}^2 \times (\hbar\omega)^2}{\pi^2\hbar^3c^2}\exp\left(\frac{-\hbar\omega}{kT}\right)\left(\frac{1}{{n_i}^2}\right)(pn) \end{aligned} \quad (3.6)$$

where $\alpha$ is the absorption coefficient for band to band transitions [99], and $B_{rad}(\hbar\omega)$ is the spectral radiative recombination coefficient. $n_{Si}$, $\hbar\omega$, $\hbar$, $c$ denote the refractive index, photon energy, Reduced Planck's constant and velocity of light in vacuum respectively. Accounting for reabsorption and multiple reflections on both surfaces, the photon flux per energy interval emitted by a planar sample into a solid angle of detection Ω is described as [100],

$$\begin{aligned} &\frac{dj_{\gamma,em}}{d(\hbar\omega)}(\hbar\omega) \\ &= \frac{\Omega}{4\pi} \times \frac{1 - R_f(\hbar\omega)}{1 - R_f(\hbar\omega)R_b(\hbar\omega)\exp[-2\alpha(\hbar\omega)W]} \times r_{sp}(\hbar\omega) \\ &\quad \times \int_0^W \{\exp[-\alpha(\hbar\omega)x] + R_b(\hbar\omega)\exp[-\alpha(\hbar\omega)(2W - x)]\}\,dx \end{aligned} \quad (3.7)$$

with $R_f$ and $R_b$ being the spectral reflectivity of the front and of the rear surface, and $W$ being the thickness of the wafer. The influence of free carrier absorption [101, 102] is neglected in equation 3.7 due to its minor impact and weak wavelength dependence in the inspected wavelength range, coupled with the fact that the relative PL data is used.

The total measured relative PL intensity can be expressed as:

$$\begin{aligned} &I_{PL,rel,measured} \\ &= \kappa_{AD}\int_{hw_1}^{hw_2}\left(Q_{detector}(\hbar\omega) \times T_{filter}(\hbar\omega) \times \frac{dj_{\gamma,em}}{d(\hbar\omega)}(\hbar\omega)\right)d(\hbar\omega) \end{aligned} \quad (3.8)$$

with $Q_{detector}$ being the quantum efficiency of the silicon detector, $T_{filter}$ being the transmittance of the filters placed in front of the detector and $\kappa_{AD}$ being a conversion factor from photoelectrons to counts [103]. Substituting equation 3.6 and 3.7 into equation 3.8, the total measured PL intensity can be simplified to:

$$I_{PL,rel,measured} = K \times D \times (pn) \quad (3.9)$$

where

$$K = \kappa_{AD} \times \frac{\Omega}{4\pi} \quad (3.10)$$

and

$$\begin{aligned} & D\big(R_f(\hbar\omega), R_b(\hbar\omega), W\big) \\ & = \int_{\hbar\omega_1}^{\hbar\omega_2} \{Q_{dectector}(\hbar\omega) \times T_{filter}(\hbar\omega) \\ & \times \frac{1 - R_f(\hbar\omega)}{1 - R_f(\hbar\omega)R_b(\hbar\omega)\exp[-2\alpha(\hbar\omega)W]} \times \frac{{n_{Si}}^2 \times (\hbar\omega)^2}{\pi^2 h^3 c^2} \\ & \times \exp\left(\frac{-\hbar\omega}{kT}\right) \times \left(\frac{1}{{n_i}^2}\right) \\ & \times [1 - e^{-\alpha(\hbar\omega)W} + R_b(\hbar\omega)e^{-2\alpha(\hbar\omega)W}(e^{\alpha(\hbar\omega)W} - 1)]\} d(\hbar\omega) \end{aligned} \quad (3.11)$$

This function *D* is only dependent on the optical properties of a sample, and can be calculated according to equation 3.11 for a given sample if its thickness, front and rear reflectance are known, assuming that the quantum efficiency of the silicon detector and the transmission of the filters are also known. Here, it is assumed that the solid angle of detection, Ω in equation 3.7, is constant among different samples and the radiative recombination coefficient, $B(\hbar\omega)$ in equation 3.6, is injection independent for model simplification. For more sophisticated analysis, such influences [90, 91] should be considered.

Comparing equations 3.9 and 3.1, the calibration factor can be expressed as:

$$C_{calibration} = K \times D\left(R_f(\hbar\omega), R_b(\hbar\omega), W\right) \quad (3.12)$$

$C_{calibration}$ is the product of a constant scaling factor $K$ and the function $D$. Based on equation 3.12, the calibration factor between any two samples, the test mc-Si wafer and the calibration wafer (CW), are related via:

$$C_{calibration\_mc} = \frac{D(R_{f\_mc}(\hbar\omega), R_{b\_mc}(\hbar\omega), W_{mc})}{D(R_{f\_CW}(\hbar\omega), R_{b\_CW}(\hbar\omega), W_{CW})} \times C_{calibration\_CW} \quad (3.13)$$

In the proposed calibration method, we experimentally extract $C_{calibration\_CW}$ from a separate, homogeneous, monocrystalline calibration wafer, and calculate the value of $D\left(R_f(\hbar\omega), R_b(\hbar\omega), W\right)$ for both the calibration and test wafers. We then apply equation 3.13 to determine a suitable calibration factor, $C_{calibration\_mc}$, for the test sample to calibrate the PL signal into lifetime values. Since the calibration wafer has a uniform lifetime distribution, $C_{calibration\_CW}$ can be extracted accurately according to equation 3.3, using a simple arithmetic mean of the measured PL signal. Moreover, in such homogeneous wafers, the radial sensitivity of the QSSPC sensor does not impact the QSSPC measurement, hence eliminating a reliance on the experimentally determined radial sensitivity in the calibration.

In this work, a short pass filter with a cut off wavelength of 1025 nm is fitted in the imaging lens to filter the emitted band-to-band PL signal. In our experimental setup, samples were placed on a black sample stage where the spectral reflectivity between the wafers and the stage ($R_b$ in equation 3.11) is in general not known. The short pass filter served to minimize the proportion of rear reflected PL in the total measured PL, hence reducing the uncertainty in the optical modelling, both in terms of rear reflectance from the sample stage, and also in terms of any light-trapped photons resulting from imperfect sample polishing.

## 3.4.2 Experimental verification

A set of monocrystalline silicon wafers with different doping, thickness and reflectivity is used as calibration wafers to test the validity of the proposed optical correction

function (equation 3.13). For each wafer $C_{calibration\_CW}$ was determined multiple times for four different illumination intensities, equivalent to a range of injection levels, from a comparison of the average PL signal and the QSSPC measured average excess minority carrier concentration and the independently measured background doping. As can be observed from Figure 3.6(a), the values of $C_{calibration\_CW}$ extracted from the monocrystalline calibration wafers vary significantly, due to the differences in their optical properties.

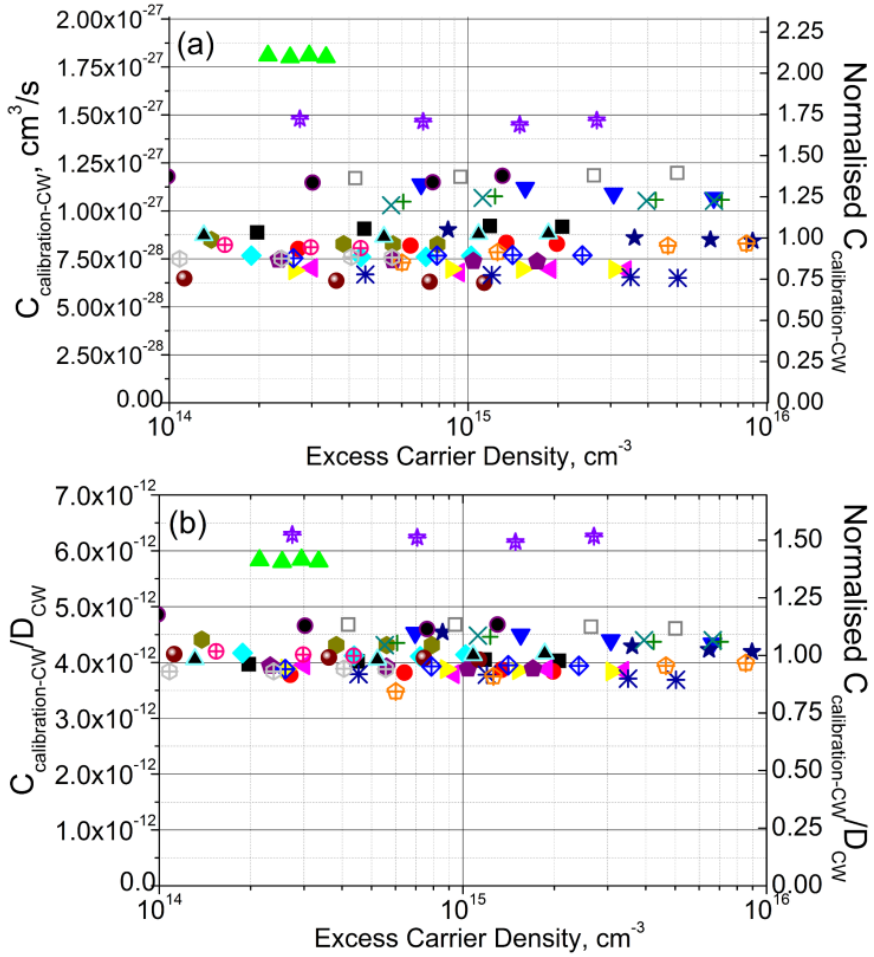


**Figure 3.6 – Injection dependence of (a) $C_{calibration\_CW}$ and (b) the ratio $C_{calibration\_CW}/D_{CW}$ extracted from a set of monocrystalline silicon wafers. $C_{calibration\_CW}/D_{CW}$ is dimensionless. Note that the samples with significantly higher ratios in Figure 3.6(b) are considerably thicker ($688\ \mu m$ and $875\ \mu m$), as shown in Figure 3.7, in which the same symbols are used to represent each sample. The secondary axis shows the values normalised against the mean value in each Figure.**

The value of the optical calibration constant $D_{CW}$ was then calculated for each wafer according to equation 3.11, using its measured optical properties. As shown in Figure

3.6(b), the ratios of $C_{calibration\_CW}/D_{CW}$ for the set of samples converge to an almost constant value, as expected, since the impact of the optical properties is divided out. Also note that for each calibration wafer, four values of the ratio $C_{calibration\_CW}/D_{CW}$ were extracted at different injection levels, revealing very little injection dependence. Therefore, despite the large variations in optical properties, most of the extracted ratios agree well with each other, with a small relative standard deviation of around 7%, indicating the validity of the proposed modelling.

Explicitly, we do not observe any dependence of $C_{calibration\_CW}/D_{CW}$ on injection level, minority carrier lifetime, doping, reflectance, and the types of surface passivation of the calibration wafers. However, $C_{calibration\_CW}/D_{CW}$ is observed to be slightly dependent on the wafer thickness as the thickness increases beyond 500 $\mu m$, as shown in Figure 3.7. This is likely to be due to the slight reduction in the sensitivity of the QSSPC measurement on thicker wafers. In general, for a precise calibration, it is advisable to choose a calibration wafer with similar properties to the test wafer in order to reduce the influences of any second order effects, such as free carrier or dopant induced band-gap narrowing [37, 104, 105], injection dependence of spontaneous radiative recombination [90, 91] or slight variation in solid angle of detection due to difference in sample thickness, which are not included in the proposed optical correction function.

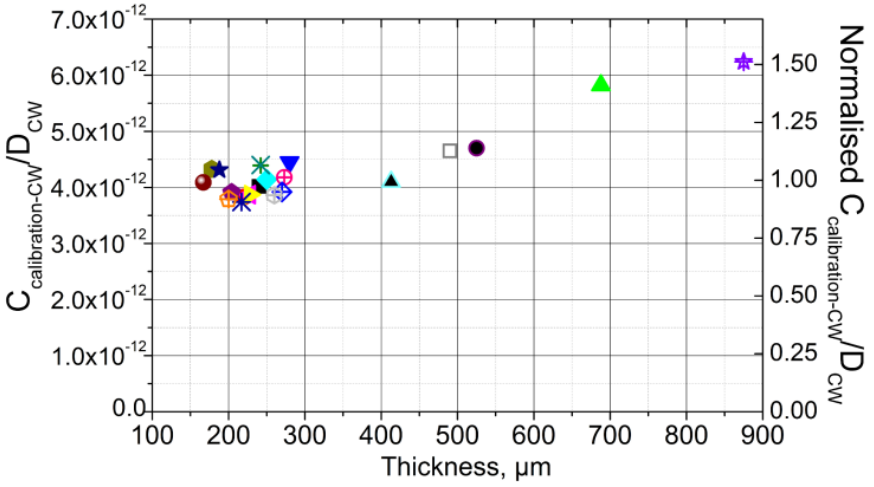


**Figure 3.7 - The influence of sample thickness on the ratio $C_{calibration\_CW}/D_{CW}$. The secondary axis shows the values normalised against the mean value in the Figure. The values in the figure represent the average ratios extracted from the four different injection levels in Figure 3.6(b).**

## 3.4.3 Application on a multicrystalline silicon wafer

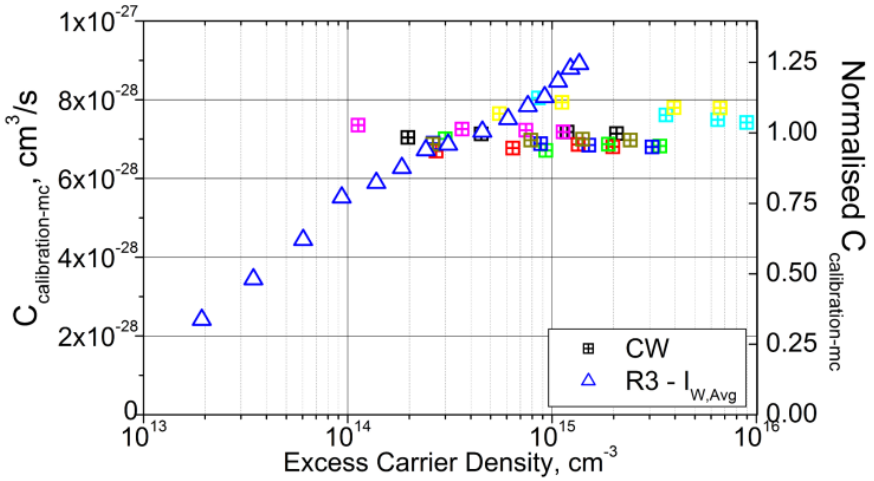


**Figure 3.8 - Variation of the calibration factor for the test mc-Si wafer ($C_{calibration\_mc}$) extracted from 8 separate monocrystalline calibration wafers (CW) at different injection levels and calculated according to equation 3.13. Also shown for comparison are values for $R3 - I_{W,Avg}$ which represent the calibration factors determined according to the standard calibration method, as shown in Figure 3.4(b). The secondary axis shows the values normalised against the mean value in the Figure. Note that the x-axis shows the average excess carrier density of the reference region, obtained from QSSPC measurements.**

We applied our proposed calibration method to the test mc-Si wafers. Based on equation 3.13, we determine $C_{calibration\_mc}$ for the test mc-Si wafer from $C_{calibration\_CW}$ extracted from several monocrystalline calibration wafers with different lifetimes, thickness, doping and reflectance. 8 calibration wafers, with their background doping ranging from $9 \times 10^{15}\ cm^{-3}$ to $1.27 \times 10^{16}\ cm^{-3}$ and their thickness varying from $167\ \mu m$ to $242\ \mu m$, were selected based on their similarity in thickness and background doping with the test mc-Si wafers. The variation in $C_{calibration\_mc}$ determined from our proposed approach, as shown in Figure 3.8, is significantly smaller than the variation in $C_{calibration\_mc}$ determined from the conventional calibration methods, shown in Figure 3.4, and it does not exhibit any injection level dependence. The average value of $C_{calibration\_mc}$ extracted from the selected calibration wafers is $7.16 \times 10^{-28}\ cm^3/s$, with a small relative standard deviation of around 4%.

At low injection, the calibration factors determined from the conventional approach are smaller than the calibration factors calculated from our proposed method. This is mainly

due to minority carrier trapping, which increasingly affects the QSSPC measurement used for calibration as the injection level decreases, even when a trapping correction procedure is applied [68]. This leads to an underestimation of the calibration factor.

At high injection levels, in which the lifetime is unaffected by trapping, the opposite is observed. This may be partially due to an overestimation of the carrier mobility sum in mc-Si wafers in regions with high dislocation densities. It has been reported previously that the carrier mobility in some regions of mc-Si wafers is lower when compared with the carrier mobility in monocrystalline wafers [106, 107], due to the presence of grain boundaries or dislocations which act as barriers for carrier diffusion. An overestimation of the mobility sum will result in an underestimation of the QSSPC measured lifetime, and an overestimation of the calibration factors. In addition, the errors could also be caused by, or partly caused by, the presence of low lifetime areas, in which the excess carrier density is not uniform depth-wise. This causes the excess carrier density to be underestimated in the QSSPC measurement [108], also leading to an overestimation in the calibration factor [109].

Comparing both calibration methods, it can be seen that the standard calibration method is subject to errors at both low and high injection and is accurate only when the calibration is performed within a narrow range of injection levels, in this case, for $\Delta n \approx 2 \times 10^{14} - 1 \times 10^{15}\ cm^{-3}$. The common approach of applying a single calibration factor obtained on a mc-Si wafer at higher injection to other injection levels, in order to avoid trapping-like measurement artefacts, is therefore prone to significant uncertainty. In some cases it may be quite accurate, while in others it can produce significant errors.

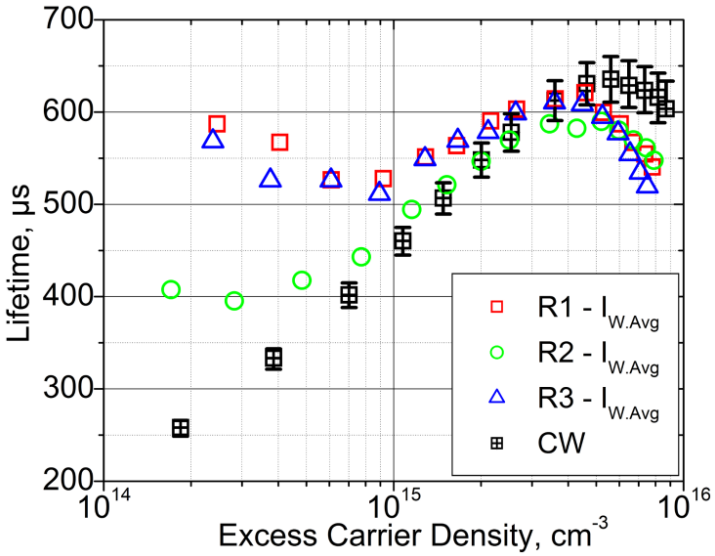


**Figure 3.9 – Injection dependent carrier lifetime of an intra-grain area, as highlighted in Figure 3.2, calibrated by our proposed approach. R1, R2 and R3 represent the lifetimes calibrated using three different reference areas in the conventional QSSPC calibration method. CW represents the lifetimes calibrated by separate Calibration Wafers (CW). The error bars represent one standard deviation in the extracted values of $C_{calibration\_mc}$ in Figure 3.8. Note that the x-axis shows the local excess carrier density of the highlighted intra-grain area.**

Figure 3.9 shows the injection dependent lifetime of the same intra-grain region highlighted in Figure 3.2 calibrated by our proposed method. As reference, we plotted the most accurate calibrated lifetime values achievable by the conventional approach, calibrated according to equations 3.4 and 3.5 with the QSSPC sensitivity function implemented. A considerable difference in the calibrated lifetime values, in terms of the magnitude and injection dependence, can be observed. The differences in the lifetime values calibrated by our method and the conventional approach vary from up to 70% at low injection levels ($\Delta n \approx 4 \times 10^{14}\ cm^{-3}$) to around 14% at moderate injection levels ($\Delta n \approx 7 \times 10^{15}\ cm^{-3}$). When using our proposed method, we do not observe any artificially high lifetime values at low injection due to minority carrier trapping. In our proposed calibration method, the calibration factor is extracted from monocrystalline wafers with homogeneous lifetime. The effect of trapping is minimised in such wafers due to low impurity levels and the lack of localised defects. As such there is no requirement to fit a trapping correction to the QSSPC data, making the calibration procedure more robust.

## 3.5 Discussion

While PL measurements are not subject to measurement artifacts such as minority carrier trapping, it is crucial that the reference data used for the calibration of the PL signal is also unaffected by such artifacts; otherwise, it could lead to a significant error. Our calibration method thus allows more consistent and accurate PL-based lifetime images at various injection levels, especially at low injection levels, compared with the standard calibration method. This is particularly relevant for some applications on mc-Si wafers, for example, when evaluating small variations of lifetime among different grains or after processing sister wafers under different conditions. Examples of such applications are shown in Chapters 5-7.

The method could also be applied to increase the accuracy in imaging interstitial iron concentrations, in which two PL images are taken at two different injection levels, before and after dissociation of iron-boron pairs [49], and the measurements are often performed at low or moderate injection levels ($\Delta n \ll 1 \times 10^{14}\ cm^{-3}$) to avoid breaking of iron-boron pairs during the initial measurement. It can also be used to measure lifetimes on small samples which cannot be measured accurately using the conventional QSSPC measurement setup as the sample is significantly smaller than the QSSPC sensor. One such application is shown in Section 7.3.2, in which the carrier lifetimes of small and narrow silicon strips are determined through PL imaging using the proposed calibration method. Furthermore, since $C_{calibration\_CW}/D_{CW}$ depends only on the system setup and is independent of the test sample parameters, it only needs to be determined once and can be applied to measurements on different samples at different injection levels, provided that the exposure time of the PL images is accounted for.

It should be noted that in our proposed calibration method, the PL signal is calibrated into lifetime values based on a few key assumptions. Firstly, it is assumed that the carrier density profile is uniform depth-wise, in both the calibration wafers and the test wafers. While the former can be easily achieved by selecting calibration wafers with high lifetime, the latter might not be achievable especially at low lifetime regions such as grain boundaries. Photon reabsorption within the sample can impact the fraction of internally generated photons that can escape the sample and contribute to the detected

signal. Our analysis accounts for photon reabsorption based on the assumption that the carrier density is uniform. A non-uniform profile affects the total amount of photon reabsorption, and hence can lead to errors in calibrating the PL signal. Variations in that fraction have been shown to be generally small, and are significant only if the minority carrier lifetime varies strongly with injection level over the range from $1\ \mu s$ to $\sim 50\ \mu s$ [110]. Therefore, our analysis can be assumed to be reasonably accurate for most situations except when applying to low lifetime areas or samples. In such cases, more sophisticated modelling tools such as Quokka [96] or QS Cell [85] are required to account for the impact of non-uniform carrier profiles on photon reabsorption.

Secondly, our method also requires both the calibration wafers and the test wafers to have planar surfaces without any texturing. This is due to the assumption of a planar surface in the derivation of equations 3.7 and 3.11. Texturing induces an increase in the average path length of luminescence within the sample [83], which can strongly affect the fraction of internally generated photons contributing to the measured PL signal. Short pass filtering can restrict the detected luminescence signal to wavelengths which are not strongly affected by these path length enhancement effects. By choosing calibration wafers with similar texture, combined with more sophisticated optical modelling, our proposed method might be applicable also to textured wafers.

Lastly, our method of modelling the emitted photoluminescence is based on the assumption that the radiative recombination coefficient is injection independent. It has been reported that the radiative recombination coefficient is enhanced by coulomb attraction between electrons and holes, and that enhancement is reduced at high carrier density due to carrier screening, especially when $\Delta n \gg 5 \times 10^{15}\ cm^{-3}$ [91]. Hence, our calibration method is best applied at lower injection levels or when both the calibration wafers and the test wafers are at similar injection levels. An empirical expression has been proposed by Altermatt *et al.* [90] to account for influence of Coulomb-enhancement on $B_{rad}$. However, the expression only applies on the integral radiative recombination coefficient over the entire spectrum but not on each particular wavelength, hence cannot be directly incorporated into our method due to the spectral dependent components used in the modelling such as the quantum efficiency of the detector and the transmission of the filters. The accuracy of our proposed calibration

method, especially when applying at high injection levels, can be further improved by implementing the influence of Coulomb-enhancement in the modelling.

## 3.6 Conclusions

In this chapter, a method for the accurate conversion of PL images into calibrated lifetime images for wafers with inhomogeneous lifetime distributions is presented. The method is based on an optically-corrected calibration factor extracted from PL and QSSPC measurements on a separate calibration wafer with homogeneous lifetime. The magnitude and injection dependence of the lifetime calibrated by the conventional approach depends on the choice of reference region used for calibration in a mc-Si wafer, and at lower injection levels on the accuracy of the trapping correction. Comparison of two conventional calibration approaches showed that radial variations in the sensitivity of the coil area in commonly used QSSPC lifetime measurement systems should be accounted for to avoid significant errors. In contrast, the lifetimes calibrated by our proposed method are consistent, regardless of the choice of calibration wafer. The proposed method also eliminates the requirement for trapping corrections and the need for measuring radial sensitivity functions for the analysis of the QSSPC data. The proposed method is used throughout this thesis for calibrating PL images.

# Chapter 4
# Quantifying carrier recombination at grain boundaries in multicrystalline silicon wafers through photoluminescence imaging

## 4.1 Introduction

Grain Boundaries (GBs) are one type of crystal defect which can significantly affect the efficiency of mc-Si solar cells. They can act as strong recombination centres for excess carriers, and hence can locally reduce the minority carrier lifetime and impact the solar cell performance. Understanding the electrical properties of GBs is therefore of great interest. GBs have been studied extensively in the literature [5, 20, 23, 24, 31], either by electron beam induced current (EBIC), light beam induced current (LBIC), photoluminescence (PL) imaging, electroluminescence (EL) imaging and other lifetime imaging or mapping techniques. In order to compare or evaluate GBs, the recombination behaviour of GBs needs to be quantified.

The most commonly used method for evaluating GBs is the signal contrast method [5], which is defined as the ratio of the signal intensity between the GB and the intra-grain region. For the case of PL measurements, the PL contrast of a GB is defined as,

$$PL_{contrast} = \frac{PL_{intra-grain} - PL_{GB}}{PL_{intra-grain}} \qquad (4.1)$$

Where $PL_{intra-grain}$ and $PL_{GB}$ represent the intra-grain PL intensity and the PL intensity at the GB respectively. For other measurement techniques, $PL_{intra-grain}$ and $PL_{GB}$ are replaced with the corresponding measured signal intensity. Signal contrast is

straightforward and easy to calculate, thus allowing a large number of GBs to be studied. However, it only provides evaluation of the recombination strength on a relative scale, and depends heavily on the lifetime of the intra-grain region, which is likely to vary at different injection levels, among different wafers, or during cell processing steps such as phosphorus gettering and hydrogenation. As signal contrast is only a relative and qualitative representation, it also prohibits a direct comparison of results from various works.

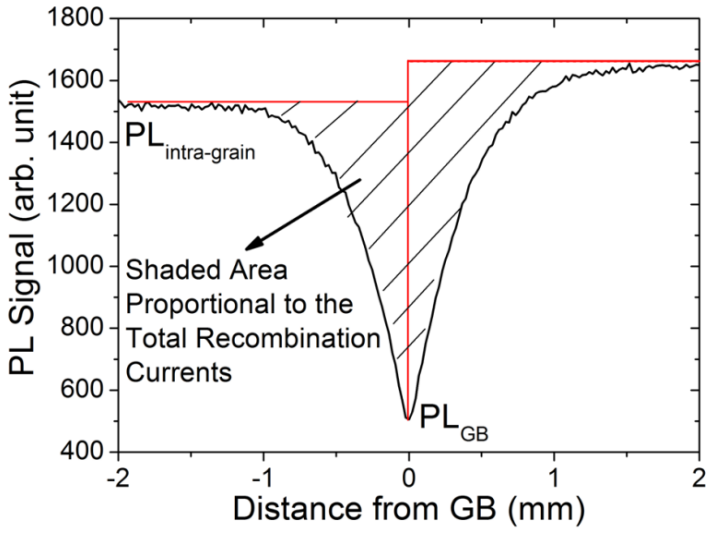


**Figure 4.1 - PL intensity profile across a GB.**

An alternative method to quantify the recombination properties of a GB is to calculate the recombination current induced by the GB, based on the PL intensity profile across the GB. The method is adapted from an approach proposed by Augarten *et al.* [111] for calculating shunt currents. Due to the higher recombination at the GB, carriers generated around the GB diffuse toward the GB, leading to a gradual reduction of PL intensity, as illustrated in Figure 4.1. The recombination current per unit length induced by the GB can be calculated as,

$$I_{R_{GB}}/_{L} = \sum_{i} J_L \times W \times \left(1 - \frac{PL_i}{PL_{intra-grain}}\right) \qquad (4.2)$$

Where $J_L$ and W represent the light generated current density and the sample width of one camera pixel in the PL image respectively. $PL_i$ represents the PL intensity of each individual pixel which is affected by the GB. Equation 4.2 can be divided into two parts.

$J_L \times W$ represents the light generated current density which is only dependent on the excitation source and the optical properties of the samples. $(1 - PL_i/PL_{intra-grain})$ represents the proportion of the total light generated current which recombines at the GB. $I_{R_{GB}}/L$ reflects the effective detrimental influence of a GB in a mc-Si wafer when it is illuminated, similar to a solar cell under normal operation. It also allows the recombination strength of a GB to be expressed in an absolute scale, for example with units of $mA/cm$. Nevertheless, such a parameter might be misleading in representing the electrical properties of a GB as it depends not only on the GB itself, but also strongly on other parameters such as the carrier generation rate and the lifetime of the grains near the GB. In order to clarify the root cause of the varying recombination behaviour of GBs, it is more meaningful to evaluate the intrinsic recombination properties of GBs, which are independent of the measurement conditions or other sample parameters.

Donolato [112, 113] presented an analytical model to describe the recombination properties of GBs and dislocations in terms of interface recombination velocity and line recombination velocity. The works were further extended by Riepe *et al.* [114] and Stokkan *et al.* [115], who modelled the effect of various GBs and dislocations on minority carrier lifetime for Carrier Density Imaging (CDI) measurements, in terms of parameters such as grain boundary misorientation and capture cross section. Corkish *et al.* [116] and Micard *et al.* [117] proposed a direct fitting procedure based on analytical modelling to extract the effective surface recombination velocities ($S_{GB}$) of GBs and the diffusion length in the neighbouring grains from EBIC and LBIC profiles across a GB.

In this chapter, an approach, based on steady state PL imaging and 2D modelling of the emitted PL signal, to quantify the recombination strength of GBs in terms of the effective surface recombination velocity ($S_{GB}$) is presented. This provides a more meaningful and absolute measure of the recombination properties of a GB compared to signal contrast or recombination current mentioned above. Moreover, a major advantage of the PL imaging technique is that it does not require a cell structure or a pn junction, in contrast to EBIC or LBIC measurements, thus reducing the difficulty of sample preparation as well as the complexity of the modelling. Also, owing to the rapidity of PL imaging, the method can be applied to a larger number of GBs for a statistically

relevant analysis. The chapter starts with a description of the principle of the method. The approach is then demonstrated on two different types of samples. Firstly, the method is applied to determine $S_{GB}$ of several GBs in double-side passivated mc-Si wafers, both before and after phosphorus gettering. Secondly, the method is applied to mc-Si wafers with infinite surface recombination at the rear surfaces, in order to enhance the sensitivity of the method to strongly recombination active GBs, as explained in detail below. The sensitivity limits and other practical constraints of the method are discussed in the end of the chapter.

# 4.2 Model Description

## 4.2.1 Model description and assumptions

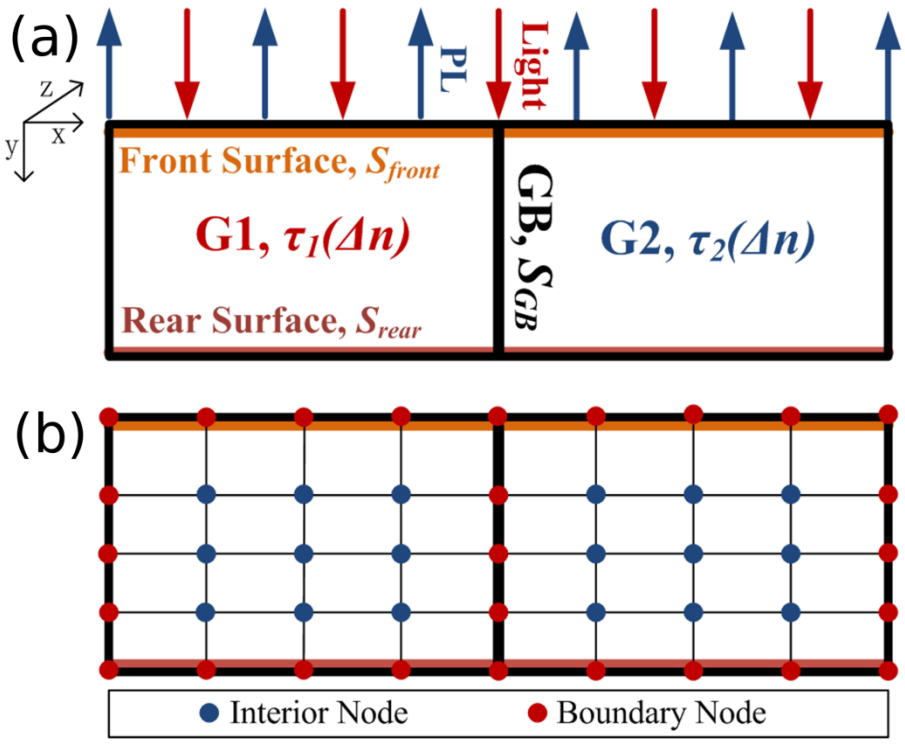


**Figure 4.2 - (a) Schematic of the presented 2D model. (b) Grid structure of the semiconductor for finite element analysis.**

Our presented model is a two dimensional simplification of a three dimensional problem, assuming no variation in the materials along the z-axis. Figure 4.2(a) shows the schematic of our 2D model, illustrating the interactions between a GB and its neighbouring grains under steady state illumination. A GB, modelled as a surface with

an effective surface recombination velocity ($S_{eff}$), is located between two neighbouring grains, G1 and G2 with bulk minority carrier lifetime $\tau_1(\Delta n)$ and $\tau_2(\Delta n)$, respectively. The semiconductor is subjected to a certain degree of surface recombination at both the front and rear surfaces, depending on the films on the surfaces, represented by $S_{front}$ and $S_{rear}$. Both $S_{front}$ and $S_{rear}$ are considered to be injection independent in the model, as the surface recombination velocities are assumed to be either negligible or infinite, as explained further below. Here, it is assumed that the GB is perpendicular to the surfaces. A GB, in reality, is not necessarily perfectly perpendicular to the surfaces, however, within a thin wafer, it lies close to perpendicular.

The semiconductor is divided into multiple nodes in both $x$ and $y$ directions, as shown in Figure 4.2(b). The local carrier concentration at each node is simulated using a finite difference method based on the continuity equation, allowing for local carrier generation, diffusion and recombination. We then modelled the PL profile across a GB through the rate of spontaneous emission of electrons and holes via band-band transitions, considering reflection, reabsorption of the emitted PL and the quantum efficiency of the detector. A summary of the equations used is given in the succeeding sections.

## 4.2.2 Bulk equations

In 2D and under steady state conditions ($dn_{x,y}/dt = 0$), the continuity equation can be written as:

$$\frac{dn_{x,y}}{dt} = D_{eff}\left(n_{x,y}\right) \times \nabla^2 n_{x,y} + G_{x,y} - \frac{n_{x,y} - n_o}{\tau_{x,y}\left(n_{x,y}\right)} = 0 \qquad (4.3)$$

Where $x, y$ denotes the position of the node, $n_{x,y}$ is the local carrier concentration, $G_{x,y}$ is the local generation rate per unit volume, $\tau_{x,y}$ is the local bulk lifetime, $n_o$ is thermal equilibrium electron concentration, and $D_{eff}$ is the effective carrier diffusivity [85]. $(n_{x,y} - n_o)/\tau_{x,y}(n_{x,y})$ represents the bulk recombination rate. $D_{eff}(n_{x,y}) \times \nabla^2 n_{x,y}$ represents the rate of change of electron current flowing into the node. The electron current, in general, consists of a diffusion term and a drift term, both can be lumped

together with the use of $D_{eff}$ [85]. In this work, we adapt the carrier mobility model from Klaassen [65, 66] to calculate the effective carrier diffusivity, according to:

$$D_{eff} = \frac{(n+p)D_n D_p}{nD_n + pD_p} \quad (4.4)$$

Where $D_n$ and $D_p$ are the diffusion coefficients for electrons and holes.

### 4.2.3 Boundary conditions

Surface recombination acts as another recombination source in the nodes located at the surfaces or at the GB. The continuity equation is modified accordingly to represent those nodes. For a node located at the front surface, equation 4.3 is modified as,

$$\frac{dn_{x,y}}{dt} = D_{eff}(n_{x,y}) \times \nabla^2 n_{x,y} + G_{x,y} - \frac{n_{x,y} - n_o}{\tau_{x,y}(n_{x,y})} - \frac{S_{front}(n_{x,y} - n_o)}{\Delta y/2} \quad (4.5)$$

Where $S_{front}$ is the effective surface recombination velocity of the front surface. $S_{front}(n_{x,y} - n_o)/(\Delta y/2)$ represents the recombination rate per unit volume of the node induced by surface recombination at the front surface. Equivalently, the boundary condition for a node located at the GB can be express as,

$$\frac{dn_{x,y}}{dt} = D_{eff}(n_{x,y}) \times \nabla^2 n_{x,y} + G_{x,y} - \frac{n_{x,y} - n_o}{\tau_{x,y}(n_{x,y})} - \frac{S_{GB}(n_{x,y} - n_o)}{\Delta x} \quad (4.6)$$

Where $S_{GB}$ is the effective surface recombination velocity of the GB. $S_{GB}(n_{x,y} - n_o)/\Delta x$ represents the recombination rate per unit volume of the node induced by recombination at the GB. The difference between the volume of the nodes at the front surface and at the GB leads to the factor of 2 difference in the surface recombination terms in equation 4.5 and equation 4.6. Here, it is assumed that any space charge regions near the GBs [118] are small in extent in comparison to the minority carrier diffusion lengths, allowing us to avoid modelling the impact of drift currents in the space charge regions near GBs.

### 4.2.3.1 Boundary conditions for diffused samples

While the proposed model is mainly applied on non-diffused samples in this work, it is also possible to simulate diffused samples. The influence of the heavily doped region can be modelled using the conductive boundary approach [119]. For diffused samples, equation 4.5 is modified as:

$$\frac{dn_{x,y}}{dt} = qD_{eff}(n_{x,y}) \times \nabla^2 n_{x,y} + \nabla_t \left(\frac{1}{R_{sheet}} \nabla_t \varphi_{Fn}\right) + qG_{x,y} - q\frac{n_{x,y} - n_o}{\tau_{x,y}(n_{x,y})} - J_{0f}\left(\frac{p_{x,y} n_{x,y}}{{n_i}^2} - 1\right)\left(\frac{2}{\Delta x \Delta y}\right) \quad (4.7)$$

Where $\varphi_{Fn}$ is the electron quasi-fermi potential, $\nabla_t$ is the divergence tangential to the surface, $R_{sheet}$ is the sheet resistance, $J_{0f}$ is the emitter saturation current density for the front surface. $\nabla_t \left(\frac{1}{R_{sheet}} \nabla_t \varphi_{Fn}\right)$ represents the additional lateral current flow through the heavily doped regions. It can be expressed in terms of $n_{x,y}$ as follows:

$$\nabla_t \left(\frac{1}{R_{sheet}} \nabla_t \varphi_{Fn}\right) = \left[\frac{1}{n_{x,y}} - \left(\frac{\mu_n - \mu_p}{n\mu_n + p\mu_p}\right)\right]\left(\frac{kT}{q}\right)\left(\frac{1}{R_{sheet}}\right) \times {\nabla_t}^2 n_{x,y} \quad (4.8)$$

Where $\mu_n$ and $\mu_p$ denote the electron and hole carrier mobility. Unlike equation 4.3 - 4.6, equation 4.8 decouples the total electron current into two components, a diffusion component driven by the electron concentration gradient, and a drift component driven by an electric field created by the mobility difference between elections and holes.

Note that non-diffused samples are used for $S_{GB}$ extraction. The modelling work presented here in this section is not used for $S_{GB}$ extraction, but to simulate and compare the detrimental influence of a GB in samples with or without diffusions. The results are shown in Section 5.3.7.

## 4.2.4 Generation

The local generation rate per unit volume is a function of the depth (y-coordinate) of each node and is calculated according to

$$G_{x,y}(y) = \alpha \times (1 - R_f) \times \phi \times \exp(-\alpha y) \quad (4.9)$$

Where $\alpha$ is the absorption coefficient for band to band transitions [99], $R_f$ is the reflectivity of the front surface at the laser wavelength and $\phi$ is the photon flux at the surface of the sample.

## 4.2.5 Implementation

The carrier concentration of each individual node is correlated to the carrier concentration of its adjacent nodes through the $\nabla^2 n_{x,y}$ term in equation 4.3, 4.5, 4.6 and the boundary conditions ($S_{front}, S_{rear}, S_{GB}$), thus forming a system of equations. The carrier concentration in each node can be determined by solving this system of equations if each local $D_{eff}$, $\tau_{x,y}$ and $G_{x,y}$ are all known. The local generation rate is calculated according to equation 4.9, or otherwise can be obtained from other modelling tools such as OPAL [120]. The effective carrier diffusivity in each element is calculated through equation 4.4. Note that the effective carrier diffusivity and the bulk lifetime are both injection dependent. This requires an initial guess of the carrier concentration and solving the system of equations through iteration until each local carrier concentration converges. The model is implemented in Matlab. The average computation time is on the order of seconds, depending on the grid size. Of course, it is also possible to use other 2D/3D simulation packages such as Sentaurus [121] to simulate the cases described in this work.

## 4.2.6 Modelling of the PL signal

Once the local carrier concentration of each individual node is known, the detected PL signal can be modelled. The rate of spontaneous emission of electrons and holes via band-band transitions can be expressed by [97, 98],

$$r_{sp}(x,y,\hbar\omega) = \alpha(\hbar\omega)\frac{{n_{Si}}^2 \times (\hbar\omega)^2}{\pi^2\hbar^3c^2}\exp\left(\frac{-\hbar\omega}{kT}\right)\left(\frac{1}{{n_i}^2}\right)(p_{x,y}n_{x,y}) \qquad (4.10)$$

Where $n_{Si}$, $\hbar\omega$, $\hbar$, $c$ denote the refractive index, photon energy, reduced Planck's constant and velocity of light in vacuum respectively. Accounting for reabsorption and multiple reflections on both surfaces and assuming planar surfaces, the photon flux per energy interval emitted by each individual node into a solid angle of detection Ω is described as [100],

$$\begin{aligned}&\frac{dj_{\gamma,em}}{d(\hbar\omega)}(x,y,\hbar\omega)\\ &= \frac{\Omega}{4\pi}\times\frac{1-R_f(\hbar\omega)}{1-R_f(\hbar\omega)R_b(\hbar\omega)\exp[-2\alpha(\hbar\omega)W]}\times r_{sp}(x,y,\hbar\omega)\\ &\times\{\exp[-\alpha(\hbar\omega)y]+R_b(\hbar\omega)\exp[-\alpha(\hbar\omega)(2W-y)]\}\Delta x\Delta y\Delta z\end{aligned} \qquad (4.11)$$

with $R_f(\hbar\omega)$ and $R_b(\hbar\omega)$ being the spectral reflectivity of the front and of the rear surface, $W$ being the thickness of the wafer, and $\Delta x\Delta y\Delta z$ represents the volume of the node. The influence of free carrier absorption [101, 102] is neglected in equation 4.11 due to its minor impact and weak wavelength dependence in the inspected wavelength range, coupled with the fact that we use relative PL data. Here, it is assumed that only the photon flux emitted vertically from each node can reach the detector due to the narrow escape cone at the silicon-air interface and the large object distance from the imaging lens which limits the solid angle of detection to within the column dimensions [96]. This assumption can only hold for samples with planar surfaces [122]. The solid angle of detection is assumed to be constant across the sample surface, thus does not impact the relative PL signal. Based on the assumptions above, the PL signal at each pixel in a PL image is modelled by integrating the photon flux emitted vertically from nodes in the same column. The measured relative PL intensity at a given coordinate $x$ can be expressed as:

$$I(x)_{PL,measured} = K \times I(x)_{PL,simulated} \qquad (4.12)$$

Where

$$I(x)_{PL,simulated} = \int_{hw_1}^{hw_2} (Q_{detector}(\hbar\omega) T_{filter}(\hbar\omega) \sum_{y=0}^{y=W} \frac{dj_{\gamma,em}}{d(\hbar\omega)}(x, y, \hbar\omega)) d(\hbar\omega) \quad (4.13)$$

with $Q_{detector}$ being the quantum efficiency of the silicon detector, $T_{filter}$ being the transmittance of the filters placed in front of the detector and $K$ being a scaling factor. The scaling factor $K$ can be determined by comparing the measured PL signal of a spatially uniform region with the simulated PL signal, calculated according to equation 4.13. This scaling factor, in principle, is a constant and is homogeneous among different samples. However, due to the fact that the scaling factor is calculated based on various experimentally determined parameters such as the reflectivity and the bulk lifetimes which are subject to a certain level of uncertainty, we applied an individual value of $K$ for each sample determined by choosing a spatially uniform region in that particular sample for improving the accuracy of the modelling of the detected PL signal. The average value of the scaling factor $K$ extracted from both single-side and double-side passivated samples presented in this chapter is $2.8 \times 10^{-7}$, with a relative standard deviation of 7%.

Based on equation 4.12, the detected PL signal at each position $x$ can be calculated if the carrier density inside the semiconductor is known, thus allowing modelling of the PL profile across a GB.

### 4.2.7 Extraction of $S_{GB}$ of a GB

The simulated PL profile across a GB is a function of the incident photon flux, the reflectivity, thickness and doping of the sample, the surface recombination velocity of the GB, the lifetimes of the neighbouring grains forming the GB and other instrument dependent parameters such as the quantum efficiency of the detector. All the parameters except $S_{GB}$ can be measured directly. The injection dependent bulk lifetimes of the neighbouring grains are sample parameters required for the model and are extracted from PL calibrated lifetime images, as explained further below. Based on the model, $S_{GB}$ of a GB is determined by fitting the simulated PL profile to an experimental profile

extracted from a PL image, using the golden section search [123] with $S_{GB}$ as the only varying parameter. A list of parameters required for the fitting is outlined in Table 4.1.

**Table 4.1 - A list of parameters required for the fitting.**

| **Sample parameters** | |
|---|---|
| Spectral reflectivity of the front and rear surfaces | $R_f(\hbar\omega), R_b(\hbar\omega)$ |
| Thickness | $W$ |
| Doping | $N_{A/D}$ |
| Lifetimes of the neighbouring grains | $\tau_1(\Delta n), \tau_2(\Delta n)$ |
| **Measurement dependent parameters** | |
| Incident photon flux | $\phi$ |
| Transmission of the optical filter | $T_{filter}(\hbar\omega)$ |
| Quantum efficiency of the detector | $Q_{detector}(\hbar\omega)$ |

For samples with uniform carrier profiles depth-wise, it is possible to simply fit the modelled carrier density profile across a GB to the measured profile extracted from PL calibrated carrier density images, avoiding the complexity of modelling the PL signal. Modelling the PL signal, however, allows the method to be applied to samples with non-uniform carrier profiles depth-wise, such as single-side passivated samples used in this work, which significantly broadens the applicability of the method, as explained further below.

# 4.3 Experimental methods

## 4.3.1 Sample Preparation

Two groups of p-type boron doped mc-Si wafers were used in this work. Wafers from the first group were around 180 $\mu m$ thick and were cut from a commercially grown directionally solidified ingot. Wafers from the second group were cut from a different ingot, with a thickness of around 330 $\mu m$. All the wafers were further cut into smaller pieces, followed by a chemical etching using HF acid and $HNO_3$ to remove saw damage, and to create an optically planar surface. Having such a planar surface is necessary for our simplified modelling of the PL emission to be valid as mentioned above. Although

the chemical etching can sometimes cause surface pits near GBs, these do not have a significant impact in the PL images.

Sister wafers in the first group were further divided into two series. Wafers in the first series were phosphorus gettered and then received an aluminium oxide film deposited by plasma-assisted atomic layer deposition (PA-ALD) together with their non-gettered sister wafers. Sister wafers in the second group were all phosphorus gettered, then divided into two series. The first series received a silicon nitride film on both surfaces, while their sister wafers received silicon nitride film on the front surfaces and a thin metallic aluminium film (approximately $10\,nm$) on the rear surfaces using metal evaporation, to achieve instantaneous rear surface recombination conditions [124]. The surface recombination velocity at the rear surface ($S_{rear}$) is assumed to be given by its maximum value, $3 \times 10^6\ cm/s$ [125]. Silicon nitride films were deposited by plasma enhanced chemical vapour deposition (PECVD). The double-side passivated wafers were used to estimate the bulk lifetime for modelling, while the single-side passivated wafers were used to investigate GB behaviour.

## 4.3.2 PL Imaging

PL images were captured with a BT Imaging LIS-R1 tool with high magnification lens, giving a lateral spatial resolution of 22 µm per pixel. The measurement setup is described in detail in Section 2.2.2.

As input parameters, our model requires the bulk lifetime of the neighbouring grains ($\tau_1(\Delta n), \tau_2(\Delta n)$) to be determined. The injection dependent bulk lifetimes were measured in the intra-grain regions, far away from the GB, via a series of calibrated PL lifetime images captured at different injection levels of the double-side passivated samples. The PL images were calibrated into lifetime images using the calibration method described in Chapter 3. A carrier de-smearing technique [84], as described in Section 2.2.2.3, was applied to the calibrated lifetime images to account for the influence of lateral carrier smearing within the sample and thus to allow more accurate extraction of the intra-grain lifetime. It was assumed that negligible surface recombination occurs at both the front and the rear surfaces as the wafers were well

passivated with $S_{eff} < 10\ cm/s$, verified by comparison with monocrystalline control wafers.

## 4.4 Results and discussion

### 4.4.1 Double-side passivated sample before and after phosphorus gettering

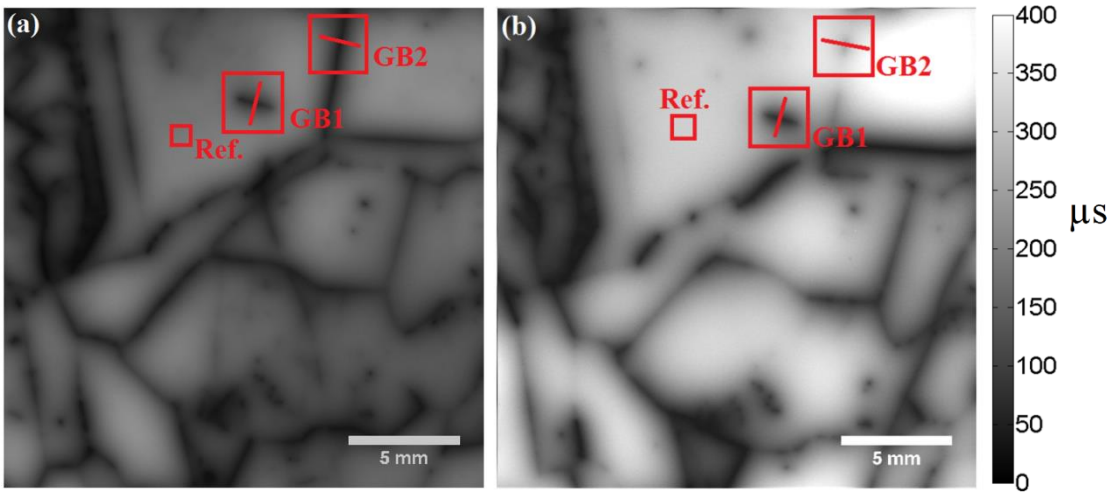


**Figure 4.3 - Calibrated lifetime (in $\mu s$) image of (a) an as-grown $Al_2O_3$ passivated mc-Si wafer (b) a gettered $Al_2O_3$ passivated sister wafer. The same scale is used for both images for direct comparison of the lifetime values. Ref. represents the reference region that is used for the calculation of the scaling factor $K$.**

Figure 4.3 shows calibrated lifetime images of an as-grown mc-Si wafer and a gettered sister wafer from the first group. Both images are taken with the same incident photon flux ($\phi = 2.3 \times 10^{17}\ cm^{-2}s^{-1}$). Comparing Figure 4.3(a) and (b), it can be seen that the lifetime of intra-grain regions improves after phosphorus gettering, due to the removal of impurities in the bulk. While some GBs become more recombination active, the opposite behaviour is observed in other GBs.

We extracted the PL intensity profiles across several selected GBs and fitted the simulated PL profiles according to the method described above to determine their corresponding $S_{GB}$. We first applied our model to study the response of two highlighted GBs (GB1 and GB2) to phosphorus gettering under the same photon excitation condition. The fitting result is shown in Figure 4.4. The simulated PL profile agrees

well with the measured PL profile, demonstrating the applicability of the method. The small discrepancy between the simulated PL profile and the measured PL profile at regions very close to the GB might be due to optical artefacts, such as the focussing of the imaging lens or light scattering in the silicon detector, as explained in Section 2.2.2.1, which has not been completely corrected for, which cause blurriness in the acquired images especially at sharp features such as a strongly recombination active GB. Our result shows that while the $S_{GB}$ of GB1 increases from 890 $cm/s$ to 1810 $cm/s$, the $S_{GB}$ of GB2 decreases from 1130 $cm/s$ to 230 $cm/s$ after gettering.

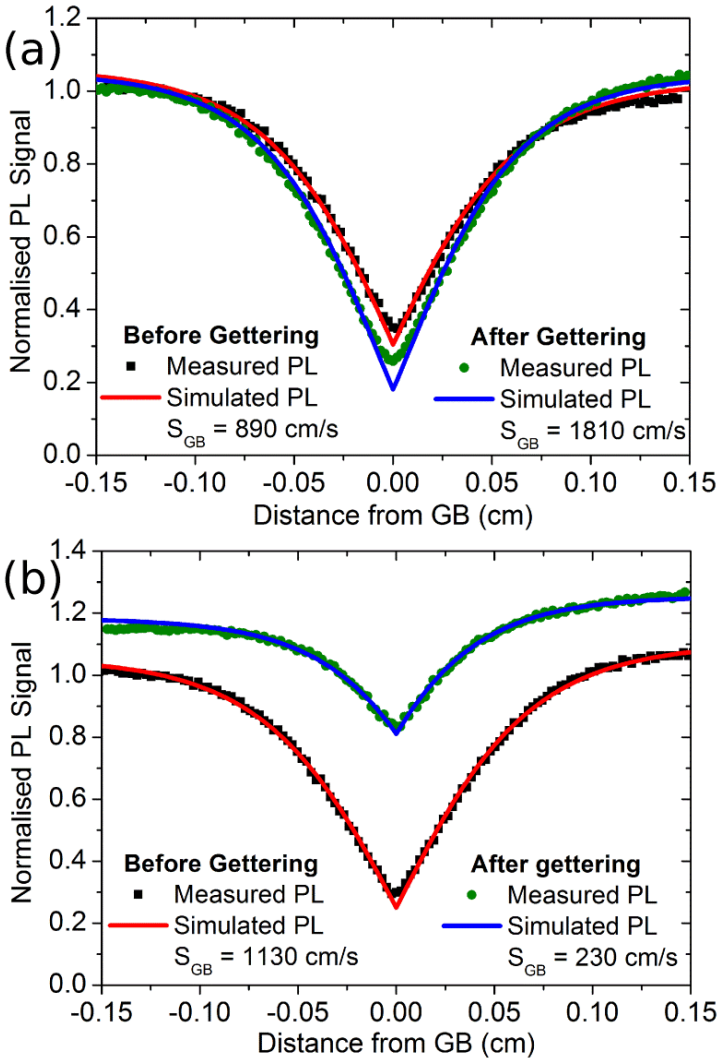


**Figure 4.4 - Simulation fitting of (a) GB1 (b) GB2, as highlighted in Figure 4.3, before and after gettering. The PL signal is normalised against the average PL signal of the highlighted reference region in Figure 4.3, which is used for the calculation of the scaling factor *K*. Note that the normalisation factors for the PL profiles are different due to different lifetimes in the reference regions.**

Note that the extracted $S_{GB}$ value only represents the surface recombination velocity of a GB at a particular injection level. Even with the same generation rate, the excess carrier density at GBs can be different after gettering due to the change in their recombination properties and the variation in the intra-grain lifetime. To account for this, we applied our model to six individual PL images of each sample taken at different injection levels, and determined $S_{GB}$ of GB1 before and after gettering, as a function of injection level at the GB. We used our model simulated minority carrier density at the GB to represent the injection level at which the $S_{GB}$ value was extracted. The result is shown in Figure 4.5.

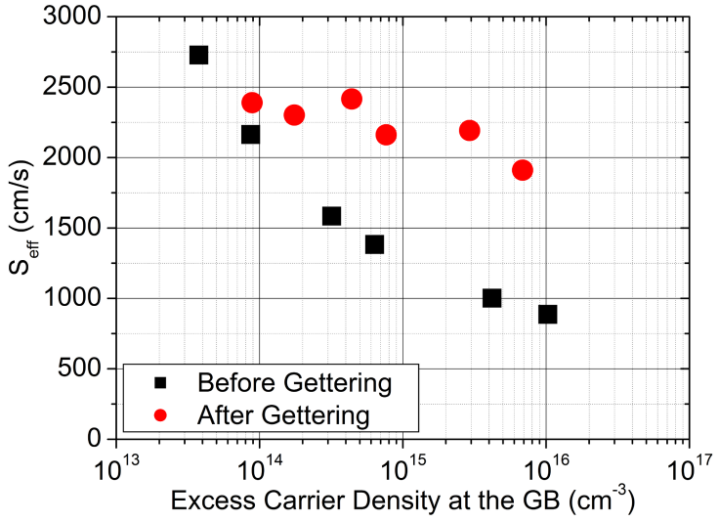


**Figure 4.5 - Injection dependent $S_{GB}$ of GB1, as highlighted in Figure 4.3, before and after gettering.**

GB1, in general, becomes more recombination active after gettering except at low injection ($\Delta n \ll 1 \times 10^{14}\ cm^{-14}$), in which case the recombination strength is largely unchanged. Before gettering, GB1 exhibits a strong injection dependence, with $S_{GB}$ decreasing significantly as injection level increases. This is similar to the recombination property of decorated dislocations, in which the enhancement in the recombination strength due to coulomb potential, created by the capture of majority carriers by electronic states at the dislocation, is thought to be reduced as the minority carrier concentration increases [126]. After gettering, the injection dependence is much less pronounced, suggesting a possible change in the origin of the recombination activity.

Note also the asymmetrical carrier profile on either side of the GB, as can be observed in Figure 4.4(b), due to variation in the bulk lifetime between neighbouring grains. This variation can induce errors in signal contrast methods, but does not impact the extracted injection dependent $S_{GB}$ values determined in this work. The injection dependent $S_{GB}$ of a GB represents the intrinsic property of a GB and is independent of the lifetime of the neighbouring grains forming the GB. The lifetime of the neighbouring grains does not impact the recombination strength of a GB directly, but indirectly through affecting the carrier concentration at the GB due to the injection dependent nature of the recombination properties of a GB.

There are two main limitations in applying the proposed model to double-side passivated samples. Firstly, our method assumes that the extracted PL profile is not affected by the presence of other nearby electrically active structural defects, such as a second GB. This would require the selected GB to be located several diffusion lengths away from other recombination centres. This can be satisfied by selecting GBs located between two large grains. However, carrier diffusion lengths can reach 1 $mm$ or above in well passivated samples, especially after gettering. This significantly limits the number of GBs that can be studied. Secondly, the injection dependent lifetime values of both neighbouring grains are used as input parameters for the fitting. The quality of fit as well as the fitting result depends strongly on the accuracy of the intra-grain lifetime values used. The close proximity of other GBs can increase uncertainty in these lifetime values owing to carrier smearing (Section 2.2.2.3), which in turn can lead to a large uncertainty in the fitting result.

## 4.4.2 Single-side passivated sample

To account for the limitations stated above, we have also applied our model to single-side passivated mc-Si wafers with infinite surface recombination at the rear surfaces, achieved by evaporating a thin layer of aluminium. This significantly reduces the effective minority carrier diffusion length within the samples, hence allowing more closely spaced GBs to be studied. Moreover, this also reduces the sensitivity of the fitting on the intra-grain lifetime, as the carrier concentration on both sides of the GB is limited by carrier transport to the rear surface, due to the infinite rear surface

recombination velocity. We chose to use mc-Si wafers with a thickness of around 330 μ$m$ instead of the more typical 180 μ$m$ wafers to allow for higher excess carrier densities inside the sample, which increases the signal to noise ratio in the PL measurements. This also allows a reasonable degree of carrier diffusion, preventing the region of influence of the GBs from becoming too narrow to be observed with the spatial resolution of the PL imaging setup.

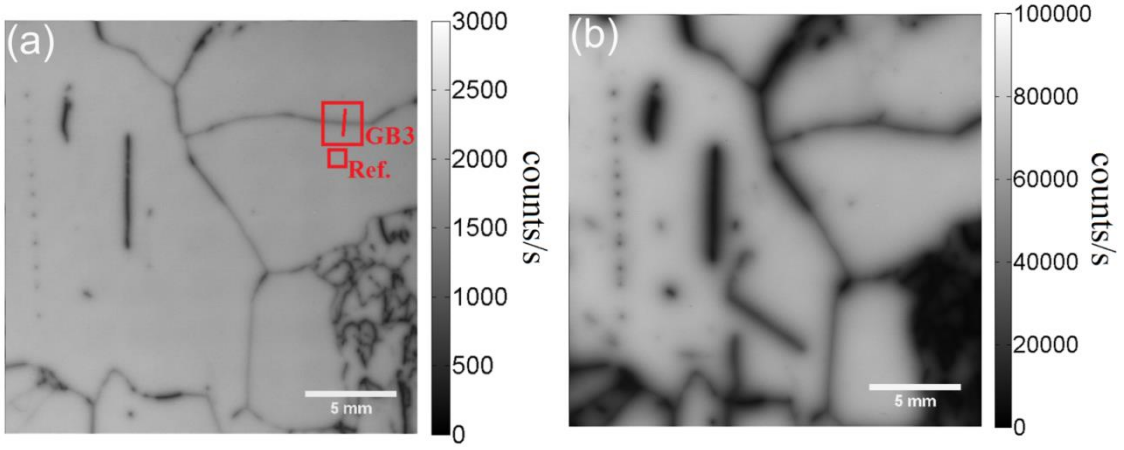


**Figure 4.6 - PL image of a (a) single-side passivated mc-Si wafer (b) double-side passivated sister wafer. Ref. represents the reference region that is used for the calculation of the scaling factor *K*. The PL signal is normalised against the exposure time of each PL image. Note that the scales of the two images are different.**

Figure 4.6 shows PL images of such a single-side passivated sample and a double-side passivated sister wafer, taken with the same incident photon flux ( $\phi = 2.7 \times 10^{18}\ cm^{-2}s^{-1}$). The PL image of the single-side passivated sample is much sharper compared to the one in the double-side passivated case, due to a large reduction in the carrier smearing as a result of significantly shorter effective minority carrier diffusion lengths. The significant reduction in carrier smearing might also allow extending the work to characterise some of the closely packed dislocation networks or loops, which are otherwise very difficult to study in well passivated samples due to the overlapping influence of multiple dislocations.

Figure 4.7 shows the measured PL profile and its corresponding profile fitting for GB3, highlighted in Figure 4.6(a). The bulk lifetimes $(\tau_1(\Delta n), \tau_2(\Delta n))$ of the neighbouring grains are required for the profile fitting and were measured from a double-side passivated sister wafer, Figure 4.6(b), after applying the carrier de-smearing technique

[84]. Good agreement is found between the measured PL profile and the simulated PL profile, demonstrating that our model can be applied not only on well passivated samples, but also on samples with strongly non-uniform carrier density profiles depth-wise, provided that the bulk properties and the boundary conditions are well known.

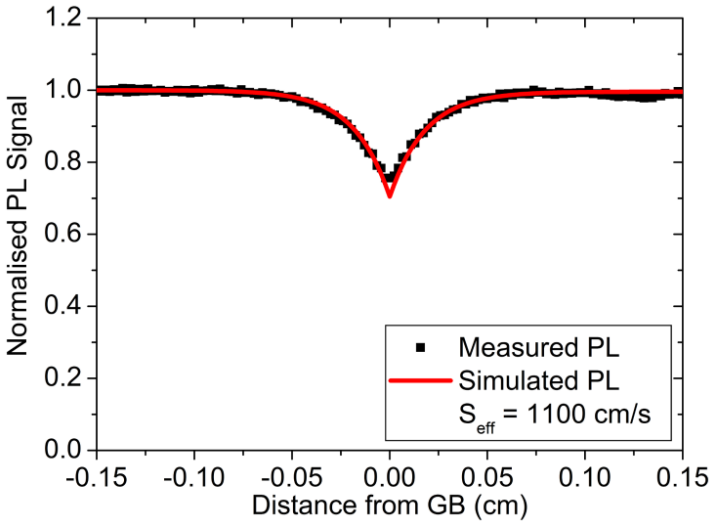


**Figure 4.7 - Simulation fitting of GB3, as highlighted in Figure 4.6(a). The PL signal is normalised against the average PL signal of the highlighted reference region in Figure 4.6(a), which is used for the calculation of the scaling factor *K*.**

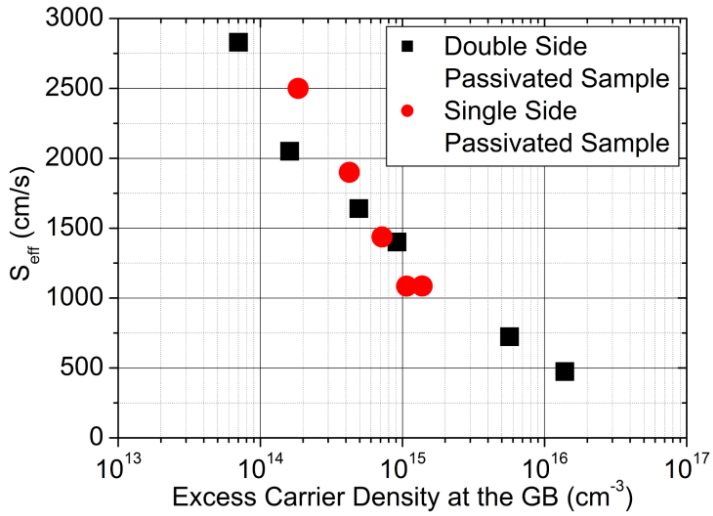


**Figure 4.8 - Injection dependent $S_{GB}$ of GB3, as highlighted in Figure 4.6, extracted from a single-side passivated sample and a double-side passivated sister wafer.**

Figure 4.8 compares injection dependent $S_{GB}$ of GB3 extracted from a single-side passivated sample and a double-side passivated sister wafer. The extracted values agree

reasonably well with each other. The small discrepancy may be due to one of the following reasons. Firstly, for the single-side passivated sample, due to the large variation in the carrier profiles at the GB, we adapted a weighted average carrier concentration ($\Delta n_{avg} = \frac{\int_0^\infty \Delta n^2 dx}{\int_0^\infty \Delta n dx}$), proposed by Bowden *et al.* [108] for determining lifetime in silicon bricks, to represent the average carrier concentration at the GB. Different averaging methods can lead to a different average value of the excess carrier density and can influence the apparent injection dependence of the extracted $S_{GB}$ values.

Moreover, in our model, we assume a constant $S_{GB}$ value for the entire GB. This might not be strictly true for GBs in single-side passivated samples, as the carrier profiles are highly non-uniform depth-wise and the $S_{GB}$ of some GBs can be strongly injection dependent, as shown above. The extracted $S_{GB}$ hence only represents an average surface recombination velocity of a GB over a range of injection levels. Furthermore, due to the infinite surface recombination at the rear surfaces, higher injection densities are difficult to achieve in a single-side passivated wafer even with a high intensity illumination source. This limits the studies of GB behaviour to low or moderate injection levels.

### 4.4.3 Sensitivity Studies

In order to determine the limitations of our proposed method for quantifying the recombination strength of a GB, the sensitivity of the PL profile for both double-side and single-side passivated samples is evaluated. In the simulation, we assume that the double-side and the single-side passivated samples have a thickness of $150\ \mu m$ and $300\ \mu m$ respectively, similar to the thickness of the mc-Si wafers used in this work after chemical polishing. Both samples are illuminated with the same incident photon flux, $2.7 \times 10^{18}\ cm^{-2}s^{-1}$, at 808 nm. Note that even with the same incident photon flux, the injection levels in both samples are different.

Firstly, the sensitivity of the PL profile on $S_{GB}$ is investigated, as shown in Figure 4.9. The intra-grain bulk lifetimes for both samples are assumed to be injection independent in this simulation and are set to be $300\ \mu s$. For the double-side passivated sample, the PL profile is sensitive to variation in $S_{GB}$ when $S_{GB} \ll 1000\ cm/s$ and only varies slightly once $S_{GB}$ exceeds $2000\ cm/s$. This is due to the fact that the recombination rate

in the latter case is limited by the transport of carriers to the GB rather than its intrinsic recombination properties. On the other hand, the PL profile in the single-side passivated sample does not saturate when $S_{GB}$ increases, as shown in Figure 4.9(b), implying that single-side passivated samples are more suitable to study strongly recombination active GBs.

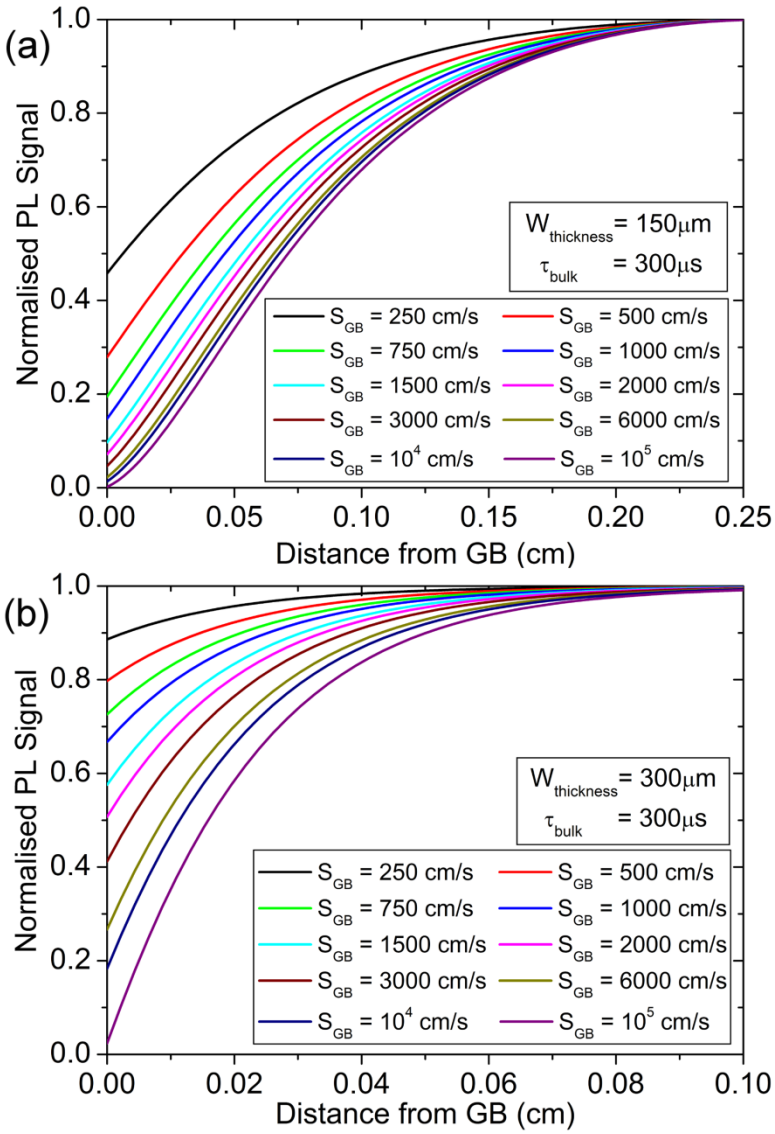


**Figure 4.9 - Sensitivity of PL profile on $S_{GB}$ for a (a) double-side passivated wafer (b) single-side passivated wafer. Only one side of the PL profile is shown as the PL profile is symmetrical. The bulk lifetimes of the neighbouring grains are assumed to be injection independent and are set to be 300 $\mu s$.**

Secondly, the sensitivity of the PL profile on the intra-grain bulk lifetime is evaluated. In this simulation, we fix the lifetime on one of the neighbouring grains for reference,

and then observe the variation of the PL profile while changing the lifetime of the other grain to a certain percentage of the reference grain. Our result, as shown in Figure 4.10 shows that the PL profile on a double-side passivated sample is very sensitive to the intra-grain lifetime. A 10% difference in the intra-grain lifetime can significantly change the shape of the PL profile. This suggests that uncertainty in the measured intra-grain lifetime can result in a relatively large uncertainty in the fitting. In contrast, the PL profile on the single-side passivated sample is less dependent on the bulk lifetime. As a result, the fitting will have a higher tolerance for uncertainty in the measured bulk lifetime.

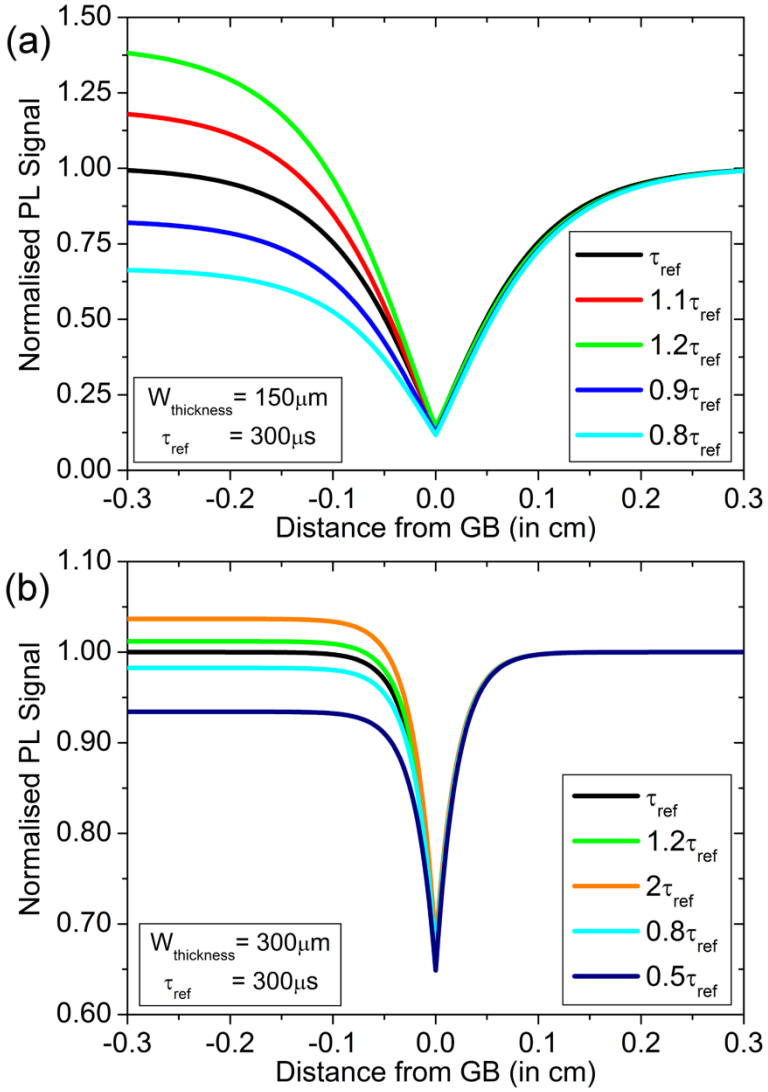


**Figure 4.10 - Sensitivity of PL profile on intra-grain bulk lifetime for a (a) double-side passivated wafer (b) single-side passivated wafer. $S_{GB}$ of the GB is set to be 1000 $cm/s$. The bulk lifetimes of the reference grains are set to be 300 $\mu s$.**

However, the extraction method, when applied to single-side passivated samples, is less sensitive to slightly recombination active GBs ($\ll 200\ cm/s$). Those GBs have a very shallow PL profile, as shown in Figure 4.11, and the reduction in the PL signal at the GB is comparable to the measurement noise, which limits the fitting accuracy. Such GBs are attributed an upper limit value of $100\ cm/s$ in Chapter 5 and $200\ cm/s$ in Chapter 6. The higher attributed value in Chapter 6 is due to thinner samples used in the studies, which reduce the sensitivity of the PL profile on $S_{GB}$, owing to the infinite surface recombination at the rear. This is demonstrated in Figure 4.11, which compares PL profiles across a GB with $S_{GB}$ of $200\ cm/s$ in 300 $\mu m$ and 150 $\mu m$ thick wafers.

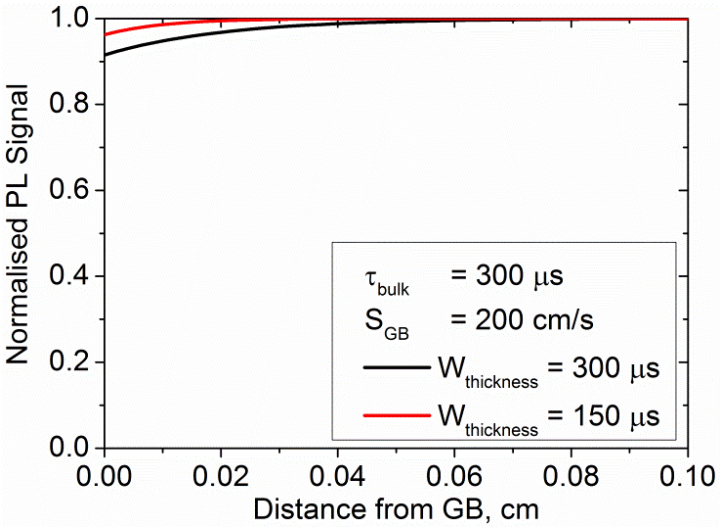


**Figure 4.11 - PL profiles across a GB with $S_{GB}$ of $200\ cm/s$ in 300 $\mu m$ and 150 $\mu m$ thick single-side passivated wafers. The bulk lifetimes of the neighboring grains are assumed to be injection independent and are set to be 300 $\mu s$. The wafers are assumed to be illuminated with the same incident photon flux, $2.7 \times 10^{18}\ cm^{-2}s^{-1}$, at 808 nm.**

# Conclusions

This chapter presents a direct fitting approach based on the steady state PL imaging technique and 2D modelling of the PL intensity profile across a GB, to determine the effective surface recombination velocities ($S_{GB}$) of GBs in multicrystalline silicon wafers. The method is demonstrated on double-side passivated wafers and single-side passivated wafers. The former allows evaluating $S_{GB}$ of GBs as a function of injection level, but is limited to less recombination active GBs located between large grains. The latter allows more GBs or even some dislocations to be studied, but only allows extraction of $S_{GB}$ values of GBs at low or moderate injection levels. It also requires a double-side passivated sister sample for extracting the bulk lifetime information in the two neighbouring grains, as required for the analysis. The presented method is used for the analysis in the succeeding chapters, in which the method is applied on single-side passivated samples to quantitatively study the recombination behaviours of GBs with different contamination levels from various types of mc-Si ingots, and their response to phosphorus gettering and hydrogenation.

# Chapter 5

# Impact of phosphorus gettering and hydrogenation on the surface recombination velocity of grain boundaries in p-type multicrystalline silicon

## 5.1 Introduction

Grain Boundaries are unavoidable in mc-Si solar cells, and are one of the limiting factors for cell performance. Understanding the origin of their recombination behaviour is necessary for designing processes to reduce or even eliminate their impact. The electrical properties of GBs depend strongly on the geometry of the GB. It was suggested that the recombination strength of GBs can be correlated to their coincidence site lattice (CSL) index. GBs with lower atomic coincidence such as random angle (RA) GBs or Σ27 GBs tend to be more recombination active than GBs with higher atomic coincidence such as Σ3 GBs or Σ9 GBs [5, 20, 127]. The recombination behaviour of GBs depends not only on the atomic coincidence, but also the contamination level in the material and their interactions [5, 20, 22, 27]. Buonassisi *et al.* [22] showed that metal silicide precipitates are more likely to form at GBs with lower atomic coincidence. Chen *et al.* [5] observed a large variation of recombination strength among different types of GBs in heavy contaminated wafers compared to clean or lightly contaminated wafers, in which only a small variation can be observed.

On the other hand, it has been shown that the electrical properties of GBs change after phosphorus gettering [20, 23, 24, 28, 29] and hydrogenation [20, 29-32]. Phosphorus

gettering has been demonstrated to be very effective in improving the overall minority carrier lifetime of mc-Si material through removing impurities from the bulk [128]. Hydrogen, on the other hand, is well known for its ability to passivate different impurities and defects in silicon [129]. However, the effectiveness of phosphorus gettering and hydrogenation is less certain on GBs. Karzel *et al.* [20] studied GBs in wafers cut from two individual mc-Si ingots with different metal contamination levels and observed a distinct difference in their responses to gettering and hydrogenation. Since phosphorus gettering and hydrogenation are incorporated in common solar cell fabrication during the formation of the pn junction, and during firing of metal contacts through the antireflection coating, in which hydrogen in the silicon nitride film diffuses into the bulk, understanding the response of GBs to those two processes is important, as it allows the possibilities of mitigating their detrimental effects during solar cell production.

Although GBs have been studied extensively in the literature, the underlying mechanisms of GB behaviour are still not fully understood. One of the challenges has been the lack of an accurate and reliable method for quantifying the recombination activities of GBs which can be applied to a large number of GBs for a statistically relevant analysis. In this chapter, we quantify the recombination strength of GBs in terms of their effective surface recombination velocities ($S_{GB}$), using the method presented in Chapter 4. This provides a more meaningful and absolute measure of the recombination properties of a GB compared to the commonly used signal contrast methods [5, 20], which give only a qualitative representation, and strongly depend on the lifetime of the intra-grain regions. We compare $S_{GB}$ of a relatively large number of GBs in mc-Si wafers with different contamination levels, and evaluate their variation after phosphorus gettering and hydrogenation, aiming to obtain a better understanding of the recombination activities of GBs. The injection dependent behaviour of GBs is investigated as different decorating impurities may give rise to different injection dependent recombination properties [19]. In addition to band-to-band PL imaging, sub-bandgap PL emitted from several selected GBs is also studied through applying micron scale photoluminescence spectroscopy at low temperature ($79\,K$). Lastly, the detrimental impact of GBs on a solar cell device is discussed, based on numerical simulations.

# 5.2 Experimental Methods

## 5.2.1 Sample Preparation

Mc-Si wafers used in this work were around $330\ \mu m$ thick and were cut at heights of 33%, 68% and 91% from the bottom of a commercially grown p-type boron doped directionally solidified ingot. The wafers have a background doping of around $1.3 \times 10^{16}\ cm^{-3}$, $1.5 \times 10^{16}\ cm^{-3}$ and $1.9 \times 10^{16}\ cm^{-3}$ respectively and are referred as W33, W68 and W91 in this work. The concentration of metallic impurities in the ingot has been measured previously by neutron activation analysis (NAA) [130]. The interstitial iron concentration in the same ingot before and after gettering and hydrogenation was also studied by Tan *et al.* [131] and Liu *et al.* [132] through QSSPC and PL imaging techniques. The different positions in the ingot lead to large differences in the amount of metallic impurities in the wafers, for example, the total concentration of iron in the wafers studied here was found to be approximately $2 \times 10^{14}\ cm^{-3}$ for wafers from 33% and 91% of the ingot and $5 \times 10^{13}\ cm^{-3}$ for wafers from 68% of the ingot [130].

After a short chemical etching using HF and $HNO_3$ acid to remove saw damage, sister wafers from each position were divided into four groups (A, B, C, D). Wafers from groups A and C were phosphorus gettered. Phosphorus gettering was performed through subjecting the wafers to a 30 min $POCl_3$ diffusion at 880℃, followed by an extended annealing in an $N_2$ ambient for more than 12 hours at 600℃ in the same diffusion furnace, resulting in sheet resistance values of around $20\ \Omega/\square$ measured using a 4-point probe. Such extended gettering has been shown to produce the most effective gettering for mc-Si [133, 134]. The wafers were then chemically etched to remove the phosphorus diffused layers. Afterward, wafers from group A and B received silicon nitride films on both surfaces for passivation, while their sister wafers from group C and D received silicon nitride films on the front surfaces and thin metallic aluminium films (approximately $10\ nm$) on the rear surfaces using metal evaporation, to achieve instantaneous rear surface recombination conditions. The double-side passivated wafers from group A and B were used to estimate the bulk lifetime required for the modelling, while the single-side passivated wafers from group C and D were used to investigate

GB behaviour.

For hydrogenation studies, all wafers in each group had their dielectric or metallic films etched off. All samples were then re-coated with fresh silicon nitride films and were fired in a rapid thermal processing (RTP) furnace (Unitemp UTP-1100) for 3 min at 700℃ in $N_2$ ambient to produce bulk hydrogenation. After firing, all annealed silicon nitride films were removed via HF dip and the samples were re-passivated with fresh films for measurements. All samples were chemically etched to remove around 3 $\mu m$ of silicon using HF and $HNO_3$ acid after each removal of the surface films, to remove any surface defects which may have formed during the firing or film deposition. The deposited silicon nitride films in this work were around 85 nm thick and were deposited with a Roth & Rau AK400 plasma enhanced chemical vapour deposition (PECVD) system with deposition temperatures between 250℃ and 300℃.

Note that instead of the more typical 180 $\mu m$ thick wafers, thicker mc-Si wafers were chosen in this work to allow for higher excess carrier densities inside the single-side passivated samples. This increases the signal to noise ratio in the PL images and allows the measurements to be performed with a lower incident photon flux, which is necessary for the injection dependence analysis described below. It should also be mentioned that this ingot was grown approximately 10 years ago, and may not necessarily represent the state of the art mc-Si materials.

## 5.2.2 Micro-photoluminescence spectroscopy

Micro-photoluminescence spectroscopy was performed with a Horiba Jobin-Yvon T6400 micro-Raman spectrometer. The excitation source is a 532 nm laser with an estimated power of 10mW and a spot size of 2-3 microns. The emission is passed through a monochromator with a 150 lines/mm grating, and detected by a liquid nitrogen cooled InGaAs detector.

## 5.3 Results and discussion

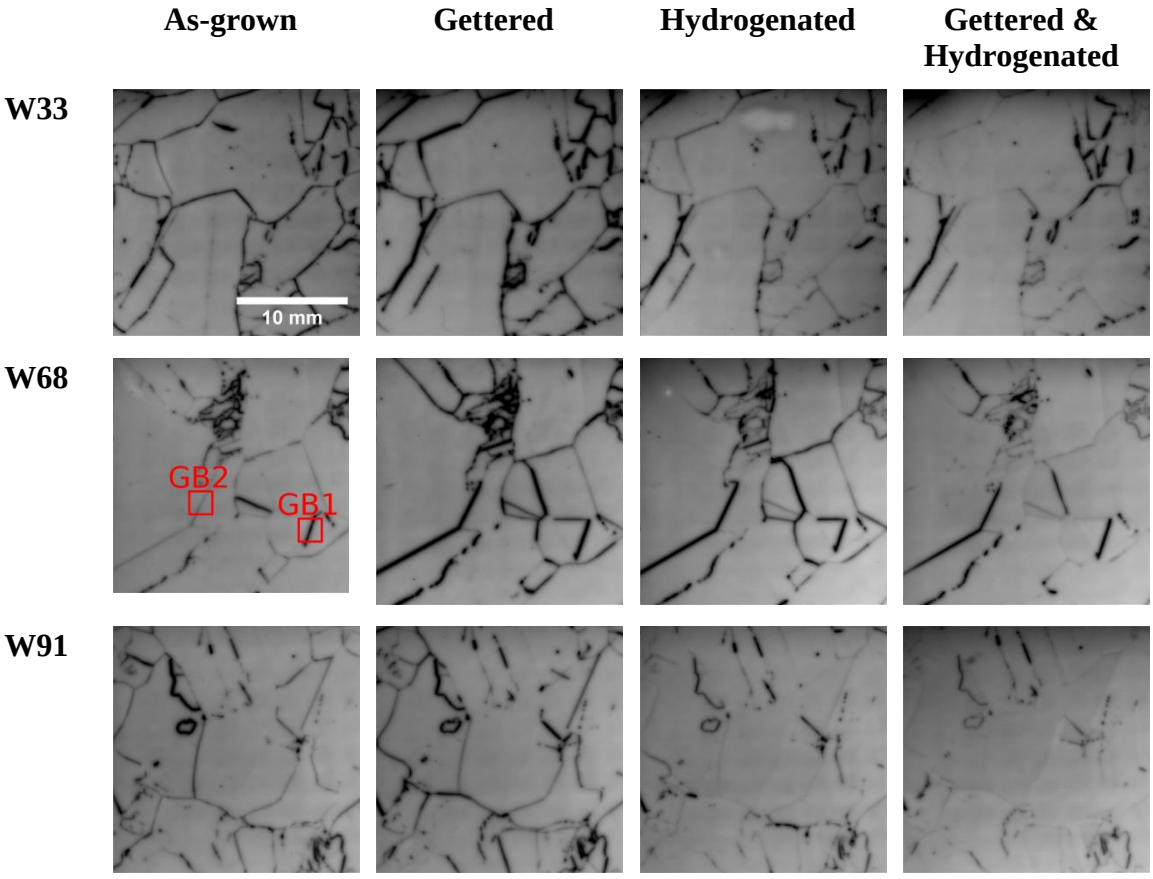


**Figure 5.1 - PL images of several selected single-side passivated mc-Si wafers studied in this work before and after gettering and hydrogenation. W33, W68 and W91 represent samples from 33%, 68% and 91% from the bottom of the mc-Si ingot respectively. The individual PL images are normalised against the PL intensity of intra-grain regions far away from crystal defects. The same scale is applied in all the images. GB1 and GB2 are two selected GBs used for micro-photoluminescence spectroscopy measurements in Section 5.3.5.**

Figure 5.1 shows PL images of several selected mc-Si wafers studied in this work before and after gettering and hydrogenation. It illustrates that the recombination behaviour of GBs varies among the studied mc-Si ingot and after gettering or hydrogenation. Figure 5.2 compares the influence of phosphorus gettering and hydrogenation on the lifetime of the intra-grain regions and their overall impact on $S_{GB}$ of GBs from three different positions of the ingot. The intra-grain lifetimes are measured in regions far away from the GBs, from PL calibrated lifetime images after applying carrier de-smearing technique [84], as described in Section 2.2.2.3. The $S_{GB}$ of

GBs are extracted from PL images captured under the same photon flux of $2.7 \times 10^{18}\ cm^{-2}s^{-1}$. The reasons for comparing $S_{GB}$ values under the same excitation condition are explained below in Section 5.3.6. Note that a higher GB effective surface recombination velocity ($S_{GB}$) corresponds to greater recombination.

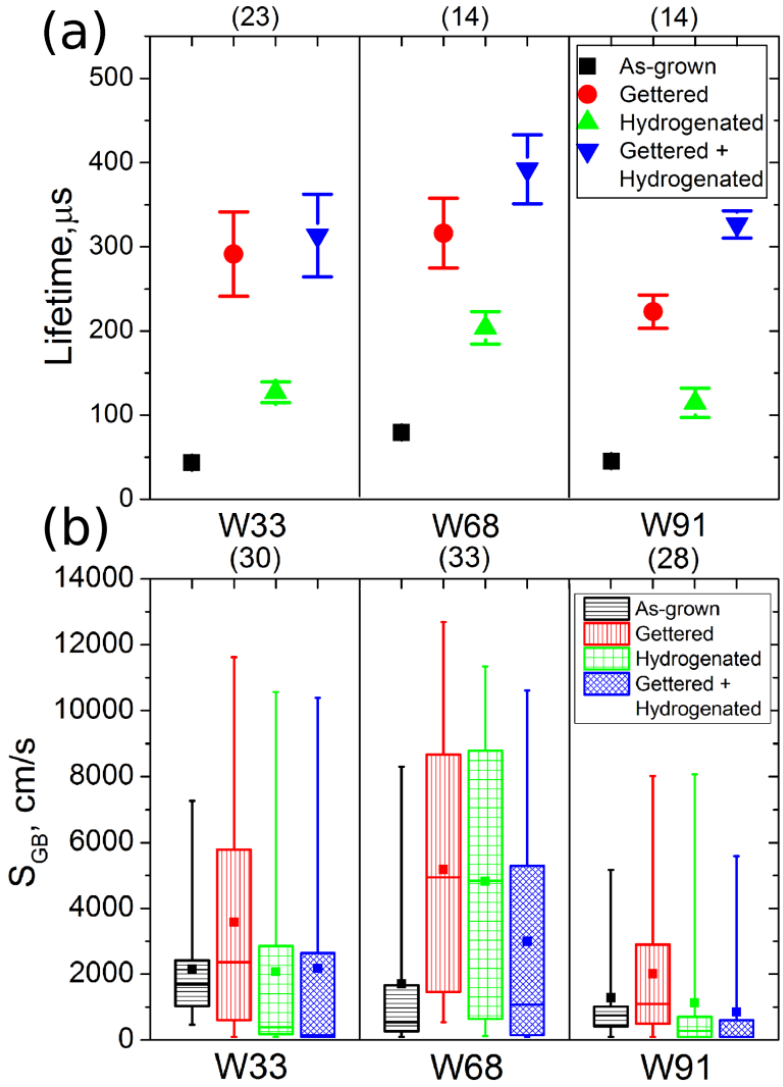


**Figure 5.2 - (a) Average $\tau_{bulk}$ of several intra-grain regions from three positions of a mc-Si ingot, before and after gettering and hydrogenation. The lifetime values are measured with an excess carrier density of $1 \times 10^{15}\ cm^{-3}$. The error bars denote one standard deviation of the data. The errors for the as-grown samples are small, only around 4 $\mu s$, hence the error bars are not visible in the figure. (b) $S_{GB}$ of various GBs before and after gettering and hydrogenation. The median values, as well as 25 and 75 percentiles are marked by horizontal bars, the means by squares. W33, W68 and W91 represent samples from 33%, 68% and 91% from the bottom of the mc-Si ingot respectively. The total numbers of sampled intra-grain regions and GBs are shown above the y-axis.**

Before any processes, the average intra-grain lifetime of wafers from the middle of the ingot is the highest among all the samples and their median $S_{GB}$ value of the GBs is the lowest. The former is likely to be due to lower impurity concentrations in wafers from the middle of an ingot compared to wafers near the bottom and the top of the ingot due to segregation from the liquid phase and diffusion from the crucible during solidification [130]. The latter is consistent with the study by Chen *et al.* [5], who suggested that GBs are not intrinsically electrically active, and only become recombination active when decorated with impurities such as iron.

The intra-grain regions from three different positions of the ingot respond similarly to gettering and hydrogenation. Phosphorus gettering is very effective for improving the intra-grain lifetimes especially on samples with higher levels of impurities, in which their lifetimes after gettering are even comparable to the gettered lifetimes on cleaner wafers from the middle of the ingot. The benefit of hydrogenation alone on the intra-grain lifetime is clear, but it is not as effective as phosphorus gettering. Performing both gettering and then hydrogenation results in the highest intra-grain lifetimes.

In terms of the GB behaviour, a similar trend can be observed for the surface recombination velocities of GBs near the bottom and the top of the ingot. Their median increases slightly after gettering and decreases dramatically after hydrogenation. On the other hand, GBs located close to the middle of the ingot react differently. Gettering or hydrogenation alone induces a significant increase in the median $S_{GB}$ values on as-grown GBs. Unexpectedly, the median $S_{GB}$ values of these cleaner samples after either gettering, hydrogenation, or both processes, are even higher than the medians of the more contaminated samples. In order to explore the cause of such behaviour, we next compare the variation of the recombination strength of individual GBs after each process.

### 5.3.1 Influence of gettering or hydrogenation on as-grown GBs

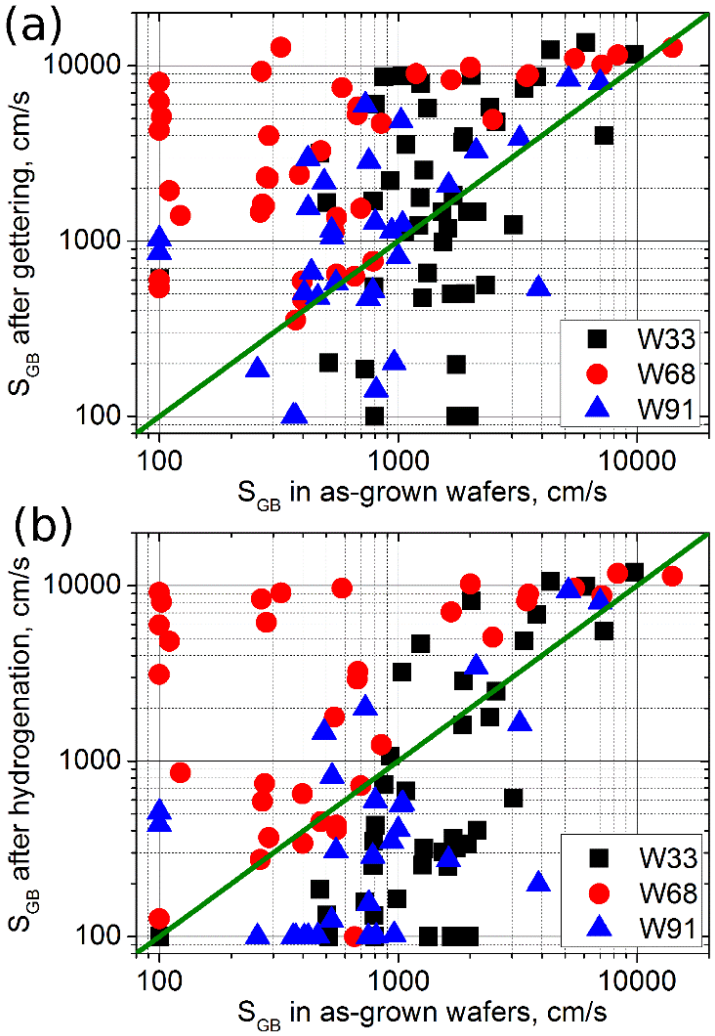


**Figure 5.3 - $S_{GB}$ of individual GBs before and after (a) gettering and (b) hydrogenation. W33, W68 and W91 represent GB location, from 33%, 68% and 91% from the bottom of the mc-Si ingot respectively. The diagonal line represents zero variation. Data points above this line correspond to GBs with an increase of $S_{GB}$ after processes, and vice versa. The value of 100 $cm/s$ is the lower detection limit of the PL imaging based measurement technique used.**

Figure 5.3 shows $S_{GB}$ values of each GB before and after either gettering or hydrogenation alone. Comparing Figure 5.3(a) and (b), it can be seen that the impact of gettering and hydrogenation is similar on as-grown GBs. Nearly all GBs from the middle of the ingot become more recombination active after gettering or hydrogenation alone, while GBs from the top and bottom regions have a more varied response. While

the reduction in their $S_{GB}$ values could be due to external gettering of impurities at GBs to the heavily doped phosphorus diffused layers, or due to hydrogenation, the causes for the increase in their $S_{GB}$ values are less clear. The striking feature is that hydrogenation does not reduce but in fact increases the recombination strength of nearly all the GBs from the middle of the ingot and some of the GBs from the top and bottom regions. This increase is unlikely to be caused by the injection dependence of $S_{GB}$ and the increase of excess carrier concentration at the GB after the processes as a result of higher lifetime in the intra-grain region, owing to the use of single-side passivated samples coupled with the fact that GBs tend to be less active as injection level increase, as described below. The similar trend in Figure 5.3(a) and (b) suggests that it may be the thermal treatment itself that is the main driving force causing the increase in the recombination properties of GBs after gettering or hydrogenation.

Note that this observation cannot be due to internal gettering of metal impurities from deep in the intra-grain regions [135] as the time duration for the hydrogenation process is only around 3 minutes, which is too short for impurities such as iron to diffuse to the GBs [50]. Moreover, as-grown GBs, in general, should be more influenced by such internal gettering from deep within the grains, due to the fact that the slow ingot cooling allows more time for impurities to diffuse to or precipitate at GBs.

Other possible mechanisms are therefore considered. Firstly, the high temperature used for the processes could dissolve some small, unstable metal precipitates, leading to a redistribution of impurities [29]. Metal precipitates may exist in different forms, structures or compositions in mc-Si [126, 136-138], and studies have shown that their phases could depend on the thermal history of the material. For example, Buonassisi *et al.* [139] reported that precipitates formed after a lower temperature anneal (655℃) exhibit distinguishing features to those formed as a result of higher-temperature annealing (1200℃) and crystal growth (1414℃). Secondly, in addition to the influence of temperature, the rapid cooling after the high temperature step might drive formation of point defects or metal precipitates with relatively smaller size, compared to larger precipitates formed during ingot cooling in which more time is available for impurity atoms to diffuse and precipitates to grow [136]. These can affect the recombination properties of GBs.

Moreover, Figure 5.2(b) shows that, contrary to as-grown samples, the median $S_{GB}$ values of GBs from the middle of the ingot are higher than the medians of GBs from the top and bottom after gettering or hydrogenation. This suggests that the high temperature steps or the rapid quenching applied, as mentioned above, have more substantial influence on GBs in cleaner samples than GBs in more contaminated samples. The following hypothesis is proposed to explain the observed behaviour. In a clean sample, as-grown GBs are not decorated with metal precipitates; hence there may be no pre-existing precipitation sites around GBs, resulting in the formation of a larger number of small precipitates. On the other hand, in more contaminated samples, metal precipitates around decorated GBs could act as pre-existing sites for metals to precipitate and grow during the thermal processes, leading to metal precipitates with relatively larger sizes and lower densities. It was suggested that, for the same average concentration of impurities, few large precipitates exhibit less recombination activity than many dispersed small precipitates [29, 140].

### 5.3.2 Influence of hydrogenation on GBs with or without a pre-gettering step

Figure 5.4(a) shows the effectiveness of hydrogenation on gettered GBs. Unlike its impact on as-grown GBs, as shown in Figure 5.3(b), it can be seen that hydrogen is very effective in reducing the recombination strength of all gettered GBs, independent of their positions in the ingot. Figure 5.4(b) compares the effectiveness of hydrogenation on GBs with or without a pre-gettering step. It can be seen that GBs with a pre-gettering step tend to benefit more from hydrogenation compared to as-gown GBs. This is in agreement with a previous study by Karzel *et al.* [20]. One possible explanation for the observed behaviour is that hydrogen is more effective in passivating impurities of certain forms such as interstitial impurities or smaller metal precipitates, which may be formed in greater amounts after gettering, as suggested above.

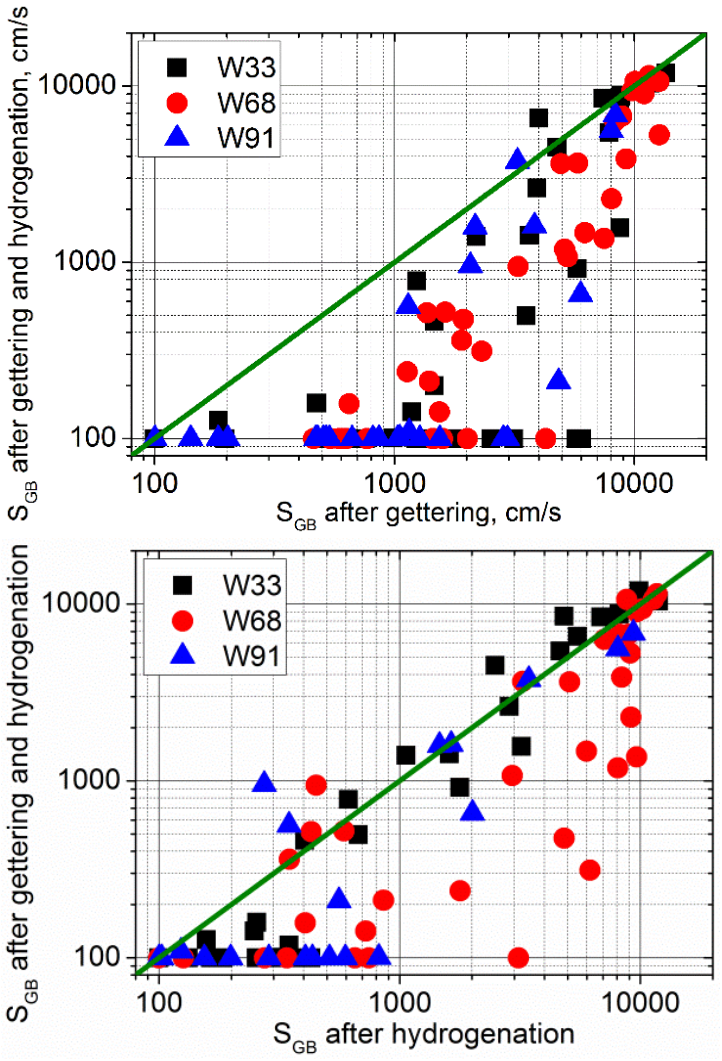


**Figure 5.4 – (a) $S_{GB}$ of gettered GBs before and after hydrogenation. (b) Effectiveness of hydrogenation on GBs with or without a pre-gettering step. W33, W68 and W91 represent GB location, from 33%, 68% and 91% from the bottom of the mc-Si ingot respectively. The diagonal line represents zero variation. Data points above this line correspond to GBs with an increase of $S_{GB}$ after processes, and vice versa. The value of 100 $cm/s$ is the lower detection limit of the PL imaging based measurement technique used.**

### 5.3.3 Influence of both gettering and hydrogenation on as-grown GBs

Figure 5.5 summarises the combined influence of gettering and hydrogenation on as-grown samples, representing the variation of the recombination properties of GBs after these common solar cell fabrication processes combined. A diverse response among various GBs is observed, while some GBs become more recombination active after the

processes, some become less active. This can be due to variations in the GB geometry or type, which can have an impact on the ability to aggregate metal impurities [22, 141].

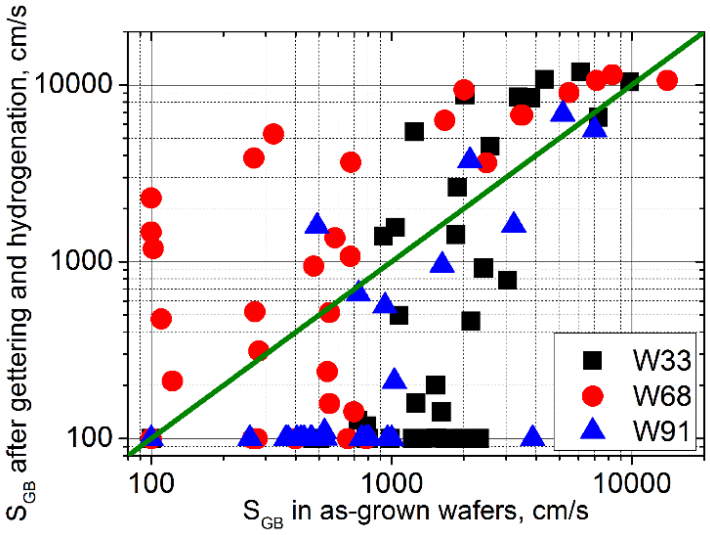


**Figure 5.5 – $S_{GB}$ of individual GBs before and after gettering and hydrogenation. W33, W68 and W91 represent GB location, from 33%, 68% and 91% from the bottom of the mc-Si ingot respectively. The diagonal line represents zero variation. Data points above this line correspond to GBs with an increase of $S_{GB}$ after processes, and vice versa. The value of 100 $cm/s$ is the lower detection limit of the PL imaging based measurement technique used.**

Electron Backscatter Diffraction (EBSD) measurements were performed to identify the GB types. However, around 80% of the sampled GBs were found to be random angle (RA) GBs. The number of GBs of other identifiable types (CSL GBs) is insufficient to allow a statistically relevant comparison of GBs of different types. This is because most of the GBs of other types such as Σ3 or Σ9 GBs are less active [5] and our method is best applied on recombination active GBs with a distinct PL profile, and is not sensitive to inactive GBs ($S_{GB} \ll 100\ cm/s$). The analysis is further complicated by the fact that the electrical properties of RA GBs can vary over a large range as they consist of GBs with a wide range of different misorientation configurations, which cannot be categorised easily. Given these limitations, I am not able to meaningfully compare GBs according to their geometry. Instead, we look into the injection dependence of the $S_{GB}$ of the GBs and use it as an alternative classification method to obtain a better understanding of the root cause of their recombination activities.

## 5.3.4 Injection dependence of $S_{GB}$

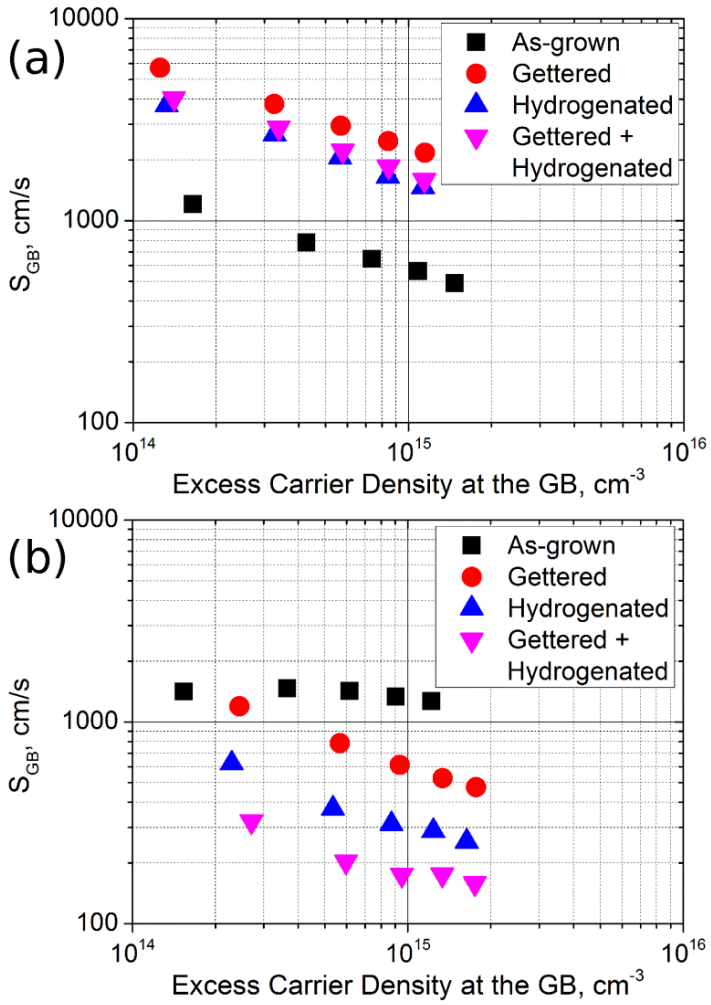


**Figure 5.6 – Injection dependent $S_{GB}$ of GBs of (a) Type A (b) Type B before and after different processes. GBs of type A show a rather strong injection dependence, while GBs of type B exhibit little injection dependence before gettering.**

Our method allows the injection dependence of $S_{GB}$ to be explicitly determined, through applying the modelling to PL images captured at different laser intensities, or injection levels. Figure 5.6 (a) and (b) show two distinct injection dependent behaviours that were commonly observed in the sampled GBs. GBs of type A exhibit similar injection dependence before and after gettering or hydrogenation, while GBs of type B reveal little injection dependence before gettering, but show a larger injection dependence after gettering or hydrogenation, with $S_{GB}$ increasing as the injection level decreases. It is found that most of the GBs from the middle of the ingot are type A, whereas type A and type B GBs exist in a more balanced ratio in wafers from the top and the bottom regions.

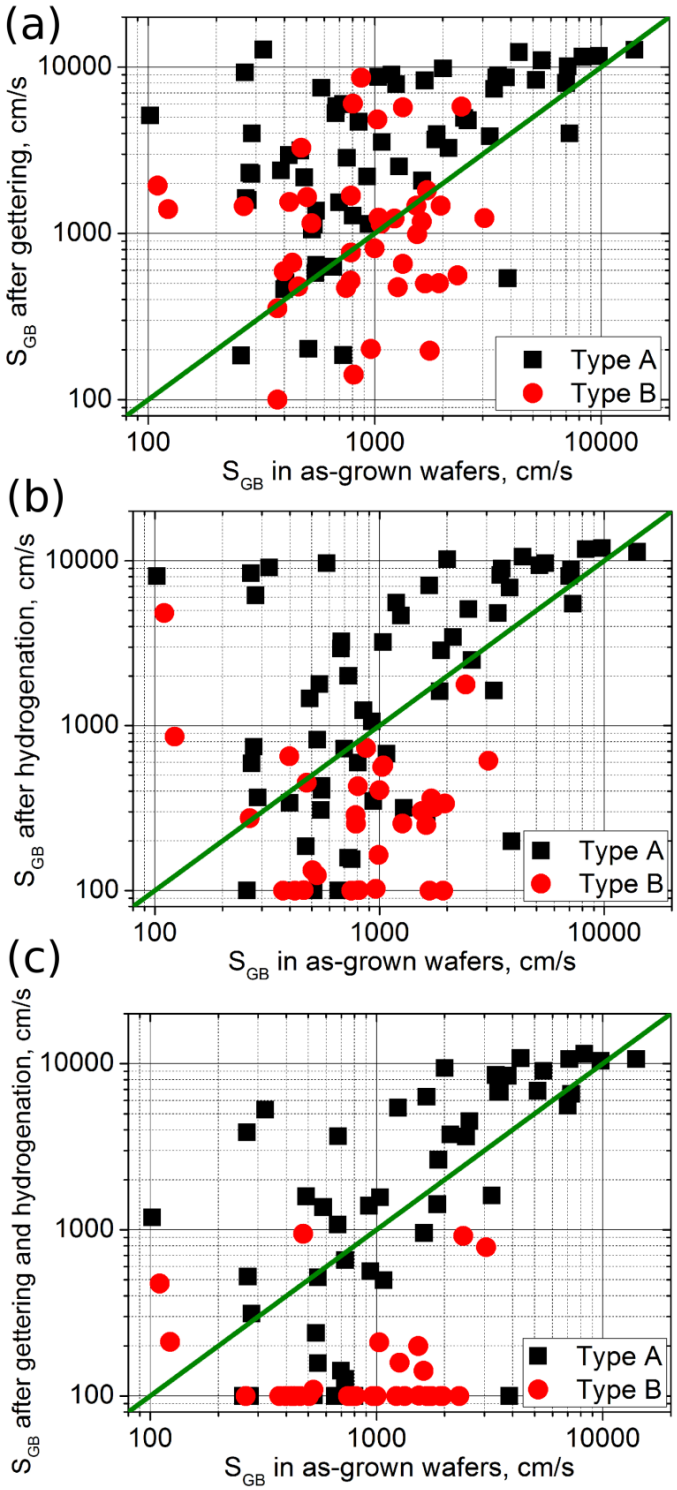


**Figure 5.7 – $S_{GB}$ of GBs, classified according to their injection dependence, before and after (a) gettering (b) hydrogenation (c) gettering and hydrogenation. Type A and Type B represents the injection dependence of the GB as noted in Figure 5.6(a) and (b) respectively. The diagonal line represents zero variation. Data points above this line correspond to GBs with an increase of $S_{GB}$ after processes, and vice versa. The value of $100\ cm/s$ is the lower detection limit of the PL imaging based measurement technique used.**

Figure 5.7 compares the response of type A and type B GBs to gettering and hydrogenation. GBs of type A, in general, become more recombination active after gettering, while GBs of type B have a more varied response. Surprisingly, hydrogenation induces a very different response in the GBs. GBs of type B become less active after hydrogenation, whilst those GBs of type A react diversely. The results here imply that the two types of GBs might have different origins for their recombination activities, and that these origins significantly affect how they react to different process steps. Literature concerning the injection dependent properties of GBs is not common. However, it is well known that impurities in silicon can cause different injection dependent characteristics because of their variations in the energy level and capture cross-sections [19]. It has also been shown that dislocations, when decorated, exhibit a strong injection dependence with their recombination properties, owing to Coulomb band bending [26, 126]. Combining this with the fact that we observe more GBs of type A in the cleaner wafers from the middle of the ingot compared to the more contaminated wafers from the top or the bottom, we speculate that the distinct injection properties between the two types of GBs are caused by different concentrations of various decorating metal impurities.

Overall, as shown in Figure 5.7(c), most of the GBs of type B tend not to be recombination active after both gettering and hydrogenation, and their $S_{GB}$ values drop below the detection limit of our method, indicating that hydrogenation with a pre-gettering step is very effective in reducing their recombination strength. Such GBs are less likely to affect the final cell performance in comparison with GBs of type A. Considering that there are more type B GBs in wafers from the top and the bottom regions, their median $S_{GB}$ values after various process steps are likely to be lower than the medians of the cleaner samples, and that is consistent with our experimental results, as illustrated in Figure 5.2(b).

## 5.3.5 Sub-bandgap photoluminescence

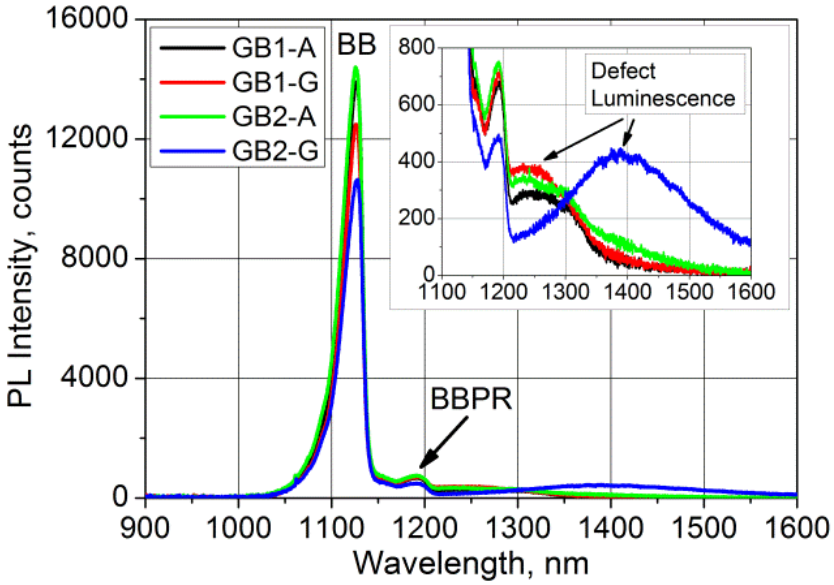


**Figure 5.8 – PL spectra of two selected GBs from middle of the ingot, as highlighted in Figure 5.1. A and G denote as-grown and gettered GBs respectively. BB and BBPR denote band-band line and the first phonon replica of the band-band line respectively.**

In addition to band-to-band PL imaging, micro-PL spectroscopy technique was also applied to measure sub-bandgap PL emitted from several selected GBs at low temperature ($79K$), using it as an additional tool to analyse GBs. It is found that for GBs from the middle of the studied ingot (W68), distinct sub-bandgap PL spectra were detected from GBs that are already active in the as-grown state and gettering activated GBs. An example performed on two selected GBs from the middle of the ingot, as highlighted in Figure 5.1, is shown in Figure 5.8. Figure 5.9 shows their corresponding injection dependent $S_{GB}$ values before and after gettering. GB1 is a Σ27 GB, while GB2 is a RA GB with misorientation angle of 33° along the axis $[342]$. GB2 is not recombination active in the as-grown state, but becomes very active after gettering, while GB1 is active even before gettering. Sub-bandgap PL around 1400 nm is only observed on GB2 after gettering, indicating the possibilities of different origins for the recombination activities in intrinsic active GBs and gettering activated GBs.

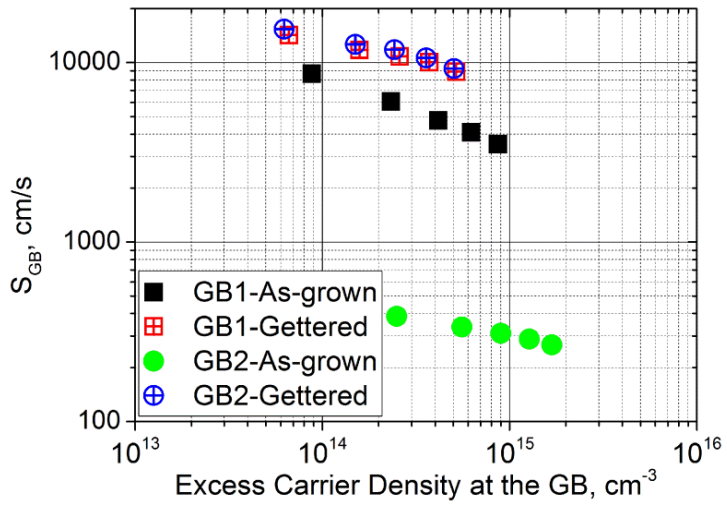


**Figure 5.9 – PL image of injection dependent $S_{GB}$ of GB1 and GB2, as highlighted in Figure 5.1, before and after gettering. Both GBs are type A GBs.**

The observed sub-bandgap PL could be related to the well-known dislocation luminescence or D-lines detected from dislocations [142-144]. Tajima *et al.* [144] studied D-lines emitted from dislocation networks or so-called small angle GBs in mc-Si materials and attributed the origin of D1/D2 lines (detected at 1530 and 1410 nm) to secondary defects or impurities trapped by the strain field around the dislocations and D3/D4 lines (detected at 1330 and 1240 nm) to the intrinsic nature of dislocations. The observed sub-bandgap PL at around 1400 nm from GB2 could be due to the certain types of impurities such as interstitial impurities or small metal precipitates that formed around the GB after gettering. These impurities could be responsible for the dramatic increase in its $S_{GB}$ value. Further studies are needed to identity the root cause for the observed sub-bandgap PL. Nevertheless, the work presented in this section highlights the possibility of using sub-bandgap PL to detect or identify certain impurities at GBs.

## 5.3.6 Limitations of the analysis

The following limitations of our analysis are noted. Firstly, the analysis presented above is solely based on a single mc-Si ingot. The results may not always be applicable to all multicrystalline silicon materials. As shown previously by Karzel *et al.* [20] and this work, the electrical properties of GBs can be strongly affected by the impurity content and the thermal history of the ingot, which can vary to a large extent depending on the ingot growth conditions. Moreover, it should be noted that instead of a standard

industrial diffusion process, we chose to use a higher deposition temperature followed by an extended anneal for our phosphorus diffusion process in order to improve the gettering effectiveness, and maximise the global lifetime after gettering, as suggested in previous studies [133, 134, 145]. The process conditions, such as the temperature and time used for the gettering or hydrogenation, could affect the results.

Secondly, all the $S_{GB}$ values shown in this work are extracted under the same photon excitation condition. The extracted $S_{GB}$ value only represents the surface recombination velocity of a GB at a particular injection level. The precise excess carrier density at the GB depends not only on their recombination properties, but also other parameters such as the generation rate, the excess carrier density of the neighbouring grains and the thickness of the sample. Therefore, even with the same generation rate, the excess carrier density at GBs can vary. Considering that some GBs exhibit strong injection dependence, comparing $S_{GB}$ values at different injection levels might yield different results, causing some uncertainty in our analysis. This uncertainty, however, is expected to be largely reduced in this work by using single-side passivated samples as the excess carrier density of the intra-grain regions in such cases is more strongly limited by the infinite surface recombination at the rear surfaces. It is certainly beneficial to compare the entire range of injection dependence of $S_{GB}$. But in reality, it is difficult to do so when comparing a large number of GBs. Moreover, from a material perspective, it might be more meaningful to compare $S_{GB}$ at a fixed excess carrier concentration. However, owing to large variation in $S_{GB}$ (from $100\ cm/s$ to $10000\ cm/s$), the carrier concentration at GB under constant generation can be very different. Being limited in practice by the maximum laser intensity and noise in the PL images at lower incident photon flux, we were not able to achieve the same excess carrier concentration for all the GBs.

Thirdly, we only evaluate recombination active GBs in this work, as our quantification method, when applied on single-side passivated samples, is not sensitive to inactive GBs ($S_{GB} \ll 100\ cm/s$). As a result, our sample group does not reflect the total population of different types of GBs in a typical mc-Si wafer. However, given that the final cell performance is more influenced by the recombination active GBs compared to the inactive ones, analysing the active GBs, which is the emphasis of this work, is

actually more relevant. Moreover, the commonly used CSL index also has its limitations as it only describes the misorientation between the neighbouring grains forming the GB, but not the exact position of the grain boundary plane. The location of the grain boundary plane can affect their electrical properties [141, 146, 147], for example, it is reported that Σ3 {110} or Σ3 {112} GBs are much more recombination active than Σ3 {111} GBs [62, 63].

Lastly, around 100 GBs are studied in detail in this work. The sample size is large enough for a statistically meaningful analysis. A larger sample size was not practical due to the fact that the method for quantifying the recombination behaviour of individual GB is somewhat time consuming.

### 5.3.7 Detrimental influence of GBs on solar devices

It is worth noting that $S_{GB}$ represents the intrinsic recombination properties of a GB. The overall impact of a GB on a solar cell depends also on other conditions such as the generation rate, the surface conditions, the intra-grain lifetime and the operating conditions. By way of demonstration, we simulate the PL intensity profile across a GB with $S_{GB}$ of $1000\ cm/s$ under four surface conditions, assuming $S_{GB}$ is injection independent. The result is shown in Figure 5.10. The total reduction in the PL intensity represents the effective influence of a GB on the neighbouring regions.

The first two simulations assume: an ideal sample without any surface recombination; and a sample with a perfectly passivated front surface and an infinite surface recombination velocity at the rear. The former represents well passivated samples that are commonly used for investigating GB behaviours. The latter is analogous to the samples studied here in this work. Comparing their PL profile, it can be seen that surface recombination reduces the overall impact of a GB as it acts as another competing recombination channel for carriers. In addition, we simulate two other conditions that are more related to a solar cell, namely: a non-perfectly passivated sample; and a passivated diffused sample. The $J_0$ for the front and rear surfaces of both samples are assumed to be $80\ fA/cm^2$, and the sheet resistance for both surfaces of the diffused sample is set to be $100\ \Omega/\square$, both of which are typical values for an industrial solar cell. The influence of the heavily doped region is simulated using the conductive

boundary approach [119], as discussed in Section 4.2.3.1. As illustrated in Figure 5.10, heavily doped regions act as conductive layers which provide additional paths for carriers to flow to the GB, hence further extending the influence of a GB across the wafer.

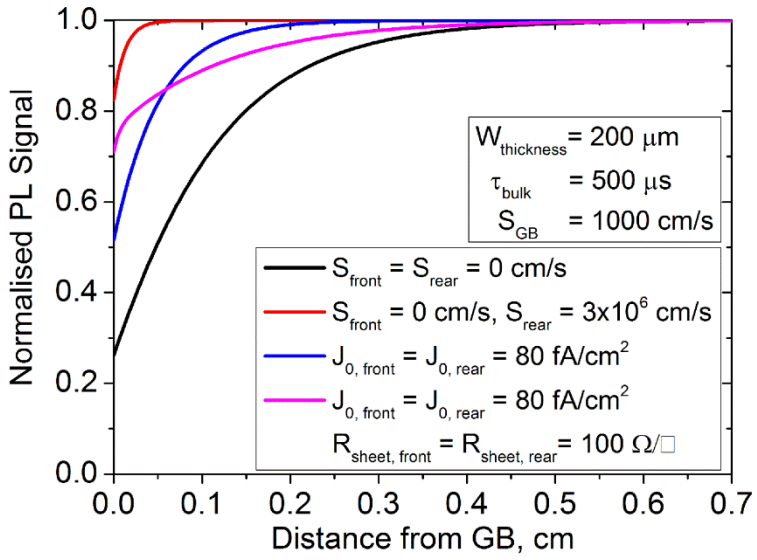


**Figure 5.10 – Simulated PL profile across a GB with $S_{GB}$ of 1000 $cm/s$ under various surface conditions. Only one side of the PL profile is shown as the PL profile is symmetrical. The bulk lifetimes of the neighbouring grains are assumed to be injection independent and are set to be 500 µ$s$. The wafers are illuminated with incident photon flux, $2.3 \times 10^{17}$ $cm^{-2}s^{-1}$, at 808 nm.**

Another example is demonstrated in Figure 5.11, comparing the PL profile across a GB with different $S_{GB}$ on an ideal sample without any surface recombination and a passivated diffused sample. For the ideal sample, the PL profile is sensitive to variations in $S_{GB}$ when $S_{GB} \ll 1000\ cm/s$ and only varies slightly once $S_{GB}$ exceeds 2000 $cm/s$. This indicates that, in the absence of diffused layers and surface recombination, the impact of a GB saturates when $S_{GB}$ reaches a certain value. This is due to the fact that the recombination rate in this situation is limited by the transport of carriers to the GB rather than its intrinsic recombination properties. In contrast, as shown in Figure 5.11(b), the PL profile for the passivated diffused sample does not converge even when $S_{GB}$ reaches $10^4$ $cm/s$ or above. This implies that the varying electrical properties among GBs are likely to have a larger impact on a solar cell compared to test structures such as well passivated and non-diffused samples that are commonly used for investigating GB behaviours.

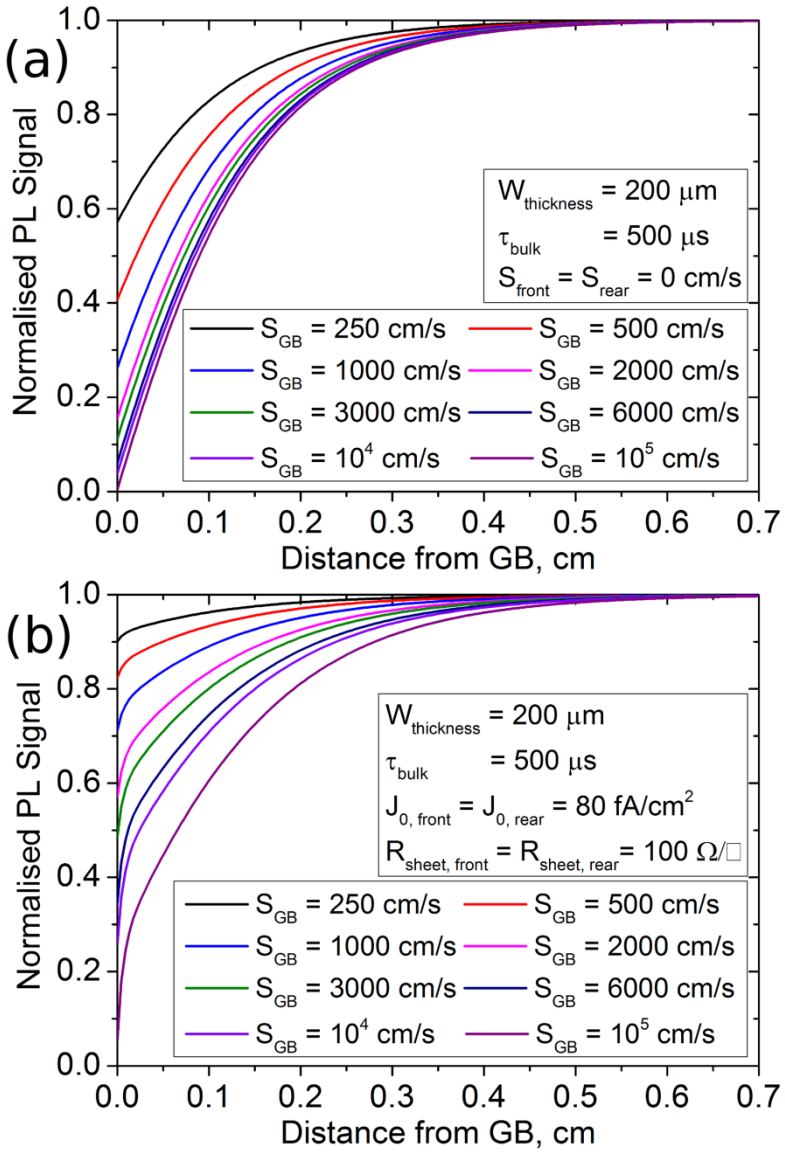


**Figure 5.11 – Sensitivity of PL profile on $S_{GB}$ for (a) an ideal sample without any surface recombination (b) a passivated diffused sample. Only one side of the PL profile is shown as the PL profile is symmetrical. The bulk lifetimes of the neighboring grains are assumed to be injection independent and are set to be 500 µs. The wafers are assumed to be illuminated with the same incident photon flux, $2.3 \times 10^{17}\ cm^{-2}s^{-1}$, at 808 nm.**

Moreover, the range of influence of GBs tends to be larger under open circuit conditions in comparison to short circuit conditions. Under open circuit conditions, carriers can flow freely from the intra-grain regions to the crystal defects either via the heavily doped regions or bulk diffusion [148, 149]. Under short circuit conditions, most of the carriers that reach the pn junction are likely to be collected at metal contacts and extracted to external circuit instead of flowing into GBs or dislocations. This is

demonstrated in Figure 5.12 which shows a two dimensional simulation, performed with Sentaurus [121], of the electron concentration around a GB with $S_{GB}$ of 1000 $cm/s$ at different operating conditions. In Figure 5.12, lateral variation in the electron concentration is due to GB recombination, whereas the vertical variation is caused by charge collection and recombination in the heavily doped regions. It can be seen that the influence of GB is at maximum at open circuit condition. Their impact reduces at maximum power point and reaches minimum at short circuit conditions in which the carrier density is strongly dominated by charge collection and emitter recombination.

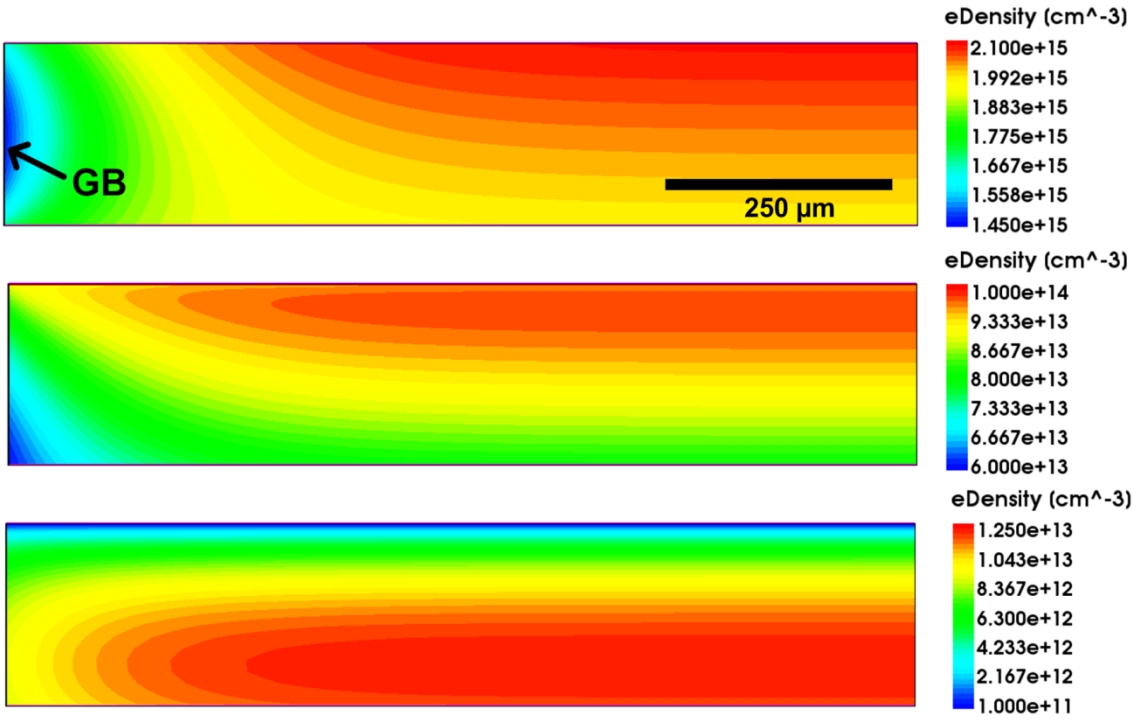


**Figure 5.12 – Electron concentration around a GB with $S_{eff}$ of 1000 $cm/s$ at (a) open circuit, (b) maximum power point and (c) short circuit condition. The bulk lifetimes of the neighbouring grains are assumed are set to be 500 $\mu s$. The samples are illuminated at approximately one sun. The $J_0$ for the front and rear surfaces are around 120 $fA/cm^2$ and 90 $fA/cm^2$ respectively. The width and thickness of the sample are set to be 1 $cm$ and 200 $\mu m$ respectively. Note the different scale for the electron concentration in each figure.**

Although the overall impact of a GB on a solar cell depends not only on the GB itself, studying the intrinsic electrical properties of a GB is still important as it may allow us to understand the origins of their recombination behaviour. Moreover, based on the extracted $S_{GB}$ value, one can also perform numerical modelling to estimate the

recombination losses induced by a GB in a solar cell under different operating conditions, and in the presence of diffusions.

## 5.4 Conclusions

Our results demonstrate that impurity levels significantly impact the electrical properties of as-grown GBs, and also their response to phosphorus gettering and hydrogenation. Gettering or hydrogenation steps alone induce a significant increase in the recombination strength of nearly all GBs near the middle of the studied ingot. We speculate this might be due to the high temperature used for the processes or the rapid quenching afterwards, which changes the form of the impurities around the GBs. The influence of gettering or hydrogenation steps alone varies on GBs in samples with higher levels of impurities. Interestingly, hydrogenation, in general, is much more effective on gettered GBs compared to as-grown GBs. A distinct difference in the injection dependence of the recombination properties of GBs is also observed. While some GBs exhibit little injection dependence before gettering, others show a rather strong injection dependence, with $S_{GB}$ increasing as the injection level decreases. The former type of GBs tend not to be recombination active after both gettering and hydrogenation, with their $S_{GB}$ values dropping below the detection limit of our method, and are thus less likely to affect the final cell performance in comparison with GBs of the latter type. Moreover, distinct sub-bandgap PL spectra were detected from GBs that are already active before gettering and gettering activated GBs, suggesting different origins for their recombination activities.

# Chapter 6

# Direct comparison of the electrical properties of various multicrystalline silicon materials for solar cells

## 6.1 Introduction

Conventionally grown p-type boron doped multicrystalline silicon has been the main stream in mc-Si solar cell production over the past decade. However, due to their lower intrinsic material quality, they are generally not suitable for high efficiency solar cells. Recent development of the crystal growth technology has led to the production of various types of mc-Si materials with great potential for high efficiency low cost solar cells. Two notable examples of such are the n-type phosphorus doped mc-Si and the seed-assisted growth high performance mc-Si.

The advantages of n-type materials over p-type materials, such as their higher tolerance to metal contaminations and the absence of boron-oxygen-related defects, have already been demonstrated on monocrystalline silicon, but are not yet widely recognised in mc-Si industry. Direct comparisons of p-type and n-type mc-Si are rare in the literature. Schindler *et al.* [150] compared the potential cell efficiency of conventionally solidified p-type and n-type mc-Si materials crystallised under the same conditions, through simulations with PC1D [151] and Sentaurus [121], based on lifetime images captured using PL after different solar cell process steps. The analysis suggests a higher material related efficiency for conventional n-type mc-Si in comparison with conventional p-type mc-Si. However, in another study, Schindler *et al.* [152, 153] applied the same analysis to high performance mc-Si, and found that both the investigated high performance p-type and n-type mc-Si wafers feature comparable diffusion lengths after phosphorus gettering. Moreover, Geerligs *et al.* [29] evaluated the effects of phosphorus gettering and hydrogenation on crystal defects in conventionally solidified p-type and n-type mc-

Si, and observed no fundamental difference between the p-type and n-type materials in terms of the recombination activities of crystal defects.

On the other hand, despite the fact that high performance mc-Si materials have already been widely adapted in mc-Si industry, detailed studies on the electrical properties of high performance mc-Si are scarce. Lan *et al.* [11] suggested that the improvement in their cell efficiency compared to conventionally solidified mc-Si solar cells, is due to the reduction of dislocation density in the material, achieved by growing mc-Si ingots with smaller grains through nucleation and grain control. The reduction of grain size should, in principle, increase the spatial density of GBs. It is still unclear why the cell performance in high performance mc-Si does not suffer from a higher GB density. Yang *et al.* [12] argued that it is due to low area percentage of GBs in mc-Si. The argument, however, falls short to explain the detrimental influence of dislocations to cell performance given that the area percentage of dislocations in mc-Si is small as well. Moreover, the detrimental impact of crystal defects is not restricted at the defects themselves, but extends to areas around the defects due to lateral carrier diffusion.

In this chapter, the recombination properties of conventionally solidified n-type mc-Si wafers and high performance p-type mc-Si wafers are directly compared with the conventional p-type mc-Si wafers studied in Chapter 5. Figure 6.1 shows PL images of the three types of mc-Si wafers studied here. Recombination active GBs appear as dark lines, whereas dislocation networks appear as dark clusters in the PL images. As illustrated in Figure 6.1, the recombination behaviour in a mc-Si wafer can be divided into three distinct regions, namely the intra-grain regions, GBs and the dislocation networks. These three distinct regions of the wafers are examined in detail in this chapter, along with their response to phosphorus gettering and hydrogenation. It is important to consider the influence of phosphorus gettering and hydrogenation when evaluating mc-Si materials as it has been shown that the electrical properties of mc-Si can change significantly after these processes [131, 150, 154, 155].

The electrical properties of intra-grain regions are assessed based on their minority carrier lifetimes and diffusion lengths, which are experimentally determined as a function of injection level from PL calibrated carrier lifetime images. The recombination activities of grain boundaries are compared quantitatively in terms of

their effective surface recombination velocities ($S_{GB}$), using the method presented in Chapter 4. Lastly, the recombination behaviour of dislocations is evaluated qualitatively based on PL images.

**(a) p mc-Si** **(b) n mc-Si**

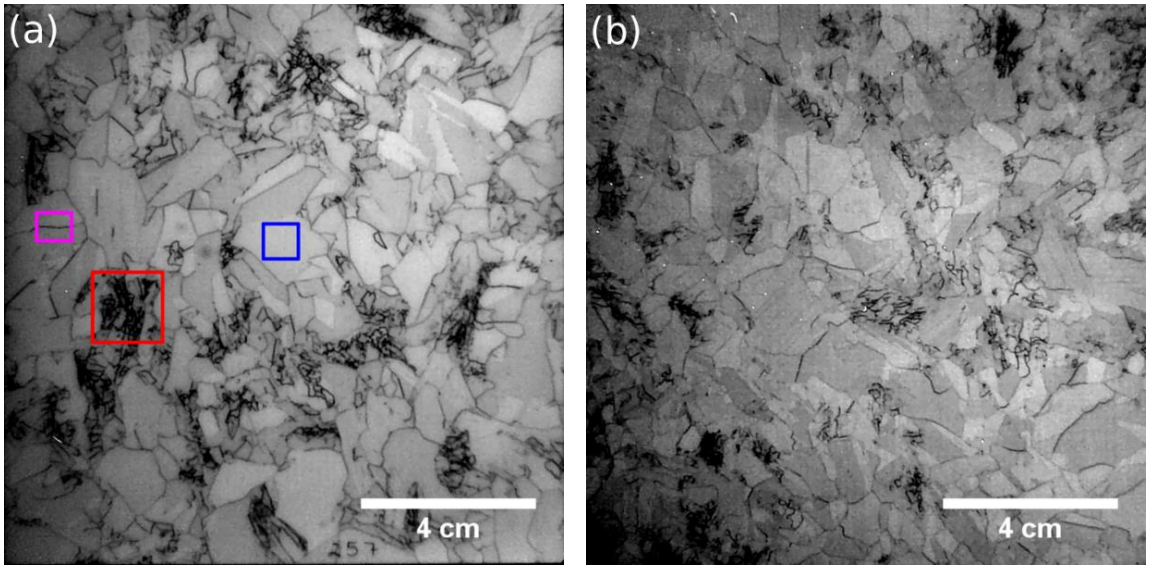


**(c) HP p mc-Si**

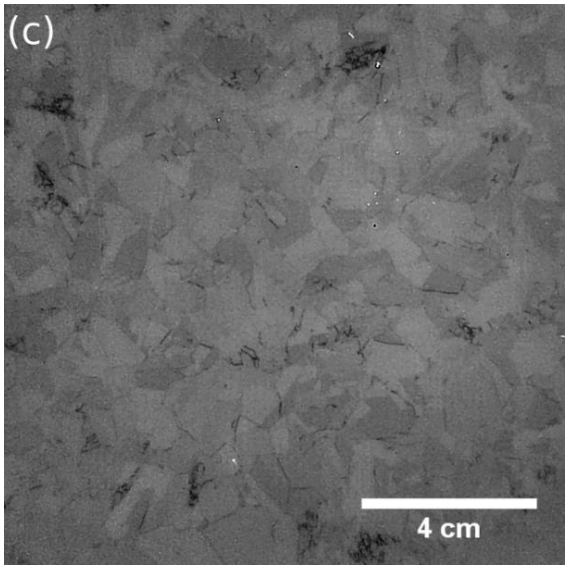


**Figure 6.1 - PL images of as-grown unpassivated mc-Si wafers from the (a) conventional p-type, (b) n-type and (c) high performance p-type mc-Si ingot studied in this work. Note that different scales were applied to the images to allow a better visual inspection of grain size, spatial distribution of GBs and dislocation networks. Examples of an intra-grain region, GB and dislocation network are highlighted in blue, magenta and red.**

# 6.2 Experimental Methods

## 6.2.1 Sample preparation

Wafers used in this work were cut from three commercially grown directionally solidified mc-Si ingots, that is, a conventional p-type boron doped ingot, a conventional n-type phosphorus doped ingot, and a high performance p-type boron doped ingot. The conventional n-type and high performance p-type mc-Si wafers were around $180\ \mu m$ and $200\ \mu m$ thick respectively and have a similar background doping of around $1.2 \times 10^{16}\ cm^{-3}$. Conventional p-type mc-Si wafers that have been studied previously in Chapter 5 are used as references for comparison. They were around $330\ \mu m$ thick with a background doping of $1.5 \times 10^{16}\ cm^{-3}$ and were cut from the middle of the ingot (denoted as W68 in Chapter 5). Wafers with similar background doping were selected in this work to avoid its potential impact on carrier lifetime, and therefore allow direct comparisons of lifetimes and diffusion lengths between the samples. Note that, in principle, the variation in wafer thickness could impact their response to gettering or hydrogenation to some extent. However, we expect such effects to be small given the long annealing time used for the phosphorus gettering, as shown below, and the high diffusivity of hydrogen at the firing temperature ($700℃$) [156].

The sample preparation procedures are the same as those used in Chapter 5. After a short chemical polishing etch using HF and $HNO_3$ acid to remove saw damage, sister wafers from each ingot were divided into two groups (A, B). Wafers from group A were phosphorus gettered. Phosphorus gettering was performed through subjecting the wafers to a 30 minute $POCl_3$ diffusion at 880℃, followed by an extended annealing in an $N_2$ ambient for more than 12 hours at 600℃ in the same diffusion furnace, resulting in sheet resistance values of around $20\ \Omega/\square$ measured using a 4-point probe. The wafers were then chemically etched to remove the phosphorus diffused layers. Afterwards, half of the sister wafers from both group A and B received silicon nitride films on both surfaces for passivation, while the other half of the wafers received silicon nitride films on the front surfaces and thin metallic aluminium films (approximately $10\ nm$) on the rear surfaces using thermal evaporation, to achieve instantaneous rear surface recombination conditions. The double-side passivated wafers were used to evaluate the

bulk lifetime of the intra-grain regions, while the single-side passivated wafers were used to investigate dislocations qualitatively and GB behaviour quantitatively, using method presented in Chapter 4.

For hydrogenation studies, all wafers had their dielectric or metallic films etched off. All samples were then re-coated with fresh silicon nitride films and were fired in a rapid thermal processing (RTP) furnace (Unitemp UTP-1100) for 3 min at 700℃ in $N_2$ ambient to produce bulk hydrogenation. After firing, all annealed silicon nitride films were removed via HF dip and the samples were re-passivated with fresh films for lifetime measurements. All samples were chemically etched to remove around 3 $\mu m$ of silicon using HF and $HNO_3$ acid after each removal of the surface films, to remove any surface defects which may have formed during the firing or film deposition. The deposited silicon nitride films in this work were around 85 nm thick and were deposited with a Roth & Rau AK400 plasma enhanced chemical vapour deposition (PECVD) system with deposition temperatures between 250℃ and 300℃.

## 6.2.2 Characterisation methods

In this work, we choose to compare both the minority carrier lifetime and diffusion length of the intra-grain regions, to allow a more meaningful comparison between the p-type and n-type wafers. The lifetimes of intra-grain regions and their injection dependence were extracted from a series of calibrated PL lifetime images captured at different laser intensities, on the double-side passivated samples, measured in areas far away from crystal defects, after applying carrier de-smearing technique [84] described in Section 2.2.2.3.

Single-side passivated samples were used for evaluating dislocations. This is because dislocations tend to form closely packed loops or networks in mc-Si wafers. The influence of multiple dislocations overlaps with each other and they appear as dark clusters in the PL images of well passivated samples, making it difficult to isolate their influence and analyse their properties. As mentioned in Section 4.4.2, the significant shorter effective minority carrier diffusion lengths in single-side passivated samples reduce the effect of carrier smearing and hence allow closely packed dislocation networks to be studied more accurately.

# 6.3 Results

## 6.3.1 Intra-grain regions

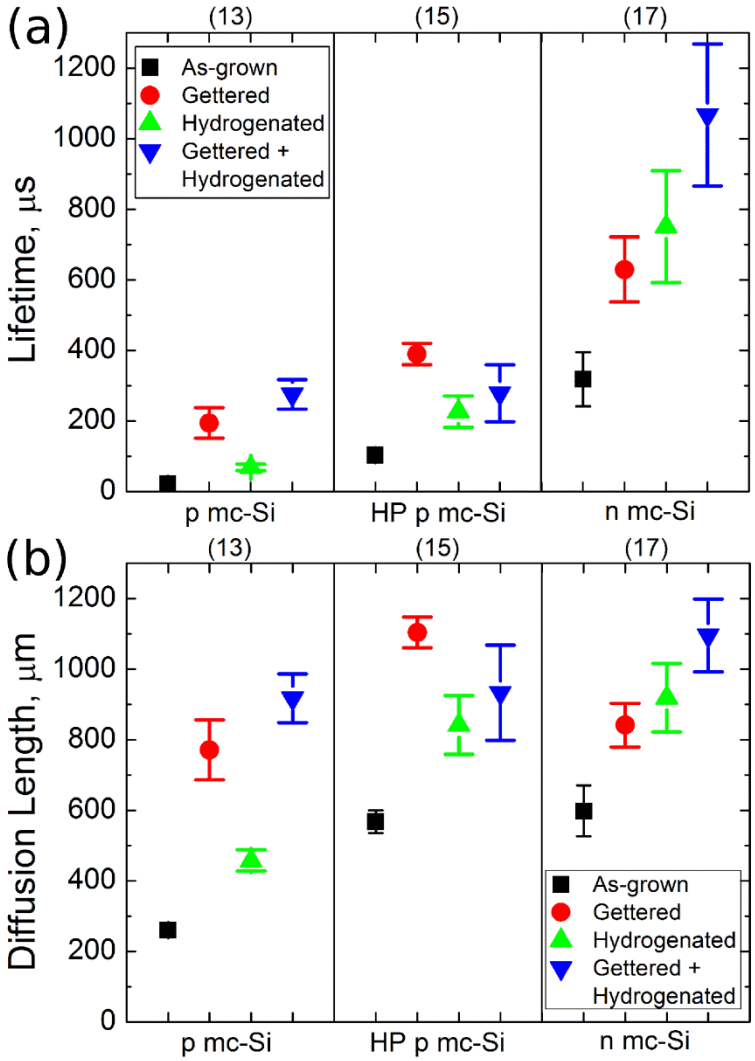


**Figure 6.2 - (a) average $\tau_{bulk}$ and (b) minority carrier diffusion length, of several intra-grain regions from the studied conventional p-type (p mc-Si), n-type (n mc-Si) and high performance p-type (HP p mc-Si) mc-Si wafers at an injection level equivalent to approximately 0.1 suns. The error bars denote one standard deviation of the data. The total numbers of sampled intra-grain regions are shown above the y-axis.**

Figure 6.2 compares the minority carrier lifetimes and diffusion lengths of intra-grain regions in the conventional p-type, n-type and high performance p-type mc-Si wafers at approximately 0.1 sun conditions, which corresponds to an injection level close to maximum power in a working solar cell [157]. The voltage of a solar cell is determined

by the product of the free carrier densities at the edge of depletion region in the base, which in turn depends directly on the minority carrier lifetime. It is observed from Figure 6.2(a) that the average intra-grain lifetime of the conventional n-type material, both before and after the different processes, is significantly higher than the p-type materials. This agrees with literatures [150, 152, 154, 158, 159] that n-type mc-Si tend to feature higher lifetime than p-type mc-Si, mainly due to their higher tolerance to metal impurity contaminations. It is also noted that, although the average as-grown intra-grain lifetime of the conventional p-type samples is considerably lower than the high performance p-type samples, the difference is diminished after phosphorus gettering and hydrogenation. This demonstrates that gettering and hydrogenation are in fact very effective in removing and passivating as-grown impurities in lower quality p-type mc-Si wafers. The results here imply that, among the intra-grain regions, the n-type material is more likely to yield a higher voltage at maximum power than the p-type materials, and both the conventional and high performance p-type materials would perform similarly, assuming other parameters affecting the device voltage remain the same.

Interestingly, while hydrogenation alone is not very effective on p-type materials, it largely improves the intra-grain lifetime in the n-type samples. The underlying mechanism of hydrogenation is not fully understood yet. The observed behaviour could potentially be related to the charge state of hydrogen. Most of the monatomic hydrogen is positively charged during the high temperature process [160], hence they might be more attractive to negatively charged impurities which are detrimental in n-type materials due to columbic attraction, improving the effectiveness of hydrogenation.

In addition to minority carrier lifetimes, their diffusion lengths are also compared. The current output of a solar cell is partly determined by the number of minority carriers that diffuse to the collecting junction before recombining, and hence is affected directly by the minority carrier diffusion length, rather than the carrier lifetime. Comparing Figure 6.2(a) and (b), it can be seen that the lifetime advantage of n-type material is largely offset by its significantly lower minority carrier mobility, resulting in a similar minority carrier diffusion length. After phosphorus gettering and hydrogenation, the average diffusion length of the intra-grain regions in the n-type samples is only marginally

higher than the other two p-type samples. Furthermore, the diffusion lengths of all three samples are at least four times higher than the thickness of a typical modern solar cell (around 200 $\mu m$). In such cases its influence on the obtainable short circuit current saturates as the vast majority of the generated carriers in the base can diffuse to the junction. Under this condition, the current output of a solar cell is dominated by its optical properties and surface recombination. This suggests that the three different materials studied here are likely to have similar performance in terms of current output from the intra-grain regions (ignoring the influence of nearby GBs and dislocations).

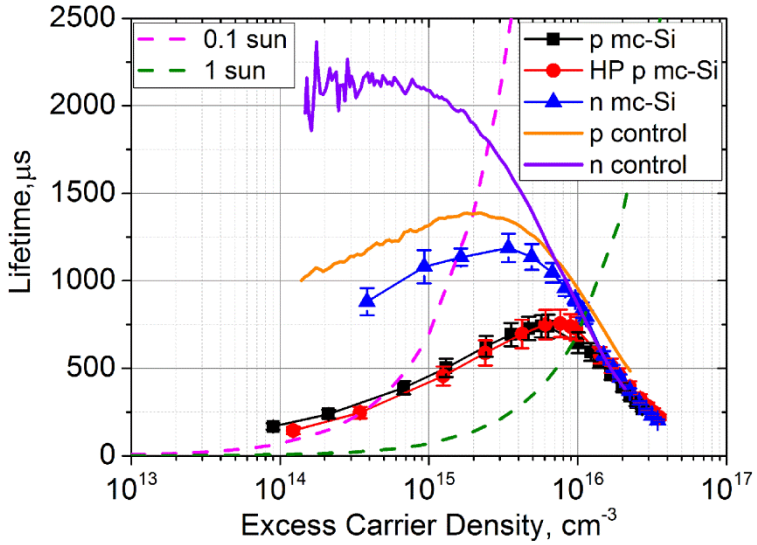


**Figure 6.3 - Injection dependent lifetime of intra-grain regions in the conventional p-type (p mc-Si), n-type (n mc-Si) and high performance p-type (HP p mc-Si) mc-Si wafers after both gettering and hydrogenation. Plotted also are the injection dependent lifetime of monocrystalline control samples with a similar background doping to our mc-Si samples. The lines of constant generation rate at approximately 0.1 sun and 1 sun are also plotted.**

Figure 6.3 shows the injection dependent lifetimes of one of the studied intra-grain regions in each type of the mc-Si wafer after both gettering and hydrogenation. It can be seen that while there is no significant difference in terms of the intra-grain lifetime between the three mc-Si materials at 1 sun condition, a substantial variation is observed at 0.1 sun condition. The lifetimes of the p-type samples are subject to a strong injection dependence and have a considerably lower lifetimes at low injection levels compared to the n-type sample. This is likely due to the fact that many of the dominant impurities in mc-Si, such as interstitial iron, act as donor levels [19] and have a larger electron capture cross-section than hole capture cross-section, hence such impurities have a more

detrimental influence in p-type materials than n-type materials at low injection levels, as described in Section 2.1.3.

The lifetime measurement performed at 1 sun condition reflects the solar cell performance at open circuit, whereas the measurement at 0.1 sun condition corresponds to operating conditions close to the maximum power point, and is therefore more relevant for a working device. The injection dependence of the lifetime, particularly the reduction of lifetime between open circuit and maximum power conditions, leads to a reduction of the fill factor in a solar cell [161]. Our results indicate that the p-type materials are likely to suffer a lower fill factor than the n-type material.

Note that although all samples have been passivated with silicon nitride, the extracted lifetimes could still be affected by surface recombination. Here, we also plotted the injection dependent lifetime of passivated monocrystalline control wafers which have a similar background doping to our mc-Si samples to demonstrate the quality of surface passivation and to verify that the extracted lifetime values at 0.1 sun are not strongly surface limited.

## 6.3.2 Grain Boundaries

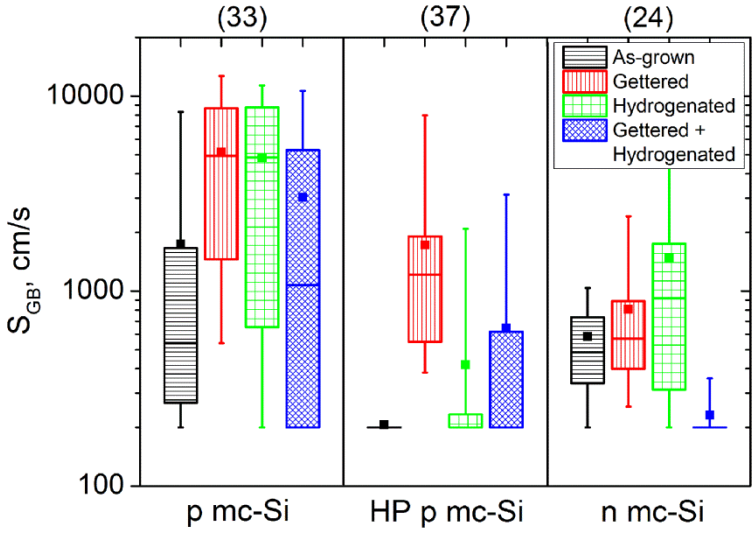


**Figure 6.4 - $S_{GB}$ of various GBs from the conventional p-type (p mc-Si), n-type (n mc-Si) and high performance p-type (HP mc-Si) mc-Si wafers before and after gettering and hydrogenation. The median values, as well as 25 and 75 percentiles are marked by horizontal bars, the means by squares. The total numbers of sampled GBs are shown above the y-axis. The value of $200\ cm/s$ is the lower detection limit of the PL imaging based measurement technique used.**

Figure 6.4 compares $S_{GB}$ of GBs from the three groups of samples before and after gettering and hydrogenation. It can be seen that the median $S_{GB}$ value of GBs from the conventional p-type samples after gettering and hydrogenation are considerably higher than the high performance p-type and conventional n-type samples. The higher recombination activities of GBs in the conventional p-type samples are unlikely to be related to the types of GBs, as it is expected that most of the sampled GBs in this work are random angle (RA) GBs. This is because most of the GBs of other types such as Σ3 or Σ9 GBs tend not to be very recombination active [5] and our quantification method is not sensitive to inactive GBs ($S_{GB} \ll 200\ cm/s$). This is confirmed by Electron Backscatter Diffraction (EBSD) measurements, which indicate that around 75% of the sampled GBs in the conventional p-type samples are RA GBs.

The lower recombination activities of GBs in high performance mc-Si could contribute to the improvement in its cell performance in comparison with conventional p-type mc-Si solar cells, considering that there is little variation in their lifetime in the intra-grain region, as described above. This could also be one of the reasons that a reduction in cell performance for high performance mc-Si is not observable in reality even though they contain a higher density of GBs, as a result of smaller grain size. Note that GBs in conventional p-type, high performance p-type and conventional n-type samples exhibit distinctive behaviours in response to the various process steps.

The influence of gettering and hydrogenation on GBs is evaluated through inspecting the response of individual GBs to each process. The results are summarised in Figure 6.5. Our results show that phosphorus gettering increases the recombination strength of all the GBs in the p-type wafers and most of the GBs in the n-type wafers. We suggest that it is due to the high temperature applied during the process or the rapid quenching afterward that causes a redistribution of impurities near the GBs [136, 139], as explained previously in Section 5.3.1.

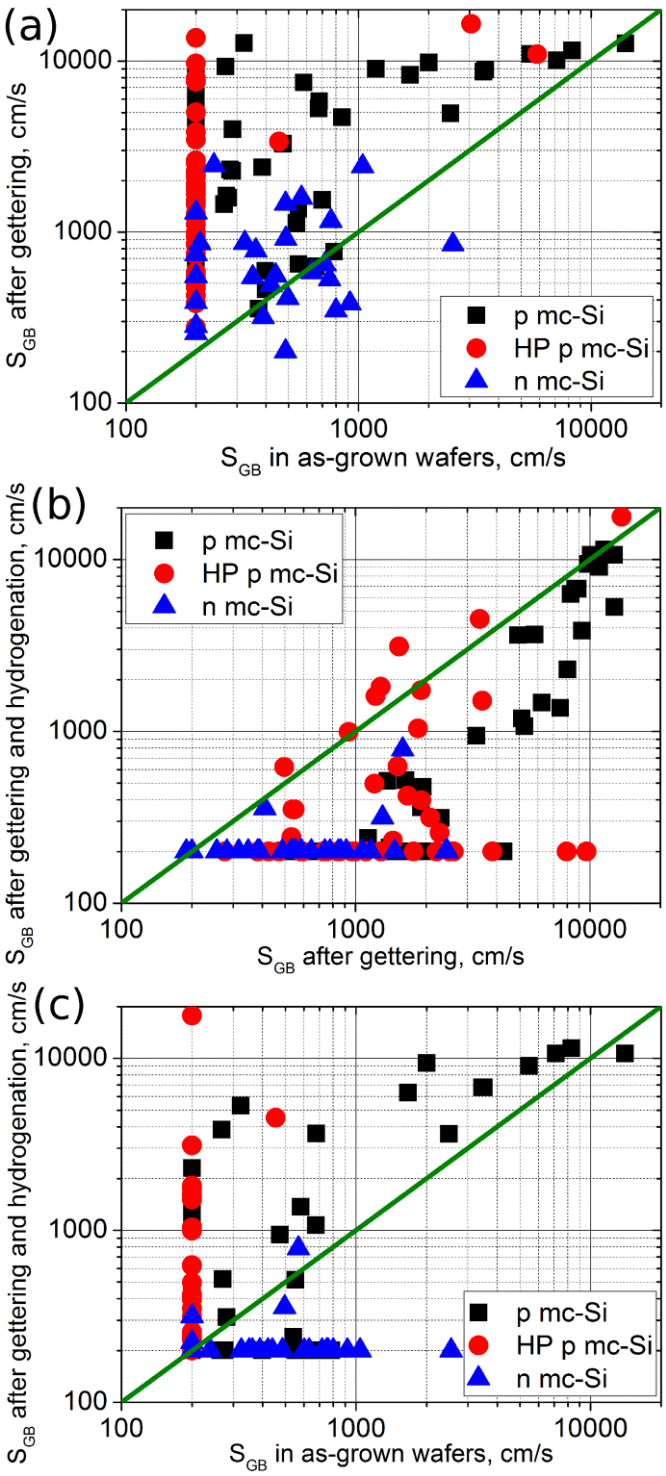


**Figure 6.5 - (a) The influence of phosphorus gettering on as-grown GBs. (b) The influence of hydrogenation on gettered GBs. (c) The net influence of gettering and hydrogenation on as-grown GBs. The diagonal line represents no change after processing. Data points above this line correspond to GBs with an increase of $S_{GB}$ after processes, and vice versa. The value of 200 $cm/s$ is the lower detection limit of the PL imaging based measurement technique used. Note that some data points in the figure overlap with each other, as some of the GBs have the same $S_{GB}$.**

In contrast, hydrogenation reduces the recombination strength of all the gettered GBs. Although the benefits of hydrogenation are clear, as shown in Figure 6.5(b), it appears that the effectiveness of hydrogen passivation strongly varies among different materials, as demonstrated in Figure 6.5(c), which shows that the net influence of phosphorus gettering and hydrogenation varies largely for the three sets of samples.

As-grown GBs in high performance p-type samples tend not to be recombination active and they become more active after both gettering and hydrogenation. On the other hand, GBs in n-type samples show a completely opposite response. They are recombination active in the as-grown state, but show a dramatic reduction in their recombination strength after gettering and hydrogenation, with their $S_{GB}$ values dropping below the detection limit of our method. Combining Figure 6.5(a) and (c), it can be seen that the benefits of hydrogenation outweigh the detrimental effect of gettering for the studied n-type samples, and vice versa for the high performance p-type samples. This echoes the observation above in Section 6.3.1, suggesting that hydrogenation is more effective on n-type mc-Si than p-type mc-Si. GBs from the conventional p-type samples have a more varied response. Some of the GBs become more recombination active, whereas others become less active. This varied response could be attributed to variation in the GB geometry or type, which can have an impact on the ability to aggregate metal impurities [22, 27, 141], as discussed as Section 5.3.3.

It should be mentioned that our finding, however, is contradictory to the results of Geerligs *et al.* [29], who observed little difference in the recombination activity of crystal defects between n-type and p-type mc-Si. It is noted that in general the electrical properties of crystal defects can be strongly affected by the impurity content and the thermal history of the ingot, which can vary to a large extent depending on the casting conditions. The process conditions, such as the temperature used for the gettering or hydrogenation, can also affect the results.

## 6.3.3 Dislocations

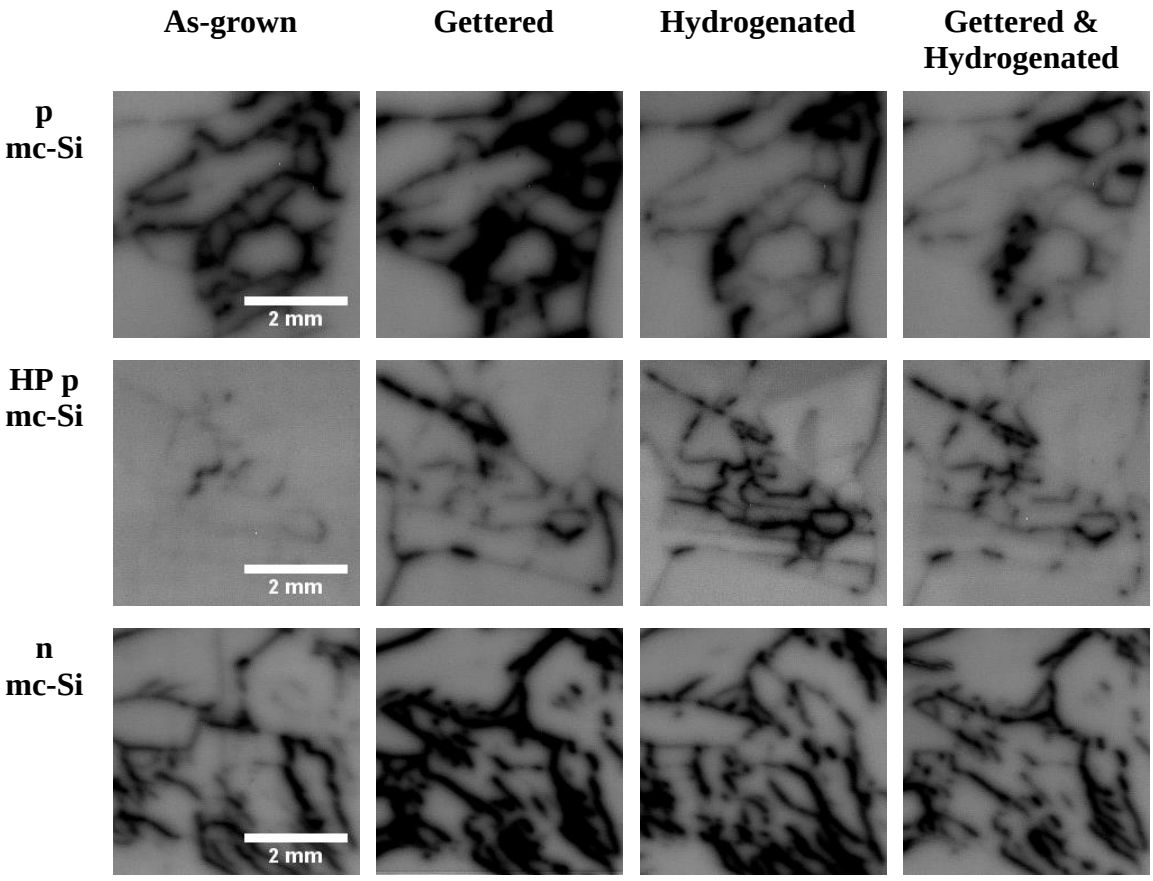


**Figure 6.6 - PL images of dislocation clusters in conventional p-type (p mc-Si), high performance p-type (HP p mc-Si) and conventional n-type (n mc-Si) samples. The individual PL images are normalised against the PL intensity of an intra-grain region far away from the dislocations. The same scale is applied in all the images.**

As mentioned above, dislocations tend to form small and closely packed loops in mc-Si. Limited by the spatial resolution of our PL images, we could not apply our method used in investigating GBs to evaluate the $S_{eff}$ of dislocations. Here, we assess the recombination properties of dislocations qualitatively based on PL images of single-side passivated wafers. Although only qualitative, this gives a picture of the recombination behaviour of dislocations before and after gettering and hydrogenation. The results are summarised in Figure 6.6. The recombination behaviour of dislocations in conventional p-type and n-type samples is qualitatively similar. Most of them are already recombination active in the as-grown state before any processing. Gettering further increases their recombination strength. Hydrogenation neutralises part of the changes

induced by gettering, and in some cases can even reduce the recombination activity to levels lower than those present in the as-grown state.

Comparing dislocations in conventional p-type and n-type samples, it can be seen that the advantage of the high immunity to metal impurities in n-type material, as evident in the high intra-grain lifetimes shown above, does not apply at dislocations, indicating the possibility that crystal defects such as dislocations might have different origins of their recombination activities in comparison to intra-grain regions. This is supported by the study of Buonassisi *et al.* [136], who observed that nanoprecipitates containing elements with higher atomic flux such as copper and nickel are mainly found at structural defects, whereby particles of low-flux species such as titanium often appear within the intra-grain regions.

Surprisingly, dislocations in high performance mc-Si exhibit a distinct behaviour. Similar to GBs in high performance mc-Si, as-grown dislocations are not recombination active and only become active after either gettering or hydrogenation. Note also that, as illustrated from Figure 6.1, the high performance mc-Si sample contains a much lower density of dislocation clusters compared to the two conventionally grown mc-Si wafers. Thus, they do not suffer as much recombination loss from dislocations as the conventional p-type and n-type mc-Si samples.

### 6.3.4 Activation of crystal defects in high performance mc-Si during annealing and phosphorus gettering

One of the features observed in this work is that crystal defects in the studied high performance mc-Si, including GBs and dislocations, are not recombination active, or only slightly active before any thermal processes, but become active after either gettering or hydrogenation. In order to determine the cause of this behaviour, an annealing experiment is performed. Figure 6.7 shows PL images of a set of high performance mc-Si wafers that were annealed at various temperatures for 30 minutes in an $N_2$ ambient. Samples in Figure 6.7(b) and (c) were air cooled to room temperature after the anneal, whereas the sample in Figure 6.7(d) was slowly cooled from 700℃ to 400℃ with a cooling rate of around 10℃ – 15℃ per 15 minutes and air cooled to room temperature afterward. Being limited by the equipment used, slow cooling from 700℃

to room temperature could not be performed. The variation in the PL intensity among different grains in Figure 6.7(a) and (d) is due to an orientation dependent surface passivation effect, which will be discussed in detail in Chapter 7. Note that the samples in these PL images are unpassivated, and hence the images are only valid for qualitative comparisons.

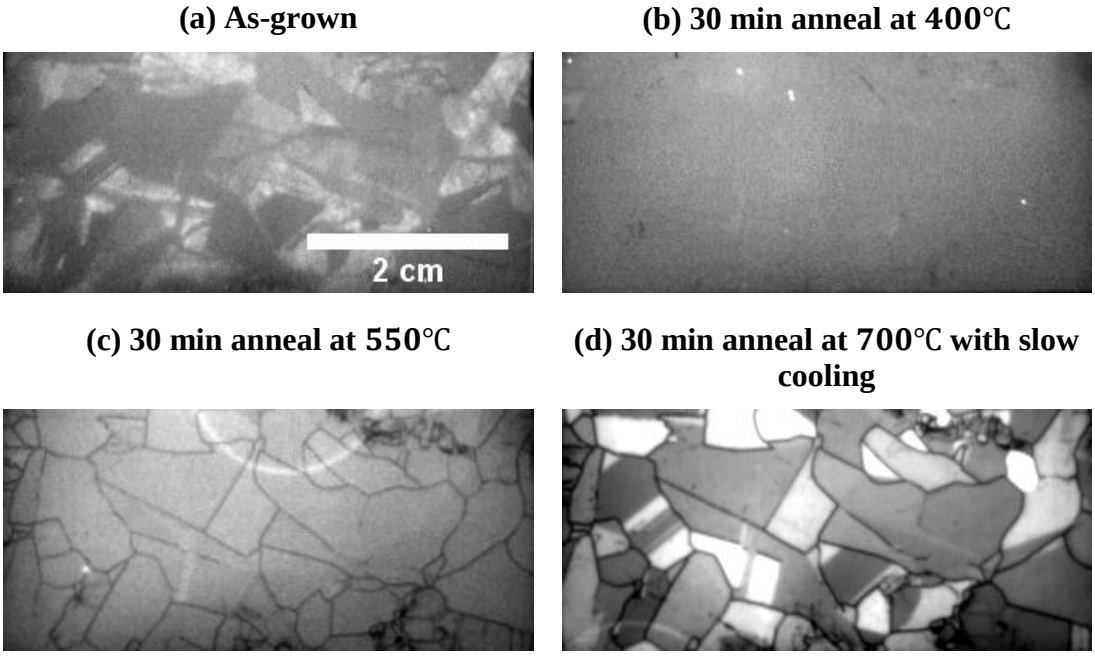


**Figure 6.7 - PL images of unpassivated high performance p-type mc-Si wafers before and after annealing at various temperatures for 30 minutes. The contrast in each image was adjusted using 50% and 150% of the average PL intensity as the minimum and maximum thresholds. The bright ring appearing in (c) is the inductive coil equipped in the PL imager for the QSSPC lifetime measurement (not used here). Note that the images were captured with standard lens which has a very different pixel size compared to Figure 6.6, in which the images were captured with a high magnification lens.**

From Figure 6.7, it can be seen that the crystal defects are quite stable below 400℃. The activation of crystal defects occurs between 400℃ and 550℃. Even with a slow cooling rate, the activation of crystal defects cannot be avoided, as shown in Figure 6.7(d). This indicates that rather than the quenching rate, the anneal temperature is more likely to be the key parameter affecting the recombination properties of crystal defects in the studied high performance mc-Si ingot.

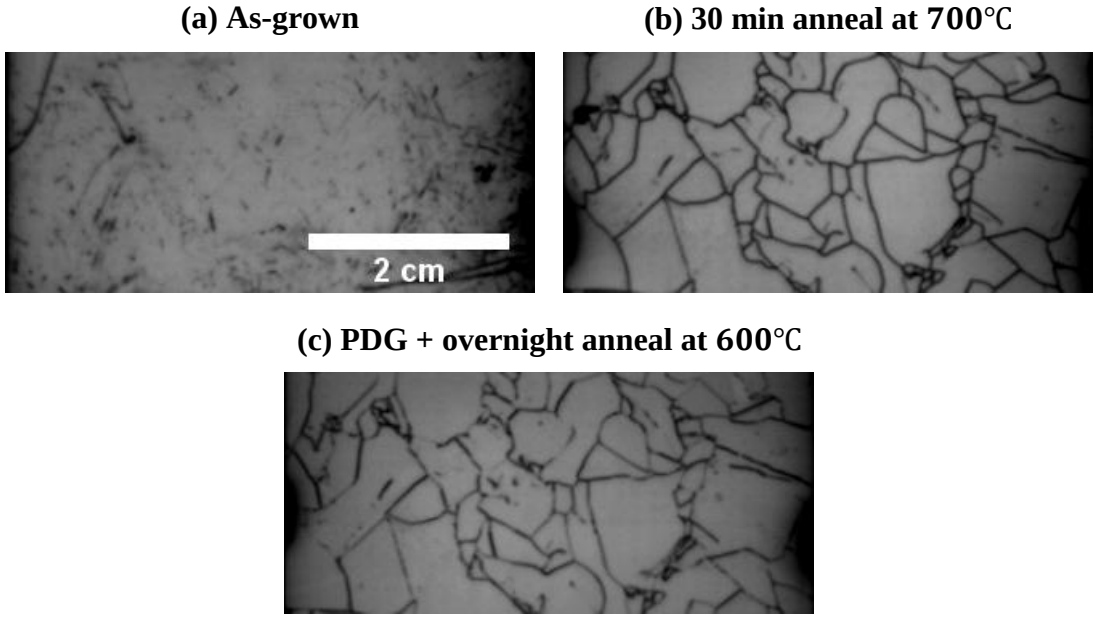


**Figure 6.8 - PL images of single-side passivated high performance p-type mc-Si wafers before and after annealing and phosphorus diffusion gettering (PDG). Phosphorus gettering was performed using recipe described in Section 6.2.1. Both samples in (b) and (c) were air cooled to room temperature after the processes. The contrast in each image was adjusted using 50% and 150% of the PL intensity of an intra-grain region in the image as the minimum and maximum threshold.**

Here, we also compare the effect of thermal annealing to phosphorus gettering. Figure 6.8 shows PL images of another set of high performance mc-Si samples before and after thermal annealing and phosphorus gettering. Note that in contrast to those in Figure 6.7, single-side passivated samples were used to allow a direct comparison of the recombination activities of crystal defects. As shown in Figure 6.8, crystal defects in the wafers were activated by either thermal annealing or gettering. Comparing Figure 6.8(b) and (c), it seems that grain boundaries or dislocations after thermal annealing are more recombination active than those after gettering. This might suggest that a portion of the metal impurities around crystal defects could in fact be gettered by the phosphorus diffused layers, though the benefit of this effect is overshadowed by the redistribution of metal impurities as a result of the high temperature used in the process, as discussed in Section 5.3.1, leading to an overall increase in their recombination behaviour.

## 6.3.5 Impact on device parameters

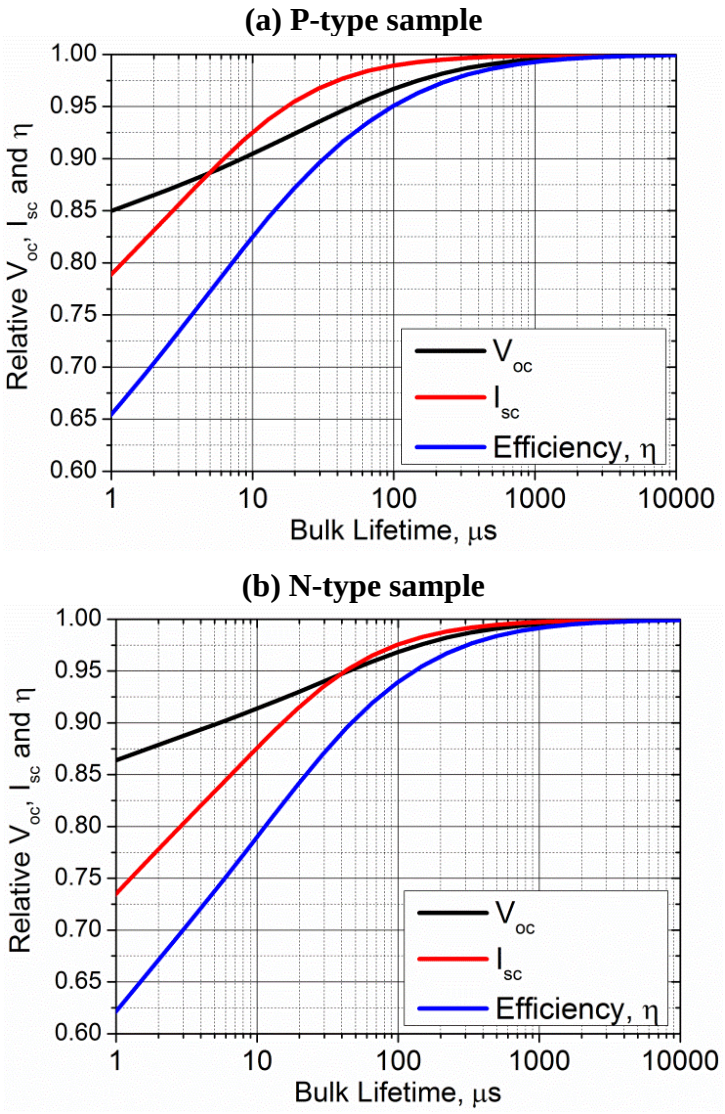


**Figure 6.9 - Simulation dependence of $V_{oc}$, $I_{SC}$ and η (scaled to the maximum achievable values) on the material bulk lifetime for (a) p-type sample (b) n-type sample. The $J_0$ for the front and rear surfaces are assumed to be 80 $fA/cm^2$ each. For the p-type sample, the maximum achievable $V_{oc}$, $I_{SC}$ and η that is used for scaling are 683 $mV$, 41.3 $mA/cm^2$ and 23.8% respectively. For n-type sample, the maximum achievable $V_{oc}$, $I_{SC}$ and η are 684 $mV$, 41.0 $mA/cm^2$ and 23.7% respectively. The slight variation in the maximum achievable efficiency for p-type and n-type samples is due to the difference in their carrier mobility, when coupled with surface recombination in the heavily doped regions.**

A simulation using QS Cell [85] is performed to model the dependence of $V_{oc}$, $I_{SC}$ and η on the material bulk lifetime for p-type and n-type samples. As shown in Figure 6.9, the solar cell efficiency starts to saturate when the bulk lifetime reaches a certain value

(around $200 - 300\ \mu s$). The solar cell efficiency in such cases is more limited by other factors such as the optical properties or surface recombination. As shown previously, the average lifetimes of the intra-grain regions for all three mc-Si samples after gettering and hydrogenation are at least above $200\ \mu s$, suggesting that the performance limiting factors in the three materials studied here are indeed recombination at GBs and dislocations.

Recombination active GBs and dislocations lead to a local reduction of lifetime and excess carrier concentration at the defects, resulting in a local reduction of both the open circuit voltage and the short circuit current, as demonstrated in Figure 6.9. The local fill factor may also be lower as some crystal defects exhibit strong injection dependence, being more recombination active at lower injection levels, as observed in Section 5.3.4 and also in Ref. [26] and [126]. Apart from the defects themselves, areas adjacent to the defects are also affected by the defects due to lateral carrier diffusion. The spatial extent of these effects depends not only on the intrinsic recombination properties of the defects, but also on other factors such as the surface conditions, the carrier diffusion length and the device operating conditions, as discussed in Section 5.3.7.

The behaviour of a complete mc-Si device is rather complex. In addition to the factors discussed above, other factors such as the density of crystal defects and their spatial distribution can all affect the performance of a large area mc-Si solar cell. Dislocation networks tend to be concentrated locally within several grains, whereas GBs are more equally distributed across the wafers. 2D or 3D modelling is required to properly simulate a mc-Si device [148-150, 162], such modelling, however, is beyond the scope of this work. The emphasis of this work is to obtain a better understanding of the electrical behaviour in various types of mc-Si materials before and after gettering and hydrogenation. The work can be used as a reference to determine the key performance limiting factors in mc-Si solar cells and develop methods to improve their efficiency.

## 6.4 Conclusions

A direct comparison of the electrical properties of conventional p-type, n-type and high performance p-type mc-Si materials is performed in this chapter. It is found that the intra-grain lifetimes of the n-type samples can reach $1\ ms$ or above and are

considerably higher than the two p-type materials studied here. Nevertheless, among the intra-grain regions, all samples reveal high diffusion lengths ($> 800\ \mu m$) after gettering and hydrogenation, indicating that the main performance limiting factors in mc-Si are likely to be recombination at crystal defects.

GBs in conventional p-type samples are more recombination active than those in high performance p-type and conventional n-type samples. Phosphorus gettering increases the recombination strength of most of the GBs. Hydrogenation is most effective on gettered n-type samples, being able to neutralise the influence of gettering and in fact deactivate most of the GBs. Hydrogenation, however, can only offset part of the increase in $S_{GB}$ induced by gettering in p-type samples. In terms of dislocations, the recombination behaviour of dislocations in conventional p-type and n-type samples is qualitatively similar, being already very recombination active in the as-grown state and becoming even worse after gettering. Their recombination strength reduces after hydrogenation, but does not disappear completely. Similar to GBs, as-grown dislocations in high performance mc-Si samples are not recombination active and they only become active after gettering or hydrogenation. Annealing experiments reveal that the activation of crystal defects in the studied high performance mc-Si occurs between $400℃$ and $550℃$ and such activation is more likely to be related to the high temperature used in the process rather than the rapid quenching afterward.

Overall, among the three materials studied in this work, it is expected that both the conventional n-type and the high performance p-type mc-Si samples would outperform the conventional p-type mc-Si sample. The main advantage of the n-type mc-Si material is its superior electrical properties in the intra-grain regions and GBs, especially after both gettering and hydrogenation. The benefit of the high performance p-type mc-Si material is that it contains significantly fewer dislocation networks. Combining the advantages of both of these materials in a high performance n-type mc-Si ingot may prove to be the ideal mc-Si material for high efficiency low cost solar cells, due to its anticipated properties of high intra-grain lifetimes, relatively inactive GBs, and reduced frequency of dislocation networks.

# Chapter 7
# The Influence of Crystal Orientation on Surface Recombination in Multicrystalline Silicon

## 7.1 Introduction

Apart from recombination through crystal defects within the bulk, recombination at surfaces acts as another significant loss mechanism in solar cells. Surface passivation is important in solar cell manufacturing as it reduces surface recombination, and thus improves the overall cell performance. Surface passivation is commonly achieved by depositing or growing dielectric films on silicon surfaces. Effective surface recombination velocities ($S_{eff}$) below 10 cm/s on undiffused crystalline silicon wafers with a range of resistivity have been widely reported with different passivation methods in the literature [163-166].

Since the surfaces of an actual solar cell are usually textured to reduce its reflectance and enhance light trapping, surface passivation is typically applied to textured surfaces rather than planar surfaces. Such textured surfaces contain crystalline facets with orientations different from the untextured planar orientation. For example, random pyramid textured surfaces contain (111) orientated facets as a result of the associated alkaline etching used. It has been reported that the passivation effectiveness for certain dielectric films, such as silicon dioxide [33, 167], amorphous silicon [34, 35] and aluminium oxide [168, 169] can indeed be influenced by surface orientation, whereas some other films such as silicon nitride [33, 170] are unaffected. Baker-Finch and McIntosh [33] compared the passivation effectiveness on (100) and (111) wafers and observed the recombination rate at hydrogenated $SiO_2$-passivated planar (111) surfaces to be four times higher compared to equivalent (100) surfaces, while a similar level of

passivation was observed on planar (100) and planar (111) wafers passivated by silicon nitride, both before and after hydrogenation. Liang *et al.* [168] compared the recombination current density ($J_o$) on boron-diffused (111) and (100) wafers passivated by aluminum oxide films deposited through atomic layer deposition (ALD) and reported that the recombination current of (111) samples is higher than (100) samples.

The majority of previous studies on dielectric passivation focussed on monocrystalline silicon and were, therefore, usually limited to (100), (111) and (110) orientated wafers. The effectiveness of surface passivation in mc-Si material is more complex due to the random crystal orientation in mc-Si, and the fact that commercial mc-Si solar cells are usually textured in an acidic, isotopic etchant, resulting in the formation of hemispherically shaped bowl-like structures on the surfaces [171] which contain a continuous range of crystal orientations. Surface passivation studies on mc-Si wafers are rare in the literature. The main challenges are the lack of a suitable technique to evaluate surface recombination in mc-Si wafers, and the fact that measuring crystal orientation in mc-Si wafers often requires time consuming techniques. This chapter addresses these two concerns, applying PL imaging technique to explore surface recombination in silicon wafers.

The chapter begins with applying PL imaging to thin and chemically polished mc-Si wafers, in which the formation of a very thin native oxide on the surfaces provides a crystal orientation dependent passivation effect. An approach for monitoring crystal orientations in mc-Si wafers based on this correlation is proposed. Measurement of crystal orientation is usually performed through X-Ray diffraction or Electron Microscopy techniques such as X-ray Diffraction Topography (XRT) and Electron Backscatter Diffraction (EBSD) [56], as discussed in Section 2.2.3. Although these methods allow very accurate measurements or mapping of crystal orientation, they are time consuming and can usually only be applied to a small area. Several other methods for determining grain orientations in large area mc-Si wafers have been proposed recently [172-175]. Wang *et al.* [174] and Lausch *et al.* [175] demonstrated the possibility of measuring grain orientations in mc-Si wafers based on reflectometry and optical microscopy using anisotropically etched wafers. The approach proposed in this

chapter provides the basis for a simple and fast method to determine the mixture of grain orientations in large area mc-Si wafers based on chemically polished wafers.

In the second part, the chapter presents two approaches for evaluating the influence of crystal orientation on surface passivation using PL imaging. The methods allow a variety of orientations, not limited to (100), (110) and (111) planes, to be studied. The first approach is based on imaging carrier lifetimes among different grains in mc-Si wafers, making use of their random distribution of crystal orientations. The second approach is based on imaging carrier lifetimes in silicon strips containing different surface orientations, created from a single monocrystalline silicon wafer via laser cutting. For demonstration, both approaches are applied to investigate the orientation dependent passivation effect of thermally grown silicon oxide films. The advantages and limitations for both approaches are discussed and compared.

# 7.2 Imaging crystal orientations in mc-Si wafers via photoluminescence

## 7.2.1 Experimental Methods

### 7.2.1.1 Method description

The effective lifetime of any semiconductor may be written as,

$$\frac{1}{\tau_{eff}} = \frac{1}{\tau_b} + \frac{1}{\tau_s} \qquad (7.1)$$

Where $\tau_b$, and $\tau_s$ represent the bulk lifetime and surface lifetime respectively. Since the PL intensity is proportional to the effective lifetime, as shown in Section 3.1, the PL intensity $I_{PL}$ can be expressed as:

$$I_{PL} \propto \tau_b \qquad for\ \tau_s \gg \tau_b \qquad (7.2)$$

$$I_{PL} \propto \tau_s \qquad for\ \tau_b \gg \tau_s \qquad (7.3)$$

Hence, the PL intensity is proportional to the bulk lifetime in sufficiently well passivated wafers [176-178]. By contrast, in an unpassivated wafer, provided that the bulk lifetime is much higher than surface lifetime (satisfying equation 7.3), the PL intensity reflects the surface recombination velocity of each grain in a mc-Si wafer, which in turn depends on their crystal orientations. Different crystal orientations can have different surface recombination velocities due to variations in surface structure, such as the density of dangling bonds, and their interactions with surface passivating films, such as deposited films, or even a native oxide [178, 179]. In an as-cut wafer, the contrast between grains is significantly reduced due to the fact that the deep saw damage limits the differences in the intrinsic surface properties and the effectiveness of surface passivation, causing a very high and almost identical surface recombination velocity on all grains. Polished samples allow for the removal of this deep saw damage, and avoid optical effects caused by changes in reflectance in different grains, as opposed to alkaline etched samples that often exhibit varying degrees of texturing on different orientations, which can impact on the PL emission properties. The relatively undamaged polished surface then permits the native oxide to provide some level of passivation, while still ensuring that the effective lifetime is surface limited. This provides suitable conditions for observing variations in crystal orientations.

#### 7.2.1.2 Sample preparation

The samples used here were p-type boron doped mc-Si wafers which came from 25% (W25), 50% (W50) and 75% (W75) from the bottom of a commercially grown directionally solidified mc-Si ingot. While the majority of the data was obtained using the W50 wafer, wafers W25 and W75 were used to test the validity of this approach when using wafers with different doping and bulk lifetimes. Each wafer was diced into smaller pieces, then each piece was polished through chemical etching using HF and $HNO_3$ in a ratio of 1:8 for more than 6 minutes with agitation until a mirror-like surface was achieved. All wafers were dipped in HF solution after etching to remove any residual acid-grown oxide on their surfaces. The thickness of the wafers reduced from 180 µm in the as-cut state to around 115 µm after the polishing. PL images of each wafer were captured a few days after the polishing to allow enough time for the passivation effect of residual HF to vanish.

### 7.2.1.3 Characterisation method

The crystal orientation of selected grains was measured and mapped by EBSD, taken with a Zeiss UltraPlus analytical FESEM, with details described in Section 2.2.3. The PL intensity of each grain is correlated with the crystal orientation through its corresponding surface energy. The surface energy can be interpreted as the excess energy at a surface compared with the bulk caused by the breaking of atomic bonds at the surface. It is strongly influenced by the density of dangling bonds, which affects the $S_{eff}$, and it also reflects the difficulty of saturating dangling bonds, which affects passivation effectiveness. Here, the surface energy ($E_s$) of each surface orientation was determined based on first-principles [180, 181],

$$E_s = \frac{(E_T - NE_b)}{2A} \qquad (7.4)$$

Where $E_b$ and $E_T$ correspond to the bulk energy of the silicon lattice and the total energy of an N-layer slab constructed according to each orientation. $A$ is the surface area of the slab. Both bulk and slab energy were modelled using GULP [182] in Materials Studio modelling software.

**Table 7.1 – Surface energy comparison between modelling results and literature values**

| **Orientation** | **Surface Energy ($J/m^2$)** | | | |
|---|---|---|---|---|
| | **Modelled** | **Jaccodine [183]** | **Lu *et al.* [180]** | **Stekolnikov *et al.* [184, 185]** |
| **(100)** | **2.26** | **2.13** | **2.37** | **2.39** |
| **(111)** | **1.19** | **1.23** | **1.99** | **1.74** |
| **(113)** | **1.95** | | **1.82** | **1.85** |
| **(110)** | **1.51** | **1.51** | **1.75** | **1.7** |

Table 7.1 compares the modelling result of several selected orientations with results from the literature. The modelling result agrees well with Jaccodine [183], but there is some discrepancy in the surface energy of the (111) orientation between our result and results from Lu *et al.* [180] and Stekolnikov *et al.* [184, 185]. Despite this, the modelled

surface energies are sufficient to be used as a quantitative measure to represent crystal orientation, and hence to demonstrate a definite correlation exists between the PL intensity on mirror polished samples and the surface orientation.

## 7.2.2 Results

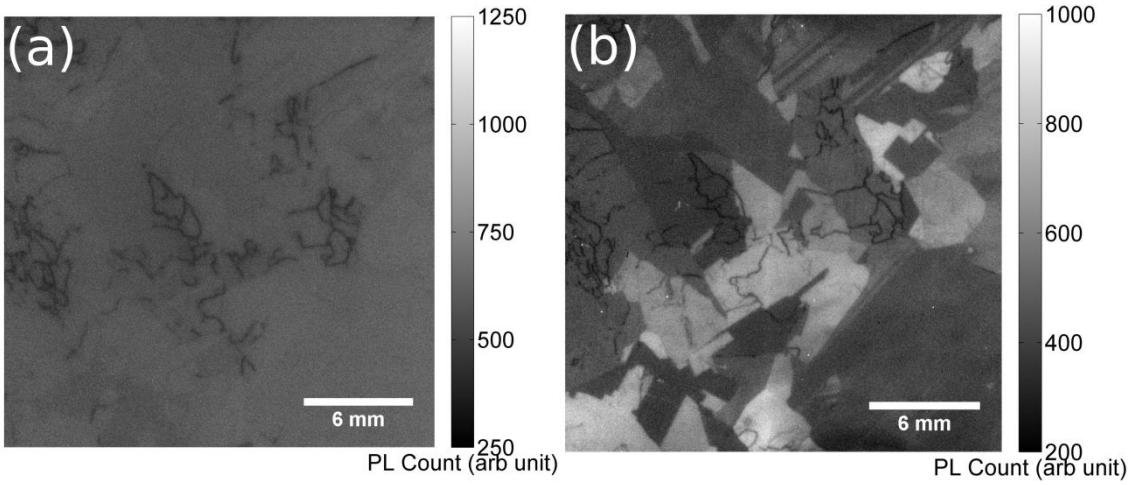


**Figure 7.1 - PL images of (a) as-cut (b) mirror polished wafer. The scale range is centred around the mean in the images, while the maxima and minima are adjusted to retain a constant contrast ratio.**

Figure 7.1 shows PL images of an as-cut wafer and a mirror polished sister wafer. The scale range is centred around the mean in both images, while the maxima and minima are adjusted to retain a constant contrast ratio. This allows a direct comparison of the differences in contrast of the PL signal among different grains. Note that the average PL intensity is reduced in Figure 7.1(b) due to the reduction in thickness. No obvious difference of the PL signal among different grains can be observed in the as-cut wafer, as shown in Figure 7.1(a), while a significant contrast among different grains is observed in the mirror polished wafer, as shown in Figure 7.1(b). The result indicates the fact that different crystal orientations have different surface recombination velocities, which are reflected in the PL intensity. Variations of the reflectivity of different grains at 808 nm (the laser excitation wavelength) in the mirror polished wafers were measured to be less than 2% using a spectrophotometer, confirming that the optical properties from grain to grain have no detectible impact on the PL emission.

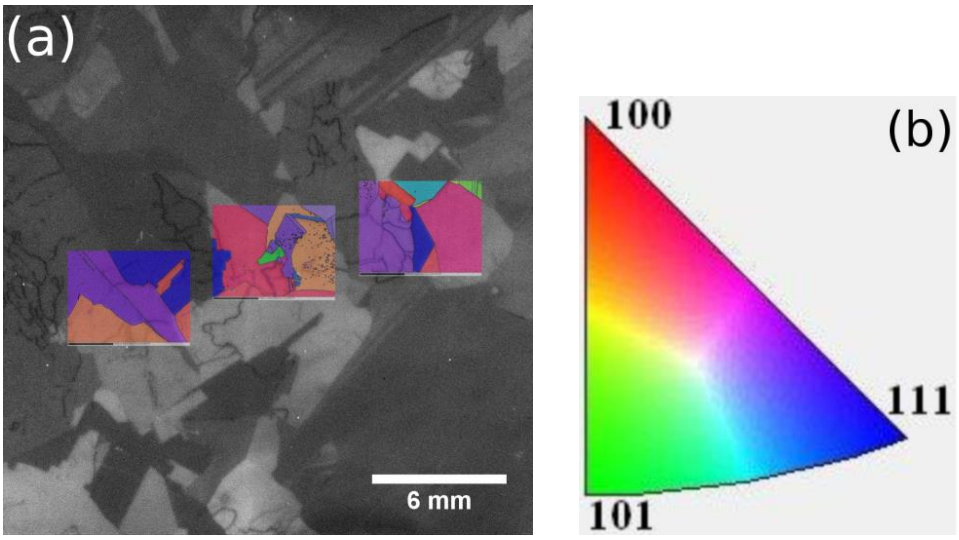


**Figure 7.2 - (a) PL image overlayed with surface orientation. (b) Colour coded Inverse Pole Figure (IPF): represents each surface orientation with a specific colour.**

Figure 7.2 shows the surface orientation maps, acquired by EBSD, overlayed on the PL image from Figure 7.1(b). Selected grains in Figure 7.2(a) are highlighted with different colours according to their surface orientations, in accordance with the Inverse Pole Figure (IPF) shown in Figure 7.2(b). It can be observed that grains with an orientation close to (100) have a higher PL intensity while crystals close to (111) have a lower PL signal.

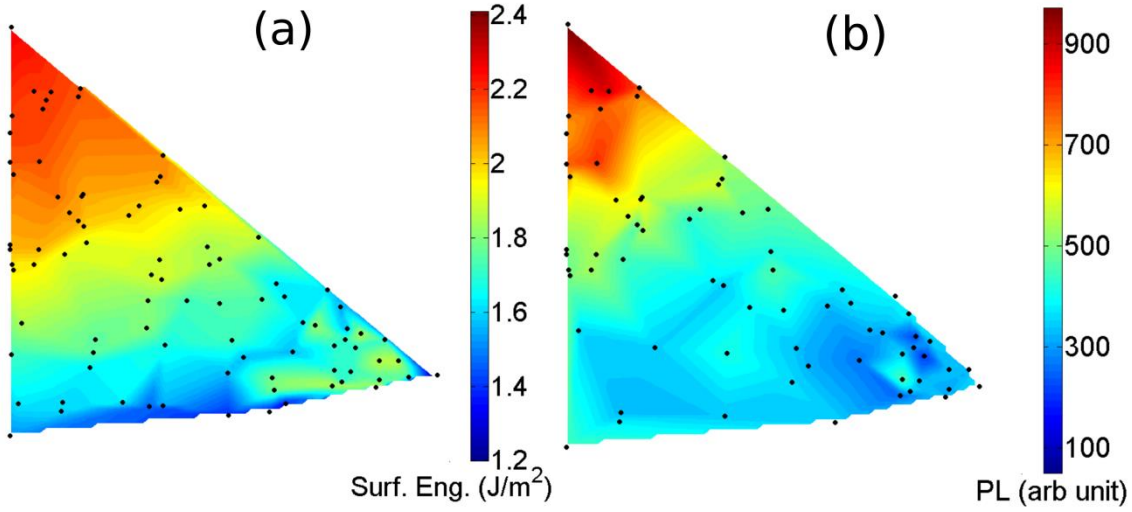


**Figure 7.3 - Interpolated result of (a) surface energy $(J/m^2)$ (b) PL count of each orientation plotted in an Inverse Pole Figure (IPF) based on measured grains, represented by dark dots.**

Based on the crystal orientation of the detected grains and their corresponding locations in an Inverse Pole Figure, we interpolated the surface energy and the PL intensity of various crystal orientations in an IPF using the modelled surface energies and measured PL counts. The result is shown in Figure 7.3. Figure 7.3(a) generally agrees with Figure 7.3(b), indicating that orientations with a high surface energy show a higher PL signal.

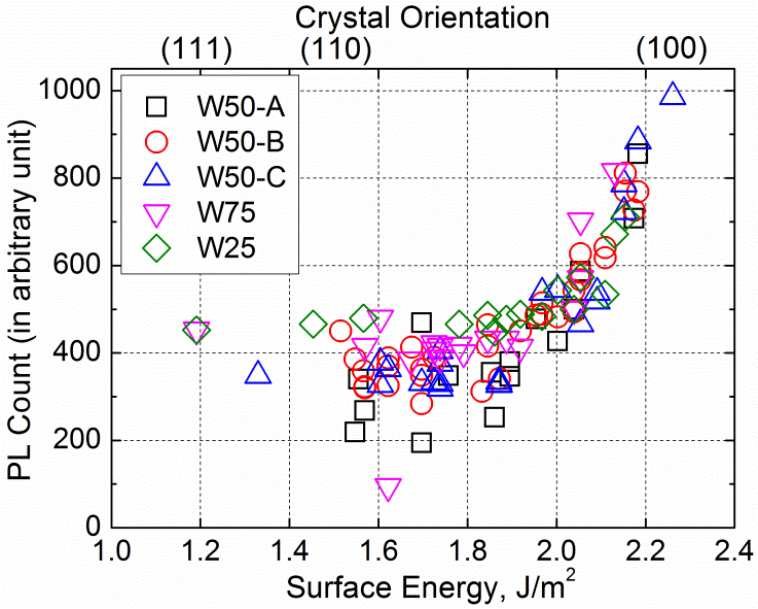


**Figure 7.4 - PL intensity of each detected grain as a function of surface energy.**

Figure 7.4 compares the measured PL intensity of each grain and its corresponding surface energy. W50-A, W50-B and W50-C corresponds to 3 wafers diced from W50. W75 and W25 are wafers from 75% and 25% from the bottom of the ingot. Due to the slight differences in thickness, doping, roughness and optical properties in the studied samples, the PL intensity of each grain is normalised using the measured PL intensity of a certain grain in the samples together with the PL intensity of a similarly orientated grain in W50-A.

A strong correlation exists between the PL intensity and the surface energy for all the wafers including wafers from different parts of an ingot. This reveals the possibility to estimate crystal orientations using PL images based on this correlation. While it is difficult to derive an absolute correlation between PL and surface orientation due to the influence of wafer thickness and surface conditions on the measured PL, this method may be useful in estimating mixes of crystal orientations in the border regions of cast

monocrystalline like silicon wafers [186], for example, in which the orientation of the large central grain is known, and the corresponding PL intensity can be used for normalisation. Alternatively, in a mc-Si wafer with a large enough number of random grains, the brightest grains can be assumed to be close to (100) orientation.

## 7.3 Characterising the influence of crystal orientation on surface passivation in silicon wafers

The work presented in the previous section highlights the possibilities of using PL imaging technique to evaluate surface recombination in silicon wafers. In this section, the technique is extended to characterise the influence of crystal orientation on dielectric passivation. Two approaches are presented. For demonstration, the approaches are applied to investigate the orientation dependent passivation effect of thermally grown silicon oxide films, although in principle the methods can also be applied to other passivating films.

### 7.3.1 Method I: Imaging carrier lifetimes in mc-Si wafers

#### 7.3.1.1 Method description and sample preparation

The first approach is based on imaging carrier lifetimes among different grains in mc-Si wafers, making use of their random distribution of crystal orientations. Wafers used in this section were n-type phosphorus doped mc-Si wafers with a background doping of around $1.2 \times 10^{16}\ cm^{-3}$. N-type mc-Si wafers were chosen due to their high bulk lifetime compared to p-type mc-Si wafers, which increases the sensitivity of the method. After initial chemical etching to remove saw damage, the wafers were phosphorus gettered and hydrogenated to further improve their bulk lifetime. Phosphorus gettering was performed by subjecting the wafers to a 30 minute $POCl_3$ diffusion at 880℃, followed by an extended annealing in an $N_2$ ambient for more than 12 hours at 600℃ in the same diffusion furnace. Hydrogenation was achieved by coating the samples with PECVD silicon nitride films and firing them in a rapid thermal processing (RTP) furnace (Unitemp UTP-1100) for 3 min at 700℃ in $N_2$ ambient. After gettering and hydrogenation, the surface films and diffused layers were removed via HF dip and chemical etching.

Before oxidation, the samples were mirror polished using HF and $HNO_3$ in a ratio of 1:8, to avoid any variation in surface topology from grain to grain which may have an impact on the passivation, as well as the reflectance and PL emission properties. The

thickness of the mc-Si wafers was reduced from 180 μ$m$ in the as-cut state to around 130 μ$m$ after etching. The wafers were then subjected to a thermal oxidation at 860℃ for 70 minutes, followed by a 3 hour nitrogen anneal at the same temperature and a forming gas anneal at 400℃ for 30 minutes afterward, to grow silicon oxide films on their front and rear surfaces. Instead of a more typical oxidation process, this lower oxidation temperature was used to avoid bulk degradation in the mc-Si wafers. The nitrogen and forming gas anneals afterward were used to improve the passivation quality of the silicon oxide films.

The thickness of the silicon oxide films was measured to be around 22 nm on a (110) orientated control sample, using an ellipsometer. Note that the oxidation rate varies on surfaces with different orientations and was found to decrease in order of $R_{(111)} > R_{(110)} > R_{(100)}$ [187]. A variation in the oxide thickness from around 15 $nm$ for the (100) surfaces to around 25 $nm$ for the (111) surfaces is expected. This range of variation in the oxide thickness is unlikely to impact the passivation quality, confirmed by the fact that the highest lifetime was in fact observed from (100) surfaces, with the thinnest oxide, as shown below. The study by Baker-Finch and McIntosh [33] also demonstrated that the passivation quality of silicon oxide is independent of oxide thickness after forming gas anneal. We chose to grow silicon oxide films of this thickness range to ensure the oxide is thick enough even on a (100) surface to achieve passivation, but still thin enough that there is negligible variation in the reflectance among different grains, which could impact the extracted lifetime values from PL images.

The method presented here relies on imaging carrier lifetimes in various grains within a mc-Si wafer. As discussed previously in Section 2.2.2.3, carrier smearing within the sample obscures the measurement of the intra-grain lifetime, and hence can significantly reduce the accuracy of the method. Therefore, a carrier de-smearing technique (Section 2.2.2.3) was applied to all the acquired PL images to correct for the influence of lateral carrier smearing within the sample and thus to allow more accurate extraction of the intra-grain lifetime. The carrier de-smearing technique is crucial for the presented method.

### 7.3.1.2 Extraction of the surface recombination velocity ($S_{eff}$)

For samples with uniform carrier density profile depth-wise, the surface recombination velocity ($S_{eff}$) can be related to the bulk lifetime ($\tau_b$) and the effective lifetime ($\tau_{eff}$) according to [55]:

$$\frac{1}{\tau_{eff}(\Delta n)} = \frac{1}{\tau_b(\Delta n)} + \frac{2S_{eff}(\Delta n)}{W} \qquad (7.5)$$

Where W is the sample thickness.

The effective lifetime is the directly measurable parameter in equation 7.5. The extraction of $S_{eff}$ from the effective lifetime measurement requires information about the bulk lifetime, which is generally difficult to determine in mc-Si wafers. Thus, a (100) float-zone (FZ) wafer of similar resistivity, which received the same passivation as the mc-Si sample, is used as a control wafer to determine the bulk lifetime of the mc-Si wafers. The $S_{eff}$ of the FZ control wafer is calculated, as a function of excess carrier density, through subtracting the bulk lifetime, assumed to be Auger limited [44], from the measured injection dependent effective time, according to equation 7.5. The Auger limit assumption in effect yields an upper bound for the $S_{eff}$. A (100) grain in the mc-Si sample is then assumed to have the same $S_{eff}$ as the control wafer, and together with the effective lifetime measurement of that particular (100) grain in the mc-Si sample, the injection dependent bulk lifetime of that (100) grain can then be determined. By assuming the bulk lifetime is uniform among various grains in a mc-Si wafer, the $S_{eff}$ of each grain can be calculated from equation 7.5, which may then be correlated with the grain orientations.

Note that the bulk lifetime among different grains in a mc-Si wafer may indeed be different. This could contribute to uncertainty in the extracted $S_{eff}$ values. This uncertainty is expected to be small as long as the rate of surface recombination is much higher than bulk recombination. In this work, such a surface limited condition is achieved by using gettered and hydrogenated n-type mc-Si wafers with high intra-grain bulk lifetime (above 700 $\mu s$ measured after passivating with silicon nitride), combined

with the fact that the studied silicon oxide films only provide moderate passivation. However, this could be a potential problem when applying the method to study dielectric films that provide very good passivation effect ($S_{eff} \ll 10\ cm/s$), such as aluminium oxide, silicon nitride or other silicon oxides, in which the varying impact of the bulk lifetime is comparable to that of $S_{eff}$ among various grains.

The sensitivity limit of the method depends on the bulk lifetime and the thickness of the mc-Si wafers used. When applied on 130 μ$m$ thick wafers with bulk lifetime varying from 500 μ$s$ to 1 $ms$ between grains, an error of up to 16% is estimated in the extracted $S_{eff}$ for a dielectric film with $S_{eff}$ of 40 $cm/s$. Using thinner mc-Si wafers with higher bulk lifetime can further enhance the sensitivity of the method. For example, using 120 μ$m$ thick wafers with bulk lifetime varying from 1 $ms$ to 2 $ms$ between grains can limit the error in the extracted $S_{eff}$ to 15% or below for films with $S_{eff}$ of 20 $cm/s$ or higher.

### 7.3.1.3 Results

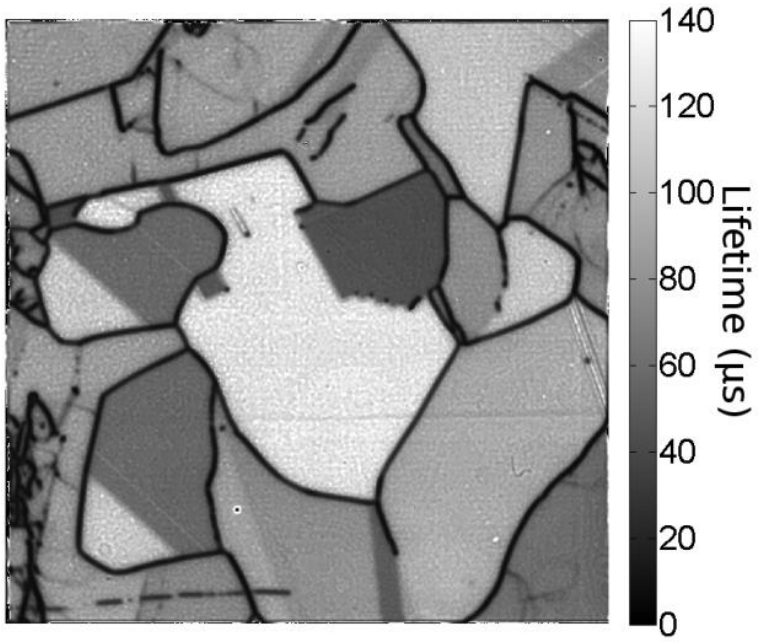


**Figure 7.5 - PL calibrated lifetime images after applying the carrier de-smearing technique. The image was taken with an incident photon flux of $2.7 \times 10^{18}\ cm^{-2}s^{-1}$.**

Figure 7.5 shows a PL calibrated lifetime image of a silicon oxide passivated mc-Si wafer studied in this work after applying the carrier de-smearing technique. A strong

contrast can be observed among different grains. The contrast is similar to one observed on mirror polished and unpassivated mc-Si wafers shown in Section 7.2, which is attributed to the orientation dependent passivation effect of a very thin native oxide formed on their surfaces.

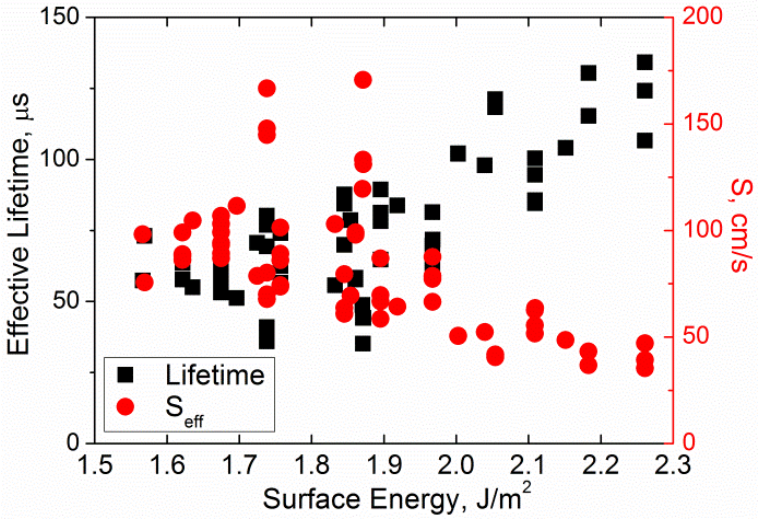


**Figure 7.6 - The effective lifetimes and surface recombination velocities of individual grains in the studied mc-Si wafers classified according to their corresponding surface energies.**

Figure 7.6 compares the surface energies of selected gains (modelled according to equation 7.4 based on their crystal orientations measured with EBSD) and their corresponding lifetimes and $S_{eff}$ (measured at an excess carrier density of $1 \times 10^{15}\ cm^{-3}$). As discussed in Section 7.2.1.3, the surface energy gives an indication of the surface structure such as the density of dangling bonds. It can be seen that there is a strong correlation between the surface energy of each grain and its corresponding $S_{eff}$ value, suggesting that the contrasts observed in Figure 7.5(b) are indeed due to the orientation dependence of the passivation. Orientations with a higher surface energy show a lower $S_{eff}$ value, and vice versa. Note that there is some scatter in the data, possibly due to factors such as thickness variation across the mc-Si wafer as a result of the extended acidic etching used, uncertainty in the modelling of the surface energies or some impact of bulk lifetime variations from grain to grain.

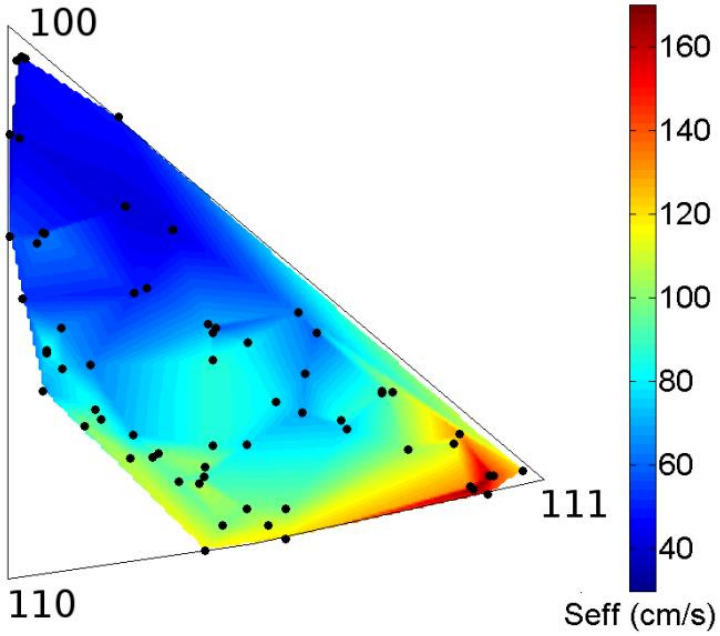


**Figure 7.7 - Interpolated result of the surface recombination velocity of each orientation plotted in an Inverse Pole Figure (IPF) based on measured grains, represented by dark dots.**

Owing to the simplicity of this method, a large number of grains/orientations can be studied with this approach. A total of 66 grains were analysed in this work. Based on these 66 grains, we interpolated the surface recombination velocities of various crystal orientations in an Inverse Pole Figure (IPF) for the studied silicon oxide films. The results are shown in Figure 7.7. It can be observed that the passivation quality of the studied silicon oxide is best for surfaces close to (100) orientation and its effectiveness reduces gradually as the orientation moves towards the (111) plane. This is in agreement with previous studies [33] which observed that the passivation effectiveness of silicon oxide on a (100) surface is considerably higher than those on a (111) surface. The observed behavior could be related to the defect density at the interface. Arnold *et al.* [188] observed a dependence of surface state density on crystal orientation on thermally oxidized single-crystal silicon. Note that no grain at or close to (110) orientation was detected among the analysed grains.

## 7.3.2 Method II: Imaging carrier lifetimes in silicon strips

### 7.3.2.1 Method description and sample preparation

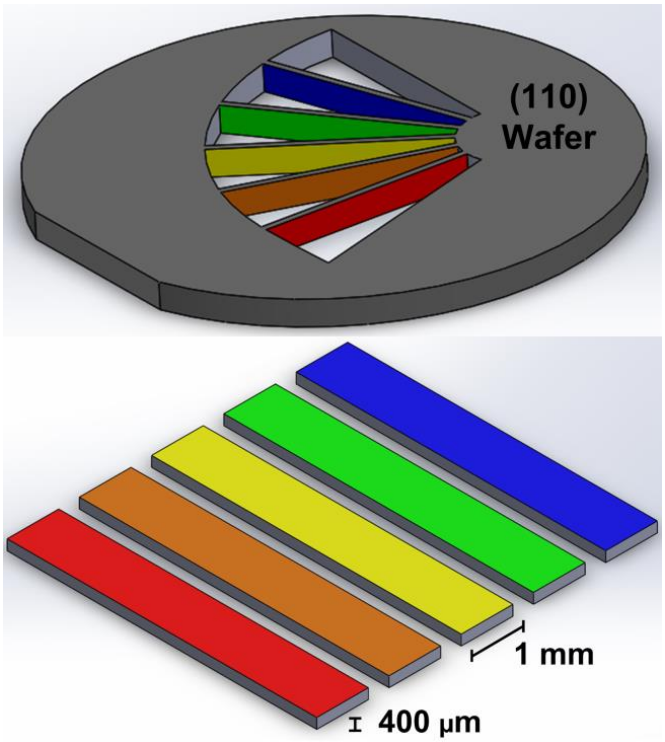


**Figure 7.8 - Silicon strips created from a (110) oriented monocrystalline silicon wafer through laser cutting. Note that the diagram is not to scale for visual illustration purposes.**

The second approach characterises the influence of crystal orientation on surface passivation through imaging carrier lifetimes in silicon strips containing different surface orientations, created from a single monocrystalline silicon wafer via laser cutting. The principle of the approach is demonstrated in Figure 7.8. The starting material is a (110) p-type boron doped Czochralski (Cz) grown monocrystalline silicon with a thickness of 1 mm. The background doping of the sample is around $3.6 \times 10^{16}\ cm^{-3}$. We cut the monocrystalline silicon wafer to produce multiple narrow strips in the wafer frame, as shown in Figure 7.8, using a Coherent Scientific PRISMA 532-V Diode-Pumped Solid-State Laser, operating at $532\ nm$ with nominal pulsed power in the range of $12\ W$ at $30\ kHz$. The width of the strips was approximately $400\ \mu m$. The cutting pattern was designed so that there is a slight rotation angle between each strip. This allows each silicon strip to have a different surface orientation of its sidewalls, denoted by different colours in Figure 7.8. The orientation of the sidewall is determined

by the laser cutting angle relative to the wafer flat, as well as the surface orientation of the wafer used, (110) in this case. Any orientation, in principle, can be achieved via perpendicular cuts through a set of (100), (111) and (110) wafers.

After cutting, the entire wafer, with the strips still attached, was chemically etched for more than 5 minutes using HF and $HNO_3$ in a ratio of 1:10 to remove the surface damage from laser cutting. The width of the strips was reduced from 400 $\mu m$ to around 307 $\mu m$ after etching. The wafer was then subjected to a thermal oxidation, using the same recipe described above in Section 7.3.1.1 to grow silicon oxide films on its front, rear and side surfaces. After oxidation, the strips were detached from the wafer frame, flipped by 90° and imaged with the PL system. A 1 mm thick wafer was chosen for this work to maximise the width of the silicon strips after flipping, and preventing the strips from becoming too narrow to be imaged, considering the spatial resolution of the PL imaging setup used. The surface morphology of the strips was evaluated with an optical microscope, verifying that planar surfaces were achieved on all the strips with no observable difference among the different strips.

#### 7.3.2.2 Lifetime measurements

The size of the silicon strips presents challenges in lifetime measurements. The silicon strips are too small, less than 900 µm wide after etching, to be measured with a typical Quasi-Steady State Photoconductance (QSSPC) lifetime tester [189]. The effective lifetime of each strip was extracted from calibrated PL images, with a lateral spatial resolution of 22 µm per pixel. The injection dependence of the lifetimes was determined from PL images captured at different laser intensities. Since the strips are significantly smaller than the standard QSSPC sensor coil, it is not possible to perform QSSPC lifetime measurement on the silicon strips in order to acquire a calibration constant for the PL images. In this work, PL images were calibrated into absolute lifetime images based on an optically corrected calibration constant extracted from separate monocrystalline calibration wafers, using the method presented in Chapter 3.

Note that we are not able to apply the carrier de-smearing technique (Section 2.2.2.3) to the silicon strips as the strips are too narrow, which significantly affects the accuracy of the noise filtering method used in the de-smearing technique. In principle, the carrier

smearing effect could lead to an underestimation of the extracted lifetime values from the silicon strips. However, such uncertainty is small given that the sidewalls of the silicon strips are also passivated with silicon oxide, unlike the grain boundaries in a mc-Si wafer, coupled with the fact that the Cz wafer used in this section has a lower bulk lifetime than the mc-Si wafers used in Section 7.3.1, resulting in a reduced impact of the carrier smearing effect.

### 7.3.2.3 Extraction of the surface recombination velocity ($S_{eff}$)

A similar approach was used to extract the surface recombination velocities in the silicon strips from the measured lifetime. A silicon strip with a (100) orientated surface was used together with a Float Zone (FZ) control sample to estimate its bulk lifetime. $S_{eff}$ of each grain can then be calculated using equation 7.5. Note that in contrast to Method I described above (Section 7.3.1), it is quite safe to assume all silicon strips have the same bulk lifetime as they were cut from the same monocrystalline silicon wafer. This significantly reduces the uncertainty in the results.

### 7.3.2.4 Results

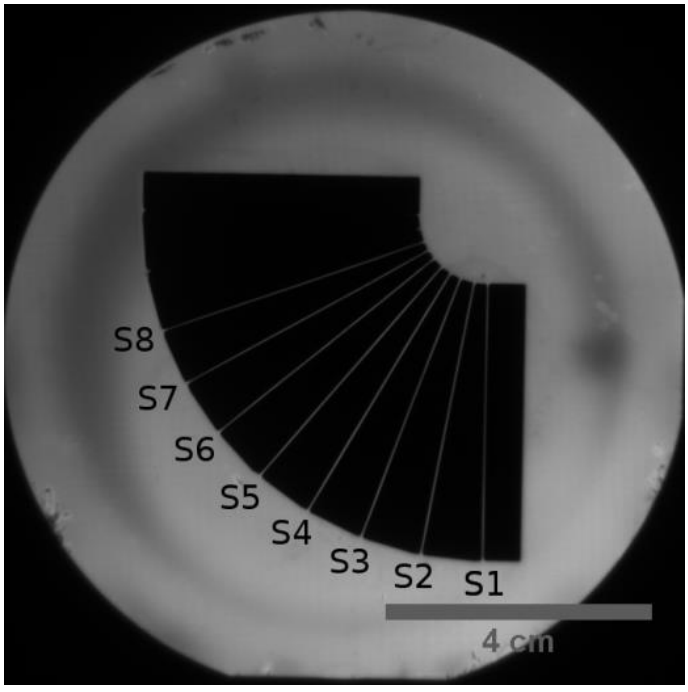


**Figure 7.9 - PL image of silicon strips before being detached from the monocrystalline silicon wafer frame.**

Figure 7.9 shows a PL image of a monocrystalline silicon wafer that has been laser cut and thermally oxidised. Figure 7.10(a) shows a PL calibrated lifetime image of the silicon strips after being detached from the monocrystalline silicon wafer frame and flipped by 90°. Figure 7.10(b) shows a line scan of the lifetimes across these silicon strips. A significant lifetime variation among different silicon strips can be observed. Note that the lifetime values in Figure 7.10(b) were extracted at a constant generation rate; their injection levels can be different owing to their lifetime variation.

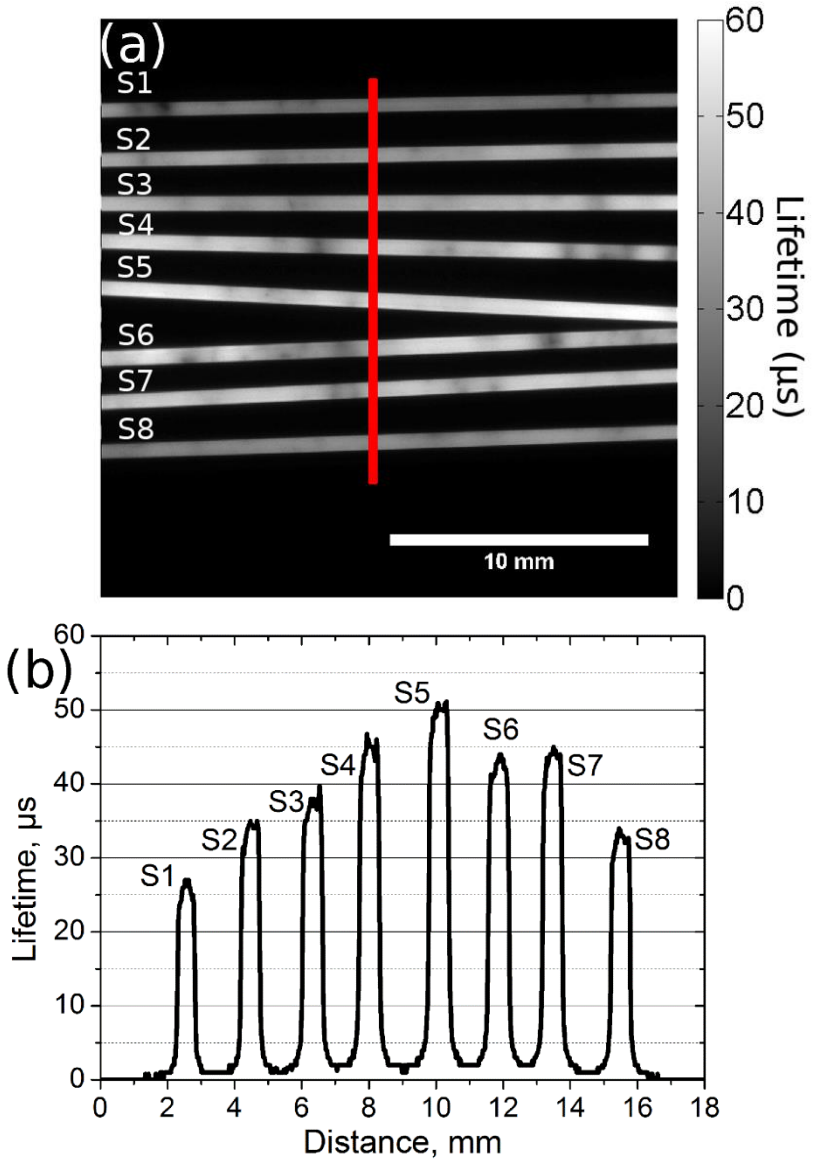


**Figure 7.10 - (a) PL calibrated lifetime image of silicon strips after being detached from the wafer frame and flipped by 90°. The images were taken with incident photon flux of $2.7 \times 10^{18}\ cm^{-2}s^{-1}$. (b) Line scan of the lifetimes across various silicon strips.**

Table 7.2 shows the highest measured lifetime of each strip extracted at an excess carrier density of $1 \times 10^{15}\ cm^{-3}$ and its corresponding $S_{eff}$ value. The lifetimes were measured from the center region in the strips far away from the edge so that the influence of surface recombination in the sidewall (a (110) surface in this case) is minimal. The highest such values were chosen to avoid those darker regions of the strips which show some bulk lifetime degradation. Note also that there is a slight variation ($\ll 5\%$) in the thickness among different strips. The average thickness of $307\ \mu m$ was used in the calculation of the $S_{eff}$ values.

Also shown is the crystal orientation, measured with EBSD, of each silicon strip and its corresponding surface energy, modelled according to equation 7.4. From Table 7.2, it can be seen that the passivation quality of the studied silicon oxide films is strongly influenced by the crystal orientation. Among the eight studied orientations, the $S_{eff}$ value of the (100) orientated strip is the lowest. The $S_{eff}$ values vary from $71\ cm/s$ for the (100) surface to $328\ cm/s$ for the (235) surface.

**Table 7.2 – Crystal orientation, surface energy, effective lifetime and surface recombination velocity of each silicon strip. The surface energies were modelled using equation 7.4. A bulk lifetime of 44 $\mu s$ (determined using a control sample with the method stated above) was used in the calculation of the $S_{eff}$ values.**

| Strips | Orientation | Surface Energy ($J/m^2$) | $\tau_{eff}$ at $1 \times 10^{15}\ cm^{-3}$ ($\mu s$) | $S_{eff}$ ($cm/s$) |
|---|---|---|---|---|
| **S1** | **(235)** | **1.74** | **23** | **328** |
| **S2** | **(214)** | **1.90** | **29** | **187** |
| **S3** | **(103)** | **2.11** | **33** | **120** |
| **S4** | **(106)** | **2.18** | **34** | **106** |
| **S5** | **(100)** | **2.26** | **37** | **71** |
| **S6** | **(013)** | **2.11** | **34** | **106** |
| **S7** | **(215)** | **2.00** | **33** | **121** |
| **S8** | **(112)** | **1.78** | **27** | **214** |

It should be noted that during the calculation of the $S_{eff}$ values with equation 7.5, it is assumed that the carrier density profile is uniform depth-wise. This is not strictly true

for the Cz samples used in this work, owing to the relatively low bulk lifetime of the wafer. However, this only leads to an uncertainty of less than 5% in the extracted $S_{eff}$ values (determined with numerical simulations based on the model presented in Section 4.2, using a bulk lifetime of 44 $\mu s$ and the measured effective lifetimes). Such uncertainty can be further reduced by using wafers with higher lifetime. The boron-oxygen-related defect is likely to be the cause for the low lifetime in the studied Cz wafer, given that the measured lifetimes correlate well with literature reported lifetimes after defect activation [18], which is likely to have occurred to the studied Cz samples during the repeated PL measurements.

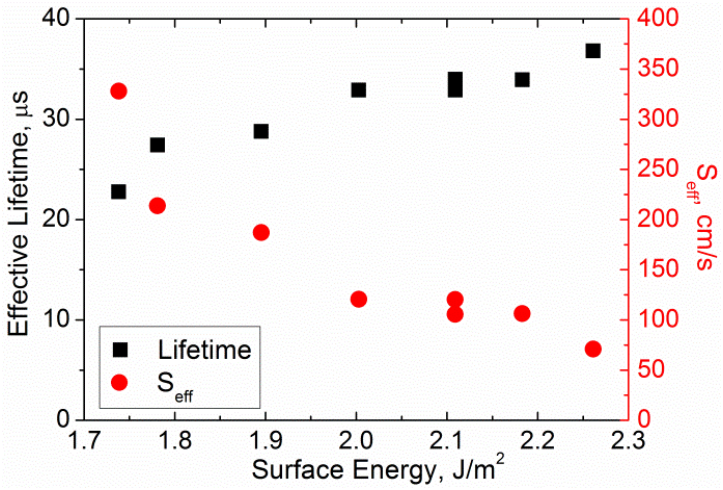


**Figure 7.11 - The effective lifetime and surface recombination velocity of each studied silicon strip classified according to its corresponding surface energy.**

Figure 7.11 correlates the effective lifetimes and surface recombination velocities ($S_{eff}$) of the silicon strips with their corresponding surface energies. A clear trend can be observed between $\tau_{eff}$, $S_{eff}$ and surface energy. The results here show that the studied silicon oxide films are more effective in passivating surfaces with high surface energy such as (100) or (106) surfaces, and less effective in passivating surfaces with low surface energy such as a (235) surface. This is in agreement with the results obtained from Method I (Section 7.3.1) described above.

## 7.3.3 Discussion

Both of the presented methods show that the passivation effectiveness of the studied silicon oxide films is strongly crystal orientation dependent. In general, the surface

recombination rate depends on the doping level/type of the substrate, the charge in the dielectric film, and their interaction. Owing to the variation in the background doping level and type of the samples used, the $S_{eff}$ values extracted from both methods could not be compared directly. The lower $S_{eff}$ values on the mc-Si samples could be related the positive charge in the oxide layer [190], which allows a better passivation on n-type samples owing to field-effect passivation, or due to the different doping concentrations or types in the substrates [191], interacting with the electron and hole capture cross sections at the interface.

In order to compare results obtained from both methods, the extracted $S_{eff}$ value of each orientation was normalised with the $S_{eff}$ value of a (100) orientated grain/strip in the corresponding sample. Figure 7.12 shows the normalised $S_{eff}$ value of each orientation obtained from the two presented methods as a function of its corresponding surface energy. It can be seen that the results from both methods are consistent with each other, indicating the validity of both methods.

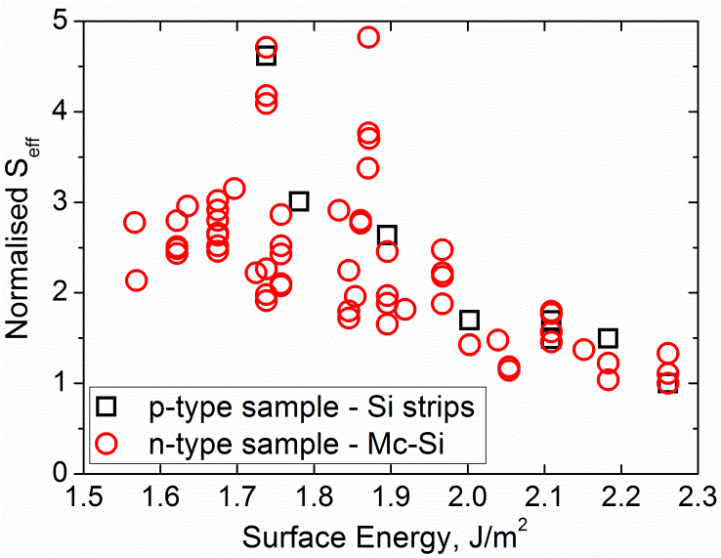


**Figure 7.12 –Normalised $S_{eff}$ value of each orientation obtained from the two presented methods as a function of its corresponding surface energy. The $S_{eff}$ value of each grain/strip is normalised with the $S_{eff}$ value of a (100) orientated grain/strip in the corresponding sample.**

Comparing both approaches, the advantage of the method using the silicon strips is that there is negligible variation in the bulk lifetimes among different strips as they were cut from the same monocrystalline wafer. However, it requires a more complex sample

preparation procedure. The sample size is also limited. On the other hand, the advantage of using mc-Si wafers to study the orientation dependent passivation effect is that the process is simple and easy to implement, thus allowing a large number of orientations to be studied. However, as mentioned above, it relies on the assumption that any varying impact of the bulk lifetime is significantly less than the variation of surface recombination among the mc-Si grains. While this assumption is largely valid for the silicon oxide passivated samples studied in this work, it may not be when applying the method to other dielectric films with lower surface recombination velocities. In such cases, the method of using the silicon strips is likely to be more accurate.

Note that the aim of this work is not to determine whether the passivation effect of a particular dielectric film is affected by crystal orientation, as such influences might vary depending on the deposition conditions, the composition of the films, and the doping of the substrates (diffused or non-diffused). Rather, the aim of the work is to demonstrate the applicability of the two presented methods for evaluating the influence of crystal orientation on surface passivation.

## 7.4 Conclusions

This chapter applies the PL imaging technique to explore surface recombination in silicon wafers. The chapter is divided into two sections. In the first section, PL imaging is applied to thin, chemically polished and unpassivated mc-Si wafers. It is found that the PL intensity from such wafers is dominated by surface recombination, which in turns is crystal orientation dependent. An approach for monitoring crystal orientations in mc-Si wafers based on this correlation is proposed. In the second part, the technique is extended to passivated wafers to characterise the influence of crystal orientation on dielectric passivation. Two methods are presented. The first method is based on imaging carrier lifetimes among different grains in mc-Si wafers. The second method is based on imaging carrier lifetimes in silicon strips cut from a single monocrystalline silicon wafer. Both methods were applied on thermally grown silicon oxide passivated samples. The results from both methods agree with each other, showing that the studied silicon oxide films provide a better passivation on surfaces with higher surface energy, such as (100) surface, compared to those with lower surface energy, such as (111) surface.

# Chapter 8

# Conclusions and Future Work

The recombination behaviour of mc-Si materials are rather complex owing to the presence of numerous types of crystal defects in the materials. This thesis has applied the PL imaging technique to study carrier recombination in mc-Si. One emphasis of the work has been recombination at GBs, which is one of the limiting factors for the performance of mc-Si solar cells. An approach for quantifying the recombination activities of a GB in terms of its effective surface recombination velocity, based on the PL intensity profile across the GB, was developed. Based on their effective surface recombination velocities, the recombination behaviours of GBs from different parts of a p-type boron doped directionally solidified mc-Si ingot were examined in detail. The work was then extended to various types of mc-Si materials. The electrical properties of conventionally solidified p-type, n-type and also recently developed high performance p-type mc-Si wafers were directly compared in terms of their electronic behaviours in the intra-grain regions, the GBs and the dislocation networks. Apart from recombination through crystal defects within the bulk, recombination at surfaces acts as another significant loss mechanism in solar cells. This thesis also demonstrated the use of the PL imaging technique to study surface recombination in silicon wafers, and provided some examples of such applications.

The main findings of the work and the suggested further work are summarised below.

## Calibrating photoluminescence-based lifetime images on mc-Si wafers

A method for converting PL images into carrier lifetime images for wafers with inhomogeneous lifetime distributions, such as mc-Si wafers, was presented. The method is based on an optically-corrected calibration factor extracted from PL and QSSPC measurements on a separate calibration wafer with homogeneous lifetime. Experimental results show that the lifetimes calibrated by the proposed method are more consistent

compared to the conventional QSSPC based calibration methods, in which the accuracy of the calibration was found to be affected by measurement artefacts in the QSSPC measurements on mc-Si wafers, possibly due to minority carrier trapping and the radial sensitivity of the QSSPC sensor coil.

# Recombination at grain boundaries in p-type mc-Si

GBs from different parts of a mc-Si ingot exhibit different recombination behaviours. Overall, as-grown GBs from the middle of the studied mc-Si ingot tend to be less recombination active compared to GBs from the top and bottom of the same ingot. However, their recombination strength increases significantly after either gettering or hydrogenation, and they become even more active than GBs from the top and bottom of the ingot, which inherently contain a higher level of metal impurity concentrations. Moreover, two types of GBs were identified based on their distinct injection dependent recombination behaviours. While some GBs exhibit little injection dependence before gettering, others show a rather strong injection dependence, with $S_{GB}$ increasing as the injection level decreases.

All the results above suggest that the impurity levels in the materials significantly impact the electrical properties of as-grown GBs, and also their response to phosphorus gettering and hydrogenation. It still remains unclear about the types of impurities that are responsible for the observed behaviours. A possible extension of the work is to measure the impurity concentrations in the studied materials, through techniques such as Neutron Activation Analysis (NAA) [130, 192] or Inductively Coupled Plasma Mass Spectrometry (ICP-MS) [20, 193], and correlate them with the observed behaviours. Microscopy study could also provide further insight about the origin of GB recombination. This could involve examining the microscopic structure of GBs of different geometries through Transmission Electron Microscopy (TEM) [63, 194, 195] or applying techniques such as synchrotron-based microprobe [22, 137, 196, 197] or atom probe tomography [27] to identify the types and forms of impurities decorated around the GBs.

Another important contribution of this work is to allow the recombination properties of a GB to be quantified in an absolute measure in terms of its surface recombination

velocity. Based on the extracted surface recombination velocities, it is possible to perform 2D or 3D simulations [198] to accurately determine the detrimental impact of GBs on the performance of solar cells of different device structures under various operating operations. This would allow a more accurate assessment of the material quality of mc-Si.

## Direct comparison of the electrical properties of various mc-Si materials for solar cells

All studied mc-Si materials show reasonably high diffusion lengths ($> 800$ μ$m$) among the intra-grain regions after gettering and hydrogenation, suggesting that the main performance limiting factors in mc-Si solar cells are likely to be recombination at crystal defects. Among the three mc-Si materials studied in this work, it is expected that both the conventional n-type and the high performance p-type mc-Si samples would outperform the conventional p-type mc-Si samples. N-type mc-Si material shows superior electrical properties in the intra-grain regions (highest lifetimes) and GBs (relatively inactive), especially after both gettering and hydrogenation. High performance p-type mc-Si material contains significantly fewer dislocation networks. The results suggest that high performance n-type mc-Si material could be an ideal material for high efficiency low cost solar cells, owing to its anticipated properties of high intra-grain lifetimes, relatively inactive GBs, and fewer dislocations networks.

It is noted that the analysis presented in this work is solely based on three studied mc-Si ingots. The electrical properties of mc-Si materials can vary to a large extent, depending on factors such as the ingot growth conditions or the impurity concentrations in the materials. An important area of future work is to examine more mc-Si materials, including high performance n-type mc-Si, possibly from different ingot manufacturers, in order to verify the findings and obtain a more representative conclusion.

On the other hand, it was observed that the electrical properties of mc-Si materials change significantly after phosphorus gettering and hydrogenation. While gettering significantly improves the lifetimes of the intra-grain regions, it also increases the recombination strength of most of the crystal defects. The benefits of hydrogenation are

clear, both on the intra-grain regions and the crystal defects. However, its effectiveness varies considerably among different mc-Si materials, being more effective on the n-type samples than the p-type samples.

Due to time constraints, only one recipe of gettering and hydrogenation was studied in this work. The process conditions, such as the temperature used for the gettering or hydrogenation, can affect the results. For example, experimental work by Fenning *et al.* [199] suggested that a higher temperature phosphorus diffusion gettering can, in some cases, reduce the dislocation density in mc-Si. Hallam *et al.* [200] claimed that the effectiveness of hydrogen passivation can be improved through applying illumination during the process. One possible extension of this thesis is to examine a wide range of process conditions for phosphorus gettering and hydrogenation using various types of mc-Si materials, to develop an optimised gettering and hydrogenation process that is suitable for mc-Si for solar cell applications.

# The Influence of Crystal Orientation on Surface Recombination in mc-Si

A strong PL contrast was observed among different grains in thin, chemically polished and unpassivated mc-Si wafers. It was found that the PL intensity from such wafers is dominated by surface recombination, which in turns is crystal orientation dependent. The result highlights the possibility of using PL images to monitor crystal orientations in mc-Si wafers, and to study surface recombination in silicon wafers. Two methods for evaluating the influence of crystal orientation on dielectric passivation were presented, and demonstrated with silicon oxide passivated samples. The methods allow the impact of various crystal orientations, not limited only to (100), (110) and (111) planes, to be studied. Both methods revealed that the studied silicon oxide films provide a better passivation on surfaces with higher surface energy, such as (100) or (106) surfaces, compared to those with lower surface energy, such as (235) or (111) surfaces. The methods demonstrated in this work can potentially be applied to other dielectric films such as silicon nitride or aluminum oxide to investigate the orientation dependence of the passivation. The results of such studies may allow an improved understanding of the impact of various planes to recombination at textured surfaces.

# List of Publications

## Publications arising from the work in this thesis:

### Refereed journal papers:

1. **H. C. Sio**, T. K. Chong, S. Surve, K. Weber, and D. Macdonald, "Characterizing the Influence of Crystal Orientation on Surface Recombination in Silicon Wafers," *IEEE Journal of Photovoltaics,* vol. 6, pp. 412-418, 2016.
2. **H. C. Sio** and D. Macdonald, "Direct comparison of the electrical properties of multicrystalline silicon materials for solar cells: conventional p-type, n-type and high performance p-type," *Solar Energy Materials and Solar Cells,* vol. 144, pp. 339-346, 2016.
3. **H. C. Sio**, S. P. Phang, T. Trupke, and D. Macdonald, "Impact of Phosphorous Gettering and Hydrogenation on the Surface Recombination Velocity of Grain Boundaries in p-Type Multicrystalline Silicon," *IEEE Journal of Photovoltaics,* vol. 5, pp. 1357-1365, 2015.
4. **H. C. Sio**, T. Trupke, and D. Macdonald, "Quantifying carrier recombination at grain boundaries in multicrystalline silicon wafers through photoluminescence imaging," *Journal of Applied Physics,* vol. 116, p. 244905, 2014.
5. **H. C. Sio**, S. P. Phang, T. Trupke, and D. Macdonald, "An accurate method for calibrating photoluminescence-based lifetime images on multi-crystalline silicon wafers," *Solar Energy Materials and Solar Cells*, vol. 131, pp. 77-84, 2014.
6. **H. C. Sio**, Z. Xiong, T. Trupke, and D. Macdonald, "Imaging crystal orientations in multicrystalline silicon wafers via photoluminescence," *Applied Physics Letters,* vol. 101, p. 082102, 2012.

### Conference papers:

7. **H. C. Sio**, S. P. Phang, H. T. Nguyen, D. Yan, T. Trupke, and D. Macdonald, "Comparison of recombination activity of grain boundaries in various multicrystalline silicon materials " *Proceeding of the 31th European Photovoltaic Solar Energy Conference*, Hamburg, Germany, 2015.

8. **H. C. Sio**, T. Trupke, and D. Macdonald, "Quantifying the recombination strength of grain boundaries in multicrystalline silicon wafers through photoluminescence imaging," *Proceeding of the 6th World Conference on Photovoltaic Energy Conversion*, Kyoto, Japan, 2014.
9. **H. C. Sio**, S. P. Phang, Y. Wan, W. Liang, T. Trupke, S. Cao, D. Hu, Y. Wan and D. Macdonald, "The influence of crystal orientation on surface passivation in multi-crystalline silicon," *Proceeding of the 39th IEEE Photovoltaic Specialists Conference (PVSC)*, Tampa, USA, pp. 1770-1775, 2013.
10. **H. C. Sio**, T. Trupke, S. P. Phang, and D. Macdonald, "Electrical properties of different types of grain boundaries in multicrystalline silicon by photoluminescence imaging," *Proceedings of the 27th European Photovoltaic Solar Energy Con*ference, Frankfurt, 2012.

## Other publications by the author:

11. S. P. Phang, **H. C. Sio**, and D. Macdonald, "Applications of carrier de-smearing of photoluminescence images on silicon wafers," *Progress in Photovoltaics: Research and Applications*, 2016.
12. S. P. Phang, **H. C. Sio**, and D. Macdonald, "Carrier de-smearing of photoluminescence images on silicon wafers using the continuity equation," *Applied Physics Letters*, vol. 103, p. 192112, 2013.

# Bibliography


[1] "ITRPV 2014, International Technology Roadmap for Photovoltaic Results 2014," 2015.

[2] T. Trupke, R. A. Bardos, M. C. Schubert, and W. Warta, "Photoluminescence imaging of silicon wafers," *Applied Physics Letters,* vol. 89, p. 044107, 2006.

[3] D. Macdonald and A. Cuevas, "Trapping of minority carriers in multicrystalline silicon," *Applied Physics Letters,* vol. 74, p. 1710, 1999.

[4] A. Cuevas, M. Stocks, D. McDonald, M. Kerr, and C. Samundsett, "Recombination and trapping in multicrystalline silicon," *Electron Devices, IEEE Transactions on,* vol. 46, pp. 2026-2034, 1999.

[5] J. Chen, T. Sekiguchi, D. Yang, F. Yin, K. Kido, and S. Tsurekawa, "Electron-beam-induced current study of grain boundaries in multicrystalline silicon," *Journal of Applied Physics,* vol. 96, pp. 5490-5495, 2004.

[6] "Photovoltaics Report," Fraunhofer Institute for Solar Energy Systems ISE 2014.

[7] J. Zhao, A. Wang, and M. A. Green, "24·5% Efficiency silicon PERT cells on MCZ substrates and 24·7% efficiency PERL cells on FZ substrates," *Progress in Photovoltaics: Research and Applications,* vol. 7, pp. 471-474, 1999.

[8] R. M. Swanson, S. K. Beckwith, R. A. Crane, W. D. Eades, K. Young Hoon, R. A. Sinton, *et al.*, "Point-contact silicon solar cells," *Electron Devices, IEEE Transactions on,* vol. 31, pp. 661-664, 1984.

[9] K. Fujiwara, W. Pan, N. Usami, K. Sawada, M. Tokairin, Y. Nose, *et al.*, "Growth of structure-controlled polycrystalline silicon ingots for solar cells by casting," *Acta Materialia,* vol. 54, pp. 3191-3197, 2006.

[10] K. Fujiwara, W. Pan, K. Sawada, M. Tokairin, N. Usami, Y. Nose, *et al.*, "Directional growth method to obtain high quality polycrystalline silicon from its melt," *Journal of Crystal Growth,* vol. 292, pp. 282-285, 2006.

[11] C. W. Lan, W. C. Lan, T. F. Lee, A. Yu, Y. M. Yang, W. C. Hsu, *et al.*, "Grain control in directional solidification of photovoltaic silicon," *Journal of Crystal Growth,* vol. 360, pp. 68-75, 2012.

[12] Y. M. Yang, A. Yu, B. Hsu, W. C. Hsu, A. Yang, and C. W. Lan, "Development of high-performance multicrystalline silicon for photovoltaic industry," *Progress in Photovoltaics: Research and Applications,* vol. 23, pp. 340-351, 2015.

[13] G. Stokkan, Y. Hu, Ø. Mjøs, and M. Juel, "Study of evolution of dislocation clusters in high performance multicrystalline silicon," *Solar Energy Materials and Solar Cells,* vol. 130, pp. 679-685, 2014.

[14] P. J. Cousins, D. D. Smith, L. Hsin-Chiao, J. Manning, T. D. Dennis, A. Waldhauer, *et al.*, "Generation 3: Improved performance at lower cost," *Proceedings of the 35th IEEE Photovoltaic Specialists Conference,* pp. 275-278, 2010.

[15] M. A. Green, K. Emery, Y. Hishikawa, W. Warta, and E. D. Dunlop, "Solar cell efficiency tables (Version 45)," *Progress in Photovoltaics: Research and Applications,* vol. 23, pp. 1-9, 2015.

[16] "Panasonic HIT® Solar Cell Achieves World's Highest Energy Conversion Efficiency of 25.6% at Research Level," Panasonic Press Release, 10 April 2014.

[17] J. Schmidt and A. Cuevas, "Electronic properties of light-induced recombination centers in boron-doped Czochralski silicon," *Journal of Applied Physics,* vol. 86, pp. 3175-3180, 1999.

[18] K. Bothe, R. Sinton, and J. Schmidt, "Fundamental boron–oxygen-related carrier lifetime limit in mono- and multicrystalline silicon," *Progress in Photovoltaics: Research and Applications,* vol. 13, pp. 287-296, 2005.

[19] D. Macdonald and L. J. Geerligs, "Recombination activity of interstitial iron and other transition metal point defects in p- and n-type crystalline silicon," *Applied Physics Letters,* vol. 85, pp. 4061-4063, 2004.

[20] P. Karzel, M. Ackermann, L. Gröner, C. Reimann, M. Zschorsch, S. Meyer, *et al.*, "Dependence of phosphorus gettering and hydrogen passivation efficacy on grain boundary type in multicrystalline silicon," *Journal of Applied Physics,* vol. 114, p. 244902, 2013.

[21] J. Chen and T. Sekiguchi, "Carrier recombination activity and structural properties of small-angle grain boundaries in multicrystalline silicon," *Japanese Journal of Applied Physics Part 1-Regular Papers Brief Communications & Review Papers,* vol. 46, pp. 6489-6497, Oct 2007.

[22] T. Buonassisi, A. A. Istratov, M. D. Pickett, M. A. Marcus, T. F. Ciszek, and E. R. Weber, "Metal precipitation at grain boundaries in silicon: Dependence on grain boundary character and dislocation decoration," *Applied Physics Letters,* vol. 89, p. 042102, 2006.

[23] S. Joonwichien, S. Matsushima, and N. Usami, "Effects of crystal defects and their interactions with impurities on electrical properties of multicrystalline Si," *Journal of Applied Physics,* vol. 113, p. 133503, 2013.

[24] I. Takahashi, N. Usami, H. Mizuseki, Y. Kawazoe, G. Stokkan, and K. Nakajima, "Impact of type of crystal defects in multicrystalline Si on electrical properties and interaction with impurities," *Journal of Applied Physics,* vol. 109, p. 033504, 2011.

[25] T. Sekiguchi, J. Chen, W. Lee, and H. Onodera, "Electrical and optical activities of small angle grain boundaries in multicrystalline Si," *physica status solidi (c),* vol. 8, pp. 1347-1350, 2011.

[26] V. Kveder, M. Kittler, and W. Schröter, "Recombination activity of contaminated dislocations in silicon: A model describing electron-beam-induced current contrast behavior," *Physical Review B,* vol. 63, p. 115208, 2001.

[27] A. Stoffers, O. Cojocaru-Mirédin, W. Seifert, S. Zaefferer, S. Riepe, and D. Raabe, "Grain boundary segregation in multicrystalline silicon: correlative characterization by EBSD, EBIC, and atom probe tomography," *Progress in Photovoltaics: Research and Applications,* 2015.

[28] H. Nouri, M. Bouaïcha, M. Ben Rabha, and B. Bessaïs, "Gettering effect in grain boundaries of multi-crystalline silicon," *physica status solidi (c),* vol. 9, pp. 1937-1941, 2012.

[29] L. J. Geerligs, Y. Komatsu, I. Röver, K. Wambach, I. Yamaga, and T. Saitoh, "Precipitates and hydrogen passivation at crystal defects in n- and p-type multicrystalline silicon," *Journal of Applied Physics,* vol. 102, p. 093702, 2007.

[30] T. Jiang, X. Yu, X. Gu, D. Yang, and G. Rozgonyi, "Hydrogenation of interface states at a clean grain boundary in the direct silicon bonded wafer," *physica status solidi (a),* vol. 209, pp. 990-993, 2012.

[31] M. I. Bertoni, S. Hudelson, B. K. Newman, D. P. Fenning, H. F. W. Dekkers, E. Cornagliotti, *et al.*, "Influence of defect type on hydrogen passivation efficacy in multicrystalline silicon solar cells," *Progress in Photovoltaics: Research and Applications,* vol. 19, pp. 187-191, 2011.

[32] J. Chen, D. Yang, Z. Xi, and T. Sekiguchi, "Electron-beam-induced current study of hydrogen passivation on grain boundaries in multicrystalline silicon: Influence of GB character and impurity contamination," *Physica B: Condensed Matter,* vol. 364, pp. 162-169, 2005.

[33] S. C. Baker-Finch and K. R. McIntosh, "The Contribution of Planes, Vertices, and Edges to Recombination at Pyramidally Textured Surfaces," *IEEE Journal of Photovoltaics,* vol. 1, pp. 59-65, 2011.

[34] U. K. Das, M. Z. Burrows, M. Lu, S. Bowden, and R. W. Birkmire, "Surface passivation and heterojunction cells on Si (100) and (111) wafers using dc and rf plasma deposited Si:H thin films," *Applied Physics Letters,* vol. 92, p. 063504, 2008.

[35] A. Descoeudres, L. Barraud, S. De Wolf, B. Strahm, D. Lachenal, C. Guérin, *et al.*, "Improved amorphous/crystalline silicon interface passivation by hydrogen plasma treatment," *Applied Physics Letters,* vol. 99, p. 123506, 2011.

[36] M. A. Green, *Solar cells: operating principles, technology, and system applications*. Kensington: The University of New South Wales, 1998.

[37] T. Trupke, M. A. Green, P. Würfel, P. P. Altermatt, A. Wang, J. Zhao, *et al.*, "Temperature dependence of the radiative recombination coefficient of intrinsic crystalline silicon," *Journal of Applied Physics,* vol. 94, pp. 4930-4937, 2003.

[38] J. Dziewior and W. Schmid, "Auger coefficients for highly doped and highly excited silicon," *Applied Physics Letters,* vol. 31, pp. 346-348, 1977.

[39] P. P. Altermatt, J. Schmidt, G. Heiser, and A. G. Aberle, "Assessment and parameterisation of Coulomb-enhanced Auger recombination coefficients in lowly injected crystalline silicon," *Journal of Applied Physics,* vol. 82, pp. 4938-4944, 1997.

[40] A. Hangleiter and R. Häcker, "Enhancement of band-to-band Auger recombination by electron-hole correlations," *Physical Review Letters,* vol. 65, pp. 215-218, 1990.

[41] D. B. Laks, G. F. Neumark, and S. T. Pantelides, "Accurate interband-Auger-recombination rates in silicon," *Physical Review B,* vol. 42, pp. 5176-5185, 1990.

[42] M. Govoni, I. Marri, and S. Ossicini, "Auger recombination in Si and GaAs semiconductors: Ab initio results," *Physical Review B,* vol. 84, p. 075215, 08/15/ 2011.

[43] M. J. Kerr and A. Cuevas, "General parameterization of Auger recombination in crystalline silicon," *Journal of Applied Physics,* vol. 91, pp. 2473-2480, 2002.

[44] A. Richter, S. W. Glunz, F. Werner, J. Schmidt, and A. Cuevas, "Improved quantitative description of Auger recombination in crystalline silicon," *Physical Review B,* vol. 86, p. 165202, 2012.

[45] J. Nelson, *The physics of solar cells*: Imperial College Press, 2003.

[46] W. Shockley and W. T. Read, "Statistics of the Recombinations of Holes and Electrons," *Physical Review,* vol. 87, pp. 835-842, 1952.

[47] R. N. Hall, "Electron-Hole Recombination in Germanium," *Physical Review,* vol. 87, pp. 387-387, 1952.

[48] C. Sun, F. E. Rougieux, and D. Macdonald, "Reassessment of the recombination parameters of chromium in n- and p-type crystalline silicon and chromium-boron pairs in p-type crystalline silicon," *Journal of Applied Physics,* vol. 115, p. 214907, 2014.

[49] D. Macdonald, J. Tan, and T. Trupke, "Imaging interstitial iron concentrations in boron-doped crystalline silicon using photoluminescence," *Journal of Applied Physics,* vol. 103, p. 073710, 2008.

[50] A. A. Istratov, H. Hieslmair, and E. R. Weber, "Iron and its complexes in silicon," *Applied Physics A,* vol. 69, pp. 13-44, 1999.

[51] B. B. Paudyal, K. R. McIntosh, and D. H. Macdonald, "Temperature dependent carrier lifetime studies on Ti-doped multicrystalline silicon," *Journal of Applied Physics,* vol. 105, p. 124510, 2009.

[52] K. Graff, *Metal impurities in silicon-device fabrication*: Springer-Verlag Berlin Heidelberg, 2000.

[53] C.-T. Sah, P. C. H. Chan, C.-K. Wang, C.-T. Sah, K. A. Yamakawa, and R. Lutwack, "Effect of zinc impurity on silicon solar-cell efficiency," *IEEE Transactions on Electron Devices,* vol. 28, pp. 304-313, 1981.

[54] A. G. Martin, *Silicon Solar Cells: Advanced Principles & Practice*. Sydney: Centre for Photovoltaic Devices and Systems, University of New South Wales, 1995.

[55] A. G. Aberle, *Crystalline Silicon Solar Cells: Advanced Surface Passivation and Analysis*. Sydney: Centre for Photovoltaic Engineering, University of New South Wales, 1999.

[56] V. Randle, *The Measurement of Grain Boundary Geometry*: Institute of Physics Pub., 1993.

[57] A. Voigt, E. Wolf, and H. Strunk, "Grain orientation and grain boundaries in cast multicrystalline silicon," *Materials Science and Engineering B,* vol. 54, pp. 202-206, 1998.

[58] D. G. Brandon, "The structure of high-angle grain boundaries," *Acta Metallurgica,* vol. 14, pp. 1479-1484, 1966.

[59] G. H. Bishop and B. Chalmers, "A coincidence — Ledge — Dislocation description of grain boundaries," *Scripta Metallurgica,* vol. 2, pp. 133-139, 1968.

[60] V. Randle, "The coincidence site lattice and the 'sigma enigma'," *Materials Characterization,* vol. 47, pp. 411-416, 2001.

[61] I. MacLaren and M. Aindow, "Analysis of the reference structure adopted by a mixed tilt-twist vicinal high-angle grain boundary in titanium," *Philosophical Magazine A,* vol. 76, pp. 871-888, 1997.

[62] M. Nacke, M. Allardt, P. Chekhonin, E. Hieckmann, W. Skrotzki, and J. Weber, "Investigations on residual strains and the cathodoluminescence and electron beam induced current signal of grain boundaries in silicon," *Journal of Applied Physics,* vol. 115, p. 163511, Apr 2014.

[63] B. Chen, J. Chen, T. Sekiguchi, M. Saito, and K. Kimoto, "Structural characterization and iron detection at Sigma 3 grain boundaries in multicrystalline silicon," *Journal of Applied Physics,* vol. 105, p. 113502, 2009.

[64] R. A. Sinton, A. Cuevas, and M. Stuckings, "Quasi-steady-state photoconductance, a new method for solar cell material and device characterization," *Proceedings of the 25th IEEE Photovoltaic Specialists Conference,* pp. 457-460, 1996.

[65] D. B. M. Klaassen, "A unified mobility model for device simulation—I. Model equations and concentration dependence," *Solid-State Electronics,* vol. 35, pp. 953-959, 1992.

[66] D. B. M. Klaassen, "A unified mobility model for device simulation—II. Temperature dependence of carrier mobility and lifetime," *Solid-State Electronics,* vol. 35, pp. 961-967, 1992.

[67] R. A. Sinton, *Proceedings of the 9th Workshop Role of Impurities and Defects in Silicon Device Processing,* p. 67, 1999.

[68] D. Macdonald, R. A. Sinton, and A. Cuevas, "On the use of a bias-light correction for trapping effects in photoconductance-based lifetime measurements of silicon," *Journal of Applied Physics,* vol. 89, pp. 2772-2778, 2001.

[69] S. Herlufsen, J. Schmidt, D. Hinken, K. Bothe, and R. Brendel, "Photoconductance-calibrated photoluminescence lifetime imaging of crystalline silicon," *physica status solidi (RRL) – Rapid Research Letters,* vol. 2, pp. 245-247, 2008.

[70] J. A. Giesecke, M. C. Schubert, B. Michl, F. Schindler, and W. Warta, "Minority carrier lifetime imaging of silicon wafers calibrated by quasi-steady-state photoluminescence," *Solar Energy Materials and Solar Cells,* vol. 95, pp. 1011-1018, 2011.

[71] H. Kampwerth, T. Trupke, J. W. Weber, and Y. Augarten, "Advanced luminescence based effective series resistance imaging of silicon solar cells," *Applied Physics Letters,* vol. 93, p. 202102, 2008.

[72] T. Trupke, E. Pink, R. A. Bardos, and M. D. Abbott, "Spatially resolved series resistance of silicon solar cells obtained from luminescence imaging," *Applied Physics Letters,* vol. 90, p. 093506, 2007.

[73] O. Breitenstein, J. Bauer, T. Trupke, and R. A. Bardos, "On the detection of shunts in silicon solar cells by photo-and electroluminescence imaging," *Progress in Photovoltaics: Research and Applications,* vol. 16, pp. 325-330, 2008.

[74] M. Kasemann, D. Grote, B. Walter, W. Kwapil, T. Trupke, Y. Augarten, *et al.*, "Luminescence imaging for the detection of shunts on silicon solar cells," *Progress in Photovoltaics: Research and Applications,* vol. 16, pp. 297-305, 2008.

[75] S. Y. Lim, S. P. Phang, T. Trupke, A. Cuevas, and D. Macdonald, "Dopant concentration imaging in crystalline silicon wafers by band-to-band photoluminescence," *Journal of Applied Physics,* vol. 110, p. 113712, 2011.

[76] M. Bail, M. Schulz, and R. Brendel, "Space-charge region-dominated steady-state photoconductance in low-lifetime Si wafers," *Applied Physics Letters,* vol. 82, pp. 757-759, 2003.

[77] R. A. Bardos, T. Trupke, M. C. Schubert, and T. Roth, "Trapping artifacts in quasi-steady-state photoluminescence and photoconductance lifetime measurements on silicon wafers," *Applied Physics Letters,* vol. 88, p. 053504, 2006.

[78] P. Würfel, T. Trupke, T. Puzzer, E. Schäffer, W. Warta, and S. W. Glunz, "Diffusion lengths of silicon solar cells from luminescence images," *Journal of Applied Physics,* vol. 101, p. 123110, 2007.

[79] D. C. Walter, A. Liu, E. Franklin, D. Macdonald, B. Mitchell, and T. Trupke, "Contrast Enhancement of Luminescence Images via Point-Spread Deconvolution," *Proceedings of the 38th IEEE Photovoltaic Specialists Conference*, pp. 307-312, 2012.

[80] W. H. Richardson, "Bayesian-based iterative method of image restoration," *JOSA*, vol. 62, pp. 55-59, 1972.

[81] C. Vonesch and M. Unser, "A fast thresholded Landweber algorithm for wavelet-regularized multidimensional deconvolution," *IEEE Transactions on Image Processing*, vol. 17, pp. 539-549, 2008.

[82] D. Walter, A. Fell, E. Franklin, D. Macdonald, B. Mitchell, and T. Trupke, "The Impact of Silicon CCD Photon Spread on Quantitative Analyses of Luminescence Images," *IEEE Journal of Photovoltaics*, vol. 4, pp. 368-373, 2014.

[83] T. Trupke, E. Daub, and P. Würfel, "Absorptivity of silicon solar cells obtained from luminescence," *Solar Energy Materials and Solar Cells*, vol. 53, pp. 103-114, 1998.

[84] S. P. Phang, H. C. Sio, and D. Macdonald, "Carrier de-smearing of photoluminescence images on silicon wafers using the continuity equation," *Applied Physics Letters*, vol. 103, p. 192112, 2013.

[85] A. Cuevas, "Modelling silicon characterisation," *Energy Procedia*, vol. 8, pp. 94-99, 2011.

[86] T. Maitland and S. Sitzman, "Electron Backscatter Diffraction (EBSD) Technique and Materials Characterization Examples," in *Scanning microscopy for nanotechnology: techniques and applications*, W. Zhou and Z. L. Wang, Eds., ed: Springer science & business media, 2007.

[87] *Channel 5 User Manual*. Hobro, Denmark: Oxford Instruments HKL, 2007.

[88] D. E. Kane and R. M. Swanson, "Measurement of the emitter saturation current by a contactless photoconductivity decay method," *Proceedings of the 18th IEEE Photovoltaic Specialists Conference*, pp. 578-583, 1985.

[89] M. Müller, P. P. Altermatt, K. Schlegel, and G. Fischer, "A Method for Imaging the Emitter Saturation Current With Lateral Resolution," *IEEE Journal of Photovoltaics*, vol. 2, pp. 586-588, 2012.

[90] P. P. Altermatt, F. Geelhaar, T. Trupke, X. Dai, A. Neisser, and E. Daub, "Injection dependence of spontaneous radiative recombination in c-Si: experiment, theoretical analysis, and simulation," *Proceedings of the 5th International Conference on Numerical Simulation of Optoelectronic Devices*, pp. 47-48, 2005.

[91] P. P. Altermatt, F. Geelhaar, T. Trupke, X. Dai, A. Neisser, and E. Daub, "Injection dependence of spontaneous radiative recombination in crystalline silicon: Experimental verification and theoretical analysis," *Applied Physics Letters*, vol. 88, p. 261901, 2006.

[92] B. Mitchell, T. Trupke, J. W. Weber, and J. Nyhus, "Bulk minority carrier lifetimes and doping of silicon bricks from photoluminescence intensity ratios," *Journal of Applied Physics*, vol. 109, 2011.

[93] S. Herlufsen, K. Ramspeck, D. Hinken, A. Schmidt, J. Müller, K. Bothe, *et al.*, "Dynamic photoluminescence lifetime imaging for the characterisation of silicon wafers," *physica status solidi (RRL) – Rapid Research Letters*, vol. 5, pp. 25-27, 2011.

[94] D. Kiliani, G. Micard, B. Steuer, B. Raabe, A. Herguth, and G. Hahn, "Minority charge carrier lifetime mapping of crystalline silicon wafers by time-resolved photoluminescence imaging," *Journal of Applied Physics,* vol. 110, p. 054508, 2011.

[95] J. Giesecke, "Quantitative Recombination and Transport Properties in Silicon from Dynamic Luminescence," Springer International Publishing, Switzerland, 2014.

[96] A. Fell, D. Walter, S. Kluska, E. Franklin, and K. Weber, "Determination of Injection Dependent Recombination Properties of Locally Processed Surface Regions," *Energy Procedia,* vol. 38, pp. 22-31, 2013.

[97] P. Würfel, S. Finkbeiner, and E. Daub, "Generalized Planck's radiation law for luminescence via indirect transitions," *Applied Physics A,* vol. 60, pp. 67-70, 1995.

[98] P. Würfel, "The chemical potential of radiation," *Journal of Physics C: Solid State Physics,* vol. 15, p. 3967, 1982.

[99] M. A. Green, "Self-consistent optical parameters of intrinsic silicon at 300K including temperature coefficients," *Solar Energy Materials and Solar Cells,* vol. 92, pp. 1305-1310, 2008.

[100] K. Schick, E. Daub, S. Finkbeiner, and P. Würfel, "Verification of a generalized Planck law for luminescence radiation from silicon solar cells," *Applied Physics A,* vol. 54, pp. 109-114, 1992.

[101] B. Mitchell, J. Greulich, and T. Trupke, "Quantifying the effect of minority carrier diffusion and free carrier absorption on photoluminescence bulk lifetime imaging of silicon bricks," *Solar Energy Materials and Solar Cells,* vol. 107, pp. 75-80, 2012.

[102] D. K. Schroder, R. N. Thomas, and J. C. Swartz, "Free Carrier Absorption in Silicon," *IEEE Journal of Solid-State Circuits,* vol. 13, pp. 180-187, 1978.

[103] J. A. Giesecke, M. Kasemann, and W. Warta, "Determination of local minority carrier diffusion lengths in crystalline silicon from luminescence images," *Journal of Applied Physics,* vol. 106, p. 014907, 2009.

[104] A. Schenk, "Finite-temperature full random-phase approximation model of band gap narrowing for silicon device simulation," *Journal of Applied Physics,* vol. 84, pp. 3684-3695, 1998.

[105] P. P. Altermatt, A. Schenk, F. Geelhaar, and G. Heiser, "Reassessment of the intrinsic carrier density in crystalline silicon in view of band-gap narrowing," *Journal of Applied Physics,* vol. 93, pp. 1598-1604, 2003.

[106] F. Schindler, J. Geilker, W. Kwapil, W. Warta, and M. C. Schubert, "Hall mobility in multicrystalline silicon," *Journal of Applied Physics,* vol. 110, p. 043722, 2011.

[107] O. Palais, L. Clerc, A. Arcari, M. Stemmer, and S. Martinuzzi, "Mapping of minority carrier lifetime and mobility in imperfect silicon wafers," *Materials Science and Engineering: B,* vol. 102, pp. 184-188, 2003.

[108] S. Bowden and R. A. Sinton, "Determining lifetime in silicon blocks and wafers with accurate expressions for carrier density," *Journal of Applied Physics,* vol. 102, p. 124501, 2007.

[109] S. Herlufsen, D. Hinken, M. Offer, J. Schmidt, and K. Bothe, "Validity of Calibrated Photoluminescence Lifetime Measurements of Crystalline Silicon

Wafers for Arbitrary Lifetime and Injection Ranges," *IEEE Journal of Photovoltaics*, vol. 3, pp. 381-386, 2013.

[110] T. Trupke, "Influence of photon reabsorption on quasi-steady-state photoluminescence measurements on crystalline silicon," *Journal of Applied Physics*, vol. 100, p. 063531, 2006.

[111] Y. Augarten, T. Trupke, M. Lenio, J. Bauer, J. W. Weber, M. Juhl, *et al.*, "Calculation of quantitative shunt values using photoluminescence imaging," *Progress in Photovoltaics: Research and Applications*, vol. 21, pp. 933-941, 2013.

[112] C. Donolato, "Modeling the effect of dislocations on the minority carrier diffusion length of a semiconductor," *Journal of Applied Physics*, vol. 84, pp. 2656-2664, 1998.

[113] C. Donolato, "Theory of beam induced current characterization of grain boundaries in polycrystalline solar cells," *Journal of Applied Physics*, vol. 54, pp. 1314-1322, 1983.

[114] S. Riepe, G. Stokkan, T. Kieliba, and W. Warta, "Carrier density imaging as a tool for characterising the electrical activity of defects in pre-processed multicrystalline silicon," *Solid State Phenomena*, vol. 95, pp. 229-234, 2003.

[115] G. Stokkan, S. Riepe, O. Lohne, and W. Warta, "Spatially resolved modeling of the combined effect of dislocations and grain boundaries on minority carrier lifetime in multicrystalline silicon," *Journal of Applied Physics*, vol. 101, p. 053515, 2007.

[116] R. Corkish, T. Puzzer, A. B. Sproul, and K. L. Luke, "Quantitative interpretation of electron-beam-induced current grain boundary contrast profiles with application to silicon," *Journal of Applied Physics*, vol. 84, pp. 5473-5481, 1998.

[117] G. Micard, G. Hahn, A. Zuschlag, S. Seren, and B. Terheiden, "Quantitative evaluation of grain boundary activity in multicrystalline semiconductors by light beam induced current: An advanced model," *Journal of Applied Physics*, vol. 108, p. 034516, 2010.

[118] C. H. Seager, "Grain boundary recombination: Theory and experiment in silicon," *Journal of Applied Physics*, vol. 52, pp. 3960-3968, 1981.

[119] R. Brendel, "Modeling solar cells with the dopant-diffused layers treated as conductive boundaries," *Progress in Photovoltaics: Research and Applications*, vol. 20, pp. 31-43, 2012.

[120] S. C. Baker-Finch and K. R. McIntosh, "A freeware program for precise optical analysis of the front surface of a solar cell," *Proceedings of the 35th IEEE Photovoltaic Specialists Conference*, pp. 2184-2187, 2010.

[121] Synopsys. (2013). *Sentaurus Device User Guide, Version 2013.03*.

[122] M. C. Schubert, S. Pingel, M. The, and W. Warta, "Quantitative carrier lifetime images optically measured on rough silicon wafers," *Journal of Applied Physics*, vol. 101, p. 124907, 2007.

[123] D. G. Luenberger and Y. Ye, *Linear and nonlinear programming*, 3 ed. vol. 116: Springer, 2008.

[124] M. J. Kerr, J. Schmidt, A. Cuevas, and J. H. Bultman, "Surface recombination velocity of phosphorus-diffused silicon solar cell emitters passivated with plasma enhanced chemical vapor deposited silicon nitride and thermal silicon oxide," *Journal of Applied Physics*, vol. 89, pp. 3821-3826, 2001.

[125] A. Cuevas, P. A. Basore, G. Giroult-Matlakowski, and C. Dubois, "Surface recombination velocity of highly doped n-type silicon," *Journal of Applied Physics,* vol. 80, pp. 3370-3375, 1996.
[126] M. Seibt, R. Khalil, V. Kveder, and W. Schröter, "Electronic states at dislocations and metal silicide precipitates in crystalline silicon and their role in solar cell materials," *Applied Physics A,* vol. 96, pp. 235-253, 2009.
[127] F. Liu, C. S. Jiang, H. Guthrey, S. Johnston, M. J. Romero, B. P. Gorman, *et al.*, "Optical response of grain boundaries in upgraded metallurgical-grade silicon for photovoltaics," *Solar Energy Materials and Solar Cells,* vol. 95, pp. 2497-2501, 2011.
[128] A. Cuevas, M. Stocks, S. Armand, M. Stuckings, A. Blakers, and F. Ferrazza, "High minority carrier lifetime in phosphorus-gettered multicrystalline silicon," *Applied Physics Letters,* vol. 70, pp. 1017-1019, 1997.
[129] S. J. Pearton, J. W. Corbett, and T. S. Shi, "Hydrogen in crystalline semiconductors," *Applied Physics A,* vol. 43, pp. 153-195, 1987.
[130] D. Macdonald, A. Cuevas, A. Kinomura, Y. Nakano, and L. J. Geerligs, "Transition-metal profiles in a multicrystalline silicon ingot," *Journal of Applied Physics,* vol. 97, p. 033523, 2005.
[131] J. Tan, A. Cuevas, D. Macdonald, T. Trupke, R. Bardos, and K. Roth, "On the electronic improvement of multi-crystalline silicon via gettering and hydrogenation," *Progress in Photovoltaics: Research and Applications,* vol. 16, pp. 129-134, 2008.
[132] A. Liu, Y.-C. Fan, and D. Macdonald, "Interstitial iron concentrations across multicrystalline silicon wafers via photoluminescence imaging," *Progress in Photovoltaics: Research and Applications,* vol. 19, pp. 649-657, 2011.
[133] P. Manshanden and L. J. Geerligs, "Improved phosphorous gettering of multicrystalline silicon," *Solar Energy Materials and Solar Cells,* vol. 90, pp. 998-1012, 2006.
[134] M. Rinio, A. Yodyunyong, S. Keipert-Colberg, Y. P. B. Mouafi, D. Borchert, and A. Montesdeoca-Santana, "Improvement of multicrystalline silicon solar cells by a low temperature anneal after emitter diffusion," *Progress in Photovoltaics: Research and Applications,* vol. 19, pp. 165-169, 2011.
[135] A. Liu, D. Walter, S. P. Phang, and D. Macdonald, "Investigating internal gettering of iron at grain boundaries in multicrystalline silicon via photoluminescence imaging," *IEEE Journal of Photovoltaics,* vol. 2, pp. 479-484, 2012.
[136] T. Buonassisi, A. A. Istratov, M. D. Pickett, M. Heuer, J. P. Kalejs, G. Hahn, *et al.*, "Chemical natures and distributions of metal impurities in multicrystalline silicon materials," *Progress in Photovoltaics: Research and Applications,* vol. 14, pp. 513-531, 2006.
[137] D. Macdonald, F. Rougieux, Y. Mansoulie, J. Tan, D. Paterson, D. L. Howard, *et al.*, "Scanning X-ray fluorescence microspectroscopy of metallic impurities in solar-grade silicon," *physica status solidi (a),* vol. 207, pp. 1807-1810, 2010.
[138] E. Weber, "Transition metals in silicon," *Applied Physics A,* vol. 30, pp. 1-22, 1983.
[139] T. Buonassisi, M. Heuer, A. A. Istratov, M. D. Pickett, M. A. Marcus, B. Lai, *et al.*, "Transition metal co-precipitation mechanisms in silicon," *Acta Materialia,* vol. 55, pp. 6119-6126, 2007.

[140] P. Plekhanov and T. Tan, "Schottky effect model of electrical activity of metallic precipitates in silicon," *Applied Physics Letters*, vol. 76, pp. 3777-3779, 2000.
[141] B. Ziebarth, M. Mrovec, C. Elsässer, and P. Gumbsch, "Interstitial iron impurities at grain boundaries in silicon: A first-principles study," *Physical Review B*, vol. 91, p. 035309, 2015.
[142] R. Sauer, J. Weber, J. Stolz, E. R. Weber, K. H. Küsters, and H. Alexander, "Dislocation-related photoluminescence in silicon," *Applied Physics A*, vol. 36, pp. 1-13, 1985.
[143] H. T. Nguyen, F. E. Rougieux, F. Wang, H. Tan, and D. Macdonald, "Micrometer-Scale Deep-Level Spectral Photoluminescence From Dislocations in Multicrystalline Silicon," *IEEE Journal of Photovoltaics*, vol. 5, pp. 799-804, 2015.
[144] M. Tajima, Y. Iwata, F. Okayama, H. Toyota, H. Onodera, and T. Sekiguchi, "Deep-level photoluminescence due to dislocations and oxygen precipitates in multicrystalline Si," *Journal of Applied Physics*, vol. 111, p. 113523, 2012.
[145] D. P. Fenning, A. S. Zuschlag, M. I. Bertoni, B. Lai, G. Hahn, and T. Buonassisi, "Improved iron gettering of contaminated multicrystalline silicon by high-temperature phosphorus diffusion," *Journal of Applied Physics*, vol. 113, p. 214504, 2013.
[146] S. Tsurekawa, H. Takahashi, Y. Nishibe, and T. Watanabe, "Potential barrier at grain boundaries in polycrystalline silicon: influence of grain-boundary character and copper/iron contamination," *Philosophical Magazine*, vol. 93, pp. 1413-1424, Apr 2013.
[147] S. Ratanaphan, Y. Yoon, and G. S. Rohrer, "The five parameter grain boundary character distribution of polycrystalline silicon," *Journal of Materials Science*, vol. 49, pp. 4938-4945, 2014.
[148] P. P. Altermatt, A. Cuevas, and G. Heiser, "Modelling the impact of inhomogeneous recombination losses on mc-Si cell efficiency," *Technical Digest of the 14th International Photovoltaic Science and Engineering Conference*, pp. 243-244, 2004.
[149] B. Michl, M. Rüdiger, J. A. Giesecke, M. Hermle, W. Warta, and M. C. Schubert, "Efficiency limiting bulk recombination in multicrystalline silicon solar cells," *Solar Energy Materials and Solar Cells*, vol. 98, pp. 441-447, 2012.
[150] F. Schindler, B. Michl, A. Kleiber, H. Steinkemper, J. Schon, W. Kwapil, *et al.*, "Potential Gain in Multicrystalline Silicon Solar Cell Efficiency by n-Type Doping," *IEEE Journal of Photovoltaics*, vol. 5, pp. 499-506, 2015.
[151] D. A. Clugston and P. A. Basore, "PC1D Version 5: 32-bit Solar Cell Modelling on Personal Computers," *Proceedings of the 26th IEEE Photovoltaic Specialists Conference*, pp. 207-210, 1997.
[152] F. Schindler, B. Michl, P. Krenckel, S. Riepe, F. Feldmann, J. Benick, *et al.*, "Efficiency Potential of p- and n-type High Performance Multicrystalline Silicon," *Energy Procedia*, vol. 77, pp. 633-638, 8// 2015.
[153] F. Schindler, J. Schön, B. Michl, S. Riepe, P. Krenckel, J. Benick, *et al.*, "High Efficiency Multicrystalline Silicon Solar Cells: Potential of n-type Doping," *IEEE Journal of Photovoltaics*, vol. 5, pp. 1571-1579, 2015.
[154] A. Cuevas, M. J. Kerr, C. Samundsett, F. Ferrazza, and G. Coletti, "Millisecond minority carrier lifetimes in n-type multicrystalline silicon," *Applied Physics Letters*, vol. 81, pp. 4952-4954, 2002.

[155] S. Gindner, P. Karzel, B. Herzog, and G. Hahn, "Efficacy of Phosphorus Gettering and Hydrogenation in Multicrystalline Silicon," *IEEE Journal of Photovoltaics,* vol. 4, pp. 1063-1070, 2014.

[156] S. Kleekajai, F. Jiang, M. Stavola, V. Yelundur, K. Nakayashiki, A. Rohatgi, *et al.*, "Concentration and penetration depth of H introduced into crystalline Si by hydrogenation methods used to fabricate solar cells," *Journal of Applied Physics,* vol. 100, p. 093517, 2006.

[157] R. A. Sinton, "Predicting multi-crystalline solar cell efficiency from life-time measured during cell fabrication," *Proceedings of 3rd World Conference on Photovoltaic Energy Conversion,* vol. 2, pp. 1028-1031, 2003.

[158] B. Michl, J. Benick, A. Richter, M. Bivour, J. Yong, R. Steeman, *et al.*, "Excellent Average Diffusion Lengths of 600 μm of N-Type Multicrystalline Silicon Wafers After the Full Solar Cell Process Including Boron Diffusion," *Energy Procedia,* vol. 33, pp. 41-49, 2013.

[159] S. Martinuzzi, I. Périchaud, C. Trassy, and J. Degoulange, "n-Type multicrystalline silicon wafers prepared from plasma torch refined upgraded metallurgical feedstock," *Progress in Photovoltaics: Research and Applications,* vol. 17, pp. 297-305, 2009.

[160] C. Sun, F. E. Rougieux, and D. Macdonald, "A unified approach to modelling the charge state of monatomic hydrogen and other defects in crystalline silicon," *Journal of Applied Physics,* vol. 117, p. 045702, 2015.

[161] D. Macdonald and A. Cuevas, "Reduced fill factors in multicrystalline silicon solar cells due to injection-level dependent bulk recombination lifetimes," *Progress in Photovoltaics: Research and Applications,* vol. 8, pp. 363-375, 2000.

[162] O. Breitenstein, J. Bauer, D. Hinken, and K. Bothe, "The reliability of thermography- and luminescence-based series resistance and saturation current density imaging," *Solar Energy Materials and Solar Cells,* vol. 137, pp. 50-60, 2015.

[163] B. Hoex, J. Schmidt, P. Pohl, M. C. M. v. d. Sanden, and W. M. M. Kessels, "Silicon surface passivation by atomic layer deposited $Al_2O_3$," *Journal of Applied Physics,* vol. 104, p. 044903, 2008.

[164] M. J. Kerr and A. Cuevas, "Recombination at the interface between silicon and stoichiometric plasma silicon nitride," *Semiconductor science and technology,* vol. 17, p. 166, 2002.

[165] M. J. Kerr and A. Cuevas, "Very low bulk and surface recombination in oxidized silicon wafers," *Semiconductor science and technology,* vol. 17, p. 35, 2001.

[166] Y. Wan, K. R. McIntosh, and A. F. Thomson, "Characterisation and optimisation of PECVD $SiN_x$ as an antireflection coating and passivation layer for silicon solar cells," *AIP Advances,* vol. 3, p. 032113, 2013.

[167] K. R. McIntosh and L. P. Johnson, "Recombination at textured silicon surfaces passivated with silicon dioxide," *Journal of Applied Physics,* vol. 105, p. 124520, 2009.

[168] W. Liang, K. J. Weber, S. Dongchul, S. P. Phang, Y. Jun, A. K. McAuley, *et al.*, "Surface Passivation of Boron-Diffused p-Type Silicon Surfaces With (1 0 0) and (1 1 1) Orientations by ALD $Al_2O_3$ Layers," *IEEE Journal of Photovoltaics,* vol. 3, pp. 678-683, 2013.

[169] L. E. Black, T. C. Kho, K. R. McIntosh, and A. Cuevas, "The Influence of Orientation and Morphology on the Passivation of Crystalline Silicon Surfaces by Al2O3," *Energy Procedia,* vol. 55, pp. 750-756, 2014.
[170] W. Yimao and K. R. McIntosh, "On the Surface Passivation of Textured C-Si by PECVD Silicon Nitride," *Ieee Journal of Photovoltaics,* vol. 3, pp. 1229-1235, 2013.
[171] D. H. Macdonald, A. Cuevas, M. J. Kerr, C. Samundsett, D. Ruby, S. Winderbaum, *et al.,* "Texturing industrial multicrystalline silicon solar cells," *Solar Energy,* vol. 76, pp. 277-283, 2004.
[172] B. Sopori, D. Guhabiswas, P. Rupnowski, S. Shet, S. Devayajanam, and H. Moutinho, "A new method for rapid measurement of orientations and sizes of grains in multicrystalline silicon wafers," *Proceedings of the 37th IEEE Photovoltaic Specialists Conference* pp. 1680-1685, 2011.
[173] C. Reimann, E. Meissner, M. Trempa, T. Lehmann, and J. Friedrich, "A New Characterization Tool for the Investigation of the Crystal Structure of Multi Crystalline Silicon," *Proceedings of the 27th European Photovoltaic Solar Energy Conference,* 2012.
[174] Y. Wang, J. Murphy, and P. Wilshaw, "Determination of Grain Orientations in Multicrystalline Silicon by Reflectometry," *Journal of the Electrochemical Society,* vol. 157, pp. H884-H890, 2010.
[175] D. Lausch, M. Gläser, and C. Hagendorf, "Determination of crystal grain orientations by optical microscopy at textured surfaces," *Journal of Applied Physics,* vol. 114, p. 194509, 2013.
[176] R. K. Ahrenkiel, S. W. Johnston, W. K. Metzger, and P. Dippo, "Relationship of band-edge luminescence to recombination lifetime in silicon wafers," *Journal of Electronic Materials,* vol. 37, pp. 396-402, 2008.
[177] M. Turek, "Interplay of bulk and surface properties for steady-state measurements of minority carrier lifetimes," *Journal of Applied Physics,* vol. 111, p. 123703, 2012.
[178] T. Mchedlidze, W. Seifert, M. Kittler, A. T. Blumenau, B. Birkmann, T. Mono, *et al.,* "Capability of photoluminescence for characterization of multi-crystalline silicon," *Journal of Applied Physics,* vol. 111, p. 073504, 2012.
[179] P. V. Gray and D. M. Brown, "Density of SiO2single bond signSi interface states," *Applied Physics Letters,* vol. 8, pp. 31-33, 1966.
[180] G. H. Lu, M. Huang, M. Cuma, and F. Liu, "Relative stability of Si surfaces: A first-principles study," *Surface Science,* vol. 588, pp. 61-70, 2005.
[181] W. Liu, W. T. Zheng, and Q. Jiang, "First-principles study of the surface energy and work function of III-V semiconductor compounds," *Physical Review B,* vol. 75, p. 235322, 2007.
[182] J. D. Gale and A. L. Rohl, "The General Utility Lattice Program (GULP)," *Molecular Simulation,* vol. 29, pp. 291-341, 2003.
[183] R. J. Jaccodine, "Surface Energy of Germanium and Silicon," *Journal of the Electrochemical Society,* vol. 110, pp. 524-527, 1963.
[184] A. A. Stekolnikov, J. Furthmüller, and F. Bechstedt, "Absolute surface energies of group-IV semiconductors: Dependence on orientation and reconstruction," *Physical Review B,* vol. 65, p. 115318, 2002.
[185] A. A. Stekolnikov, J. Furthmüller, and F. Bechstedt, "Adatoms, dimers, and interstitials on group-IV(113) surfaces: First-principles studies of energetical,

structural, and electronic properties," *Physical Review B,* vol. 67, p. 195332, 2003.

[186] X. Gu, X. Yu, K. Guo, L. Chen, D. Wang, and D. Yang, "Seed-assisted cast quasi-single crystalline silicon for photovoltaic application: Towards high efficiency and low cost silicon solar cells," *Solar Energy Materials and Solar Cells,* vol. 101, pp. 95-101, 2012.

[187] E. A. Irene, H. Z. Massoud, and E. Tierney, "Silicon Oxidation Studies: Silicon Orientation Effects on Thermal Oxidation," *Journal of the Electrochemical Society,* vol. 133, pp. 1253-1256, 1986.

[188] E. Arnold, J. Ladell, and G. Abowitz, "Crystallographic symmetry of surface state density in thermally oxidized silicon," *Applied Physics Letters,* vol. 13, pp. 413-416, 1968.

[189] R. A. Sinton and A. Cuevas, "Contactless determination of current--voltage characteristics and minority-carrier lifetimes in semiconductors from quasi-steady-state photoconductance data," *Applied Physics Letters,* vol. 69, pp. 2510-2512, 1996.

[190] A. G. Aberle, S. Glunz, and W. Warta, "Impact of illumination level and oxide parameters on Shockley–Read–Hall recombination at the Si-SiO2 interface," *Journal of Applied Physics,* vol. 71, pp. 4422-4431, 1992.

[191] S. W. Glunz, A. B. Sproul, W. Warta, and W. Wettling, "Injection-level-dependent recombination velocities at the Si-SiO2 interface for various dopant concentrations," *Journal of Applied Physics,* vol. 75, pp. 1611-1615, 1994.

[192] A. A. Istratov, T. Buonassisi, R. J. McDonald, A. R. Smith, R. Schindler, J. A. Rand, *et al.*, "Metal content of multicrystalline silicon for solar cells and its impact on minority carrier diffusion length," *Journal of Applied Physics,* vol. 94, pp. 6552-6559, 2003.

[193] R. S. Houk, V. A. Fassel, G. D. Flesch, H. J. Svec, A. L. Gray, and C. E. Taylor, "Inductively coupled argon plasma as an ion source for mass spectrometric determination of trace elements," *Analytical Chemistry,* vol. 52, pp. 2283-2289, 1980.

[194] J. Chen, B. Chen, W. Lee, M. Fukuzawa, M. Yamada, and T. Sekiguchi, "Grain Boundaries in Multicrystalline Si," *Solid State Phenomena,* vol. 156-158, pp. 19-26, 2010.

[195] T. Tachibana, J. Masuda, A. Ogura, Y. Ohshita, and K. Arafune, "Structural Change by Annealing Process at Sigma 9 Grain Boundaries in Multicrystalline Silicon Substrate for Solar Cells," *Electrochemical and Solid State Letters,* vol. 13, pp. B79-B82, 2010.

[196] W. Seifert, O. F. Vyvenko, T. Arguirov, A. Erko, M. Kittler, C. Rudolf, *et al.*, "Synchrotron microscopy and spectroscopy for analysis of crystal defects in silicon," *physica status solidi (c),* vol. 6, pp. 765-771, 2009.

[197] K. Takuto, T. Tomihisa, K. Nobuaki, O. Yoshio, A. Koji, O. Atsushi, *et al.*, "Nickel distribution and recombination activity in as-grown and annealed multicrystalline silicon," *Japanese Journal of Applied Physics,* vol. 53, p. 04ER20, 2014.

[198] D. B. Needleman, H. Wagner, P. P. Altermatt, and T. Buonassisi, "Assessing the Device-performance Impacts of Structural Defects with TCAD Modeling," *Energy Procedia,* vol. 77, pp. 8-14, 2015.

[199] D. P. Fenning, A. S. Zuschlag, J. Hofstetter, A. Frey, M. I. Bertoni, G. Hahn, *et al.*, "Investigation of Lifetime-Limiting Defects After High-Temperature Phosphorus Diffusion in High-Iron-Content Multicrystalline Silicon," *IEEE Journal of Photovoltaics,* vol. 4, pp. 866-873, 2014.

[200] B. J. Hallam, P. G. Hamer, S. Wang, L. Song, N. Nampalli, M. D. Abbott, *et al.*, "Advanced Hydrogenation of Dislocation Clusters and Boron-oxygen Defects in Silicon Solar Cells," *Energy Procedia,* vol. 77, pp. 799-809, 2015.